PORTABLE ELECTROCHEMICAL AND PLASMONIC BIOSENSORS FOR BIOMEDICAL APPLICATION

BY

XINHAO WANG

DISSERTATION

Submitted in partial fulfillment of the requirements
for the degree of Doctor of Philosophy in Electrical and Computer Engineering
in the Graduate College of the
University of Illinois at Urbana-Champaign, 2016

Urbana, Illinois

Doctoral Committee:

Associate Professor Gang Logan Liu, Chair
Professor Brian T. Cunningham
Associate Professor Gabriel Popescu
Professor Xiuling Li

ABSTRACT

Portable sensing for point-of-care (POC) has attracted a lot of attention in these years and has been developed in a wide variety for clinical and environmental applications. The idea of POC comes from the advances in portable smart electronic devices and micro-fluid systems which can be integrated and miniaturized into a lab-on-a-chip. Modern electronic devices, like smartphones, smartwatchs or even headsets, can achieve signal generating and receiving by using interfaces like camera, flashlight, audio-jack, micro-USB and wireless module. On the other side, development in the micro-fluid system enables the integration of different diagnosis techniques like separation, quenching, lysing and sensing into a single chip. Polydimethylsiloxane (PDMS) and SU-8 photoresist were commonly used in building such micro-fluid systems, which was first demonstrated by Whiteside's group. Quite a large number of applications were published by coupling such system with optical or electrical sensing techniques. In recent years, paper-based micro-fluid systems have begun to take over the traditional micro-fluid systems mainly due to paper's pump-free and cost-effective property. Some new fabrication methods like wax printing, screen printing and 3D printing were utilized to make such paper-based platforms more attractive. The paper substrate has been verified for use in different sensing stages with all of its properties, such as porous, self-pumping, flexible, anti-oxidation, cost-effective and hydrophilic capabilities.

Many sensing techniques have been demonstrated to be coupled with such micro-fluid systems mentioned above for POC applications. Plasmonic and electrochemical methods are the two techniques that will be illustrated in this dissertation. The plasmonic method is new in the sensing area. Plasmon is the oscillation of free electrons at the interface of metal and dielectric material. With the incident of light, the resonance mode will be excited at some certain frequencies which can enhance the optical signal in the form

of reflection or transmission peaks. The resonance frequency can be tuned by adjusting the surface refractive index, in such a way to achieve sensing. More sensitive quantification could be achieved on some molecules with a specific absorbance preference if the absorbance peak matches the resonance mode of the sensing substrate. This is the specific application for sensing some bio-targets with plasmon-induced absorbance enhancement. On the contrary, the electrochemical method is a classic method to analyze the electrical and chemical signal at the solid-liquid interface. Since it is easy to miniaturize and integrate into modern electronic devices, it is widely used in micro-fluid systems and POC applications. Most of the electrochemical sensing techniques like potentiommetry, amperometry and impedance methods create a balance of electrode kinetics and diffusion. The change of current or impedance can be sensed by applying different forms of potential at the electrode surface. Such electrical signal change indicates the variations in concentration, which can be used to quantify the ions or bio-targets.

With such micro-fluid systems and sensing techniques mentioned above, many environmental or clinical applications can be transformed into point-of-care applications. For ion concentration quantification, electrochemical and colorimetric methods could be the best solution. In the area of biosensing, small molecules like glucose and larger targets like protein are what mostly interest people, since they are very useful indicators of personal health conditions. Plasmonic sensing could be used here due to refractive index change or by matching the absorbance peak with the plasmonic resonance mode. Electrochemical method could also be applied if a redox system could be built. For larger bio-target sensing, like cells and bacteria, plasmonic enhanced fluorescence or plasmonic enhancement by labeling with gold nano-particles could help with the optical colorimetric sensing. The electrochemical method is also applicable when used with optimized voltammetry method. By combining these sensing techniques and micro-fluid systems for target separation, quantification and identification, the future of POC technology is promising.

To my wife and parents, for their love and support.

"Hope is a good thing,

...

maybe the best of things."

ACKNOWLEDGMENTS

I would like to express my sincere gratitude to my doctoral dissertation advisor Prof. Gang Logan Liu. His broad knowledge, insightful guidance and continuous support encouraged me during my doctoral program. I would never have achieved this without his mentoring.

I am truly grateful to have Prof. Brian Cunningham, Prof. Xiuling Li and Prof. Gabriel Popescu who served on my defense committee. Their comments and suggestions for the dissertation are precise and critical, which makes it more rigorous and complete.

My colleagues in the Liu Nanobionics group provided me with endless help in problem discussion, experiment design and execution. I would like to thank Manas Ranjan Gartia, Te-Wei Chang, Austin Hsiao, Sujin Seo, Zhida Xu, Jing Jiang, Lisa Plucinski, Abid Ameen, Chester Hu, Xiangfei Zhou and Yukun Ren for being part of the group. My thanks are also due to current and past members of the Liu Nanobionics group for creating a very friendly work environment. In addition, I would like to acknowledge the staff of the Micro and Nanotechnology Laboratory, Materials Research Laboratory at the University of Illinois at Urbana-Champaign for their help in the experiment.

I would like to thank my parents for their continuing support throughout my academic endeavors. My final gratitude goes to my wife Lingling Meng, for our wonderful unexpected meeting on campus and her endless support on my way to earning this academic degree.

TABLE OF CONTENTS

CHAPTER 1

INTRODUCTION

1.1 Portable biosensors: Background to application

The use of transportable, portable, and handheld instruments (e.g.,blood glucose meter) with test kits or strips made a revolution in clinical and environmental testing in the past ten years. Smartphones with excellent data processing and communication functions will push the revolution further by connecting to new developed portable and highly sensitive micro- or nanosensors.

The revolution to clinical application is point-of-care (POC) testing. POC testing is defined as medical testing at or near the site of patient care. Simple tests include those found in medical examinations, urine test strips and even simple imaging such as with a portable ultrasound device.

The driving notion behind POC testing is to bring the test conveniently and immediately to the patient. This increases the likelihood that the patient, physician, and care team will receive the results quicker, which allows for making immediate clinical management decisions. Cheaper, faster, and smarter POC testing devices have increased their use and made them cost-effective for many diseases.

The revolution to environmental application is the portable instrument for measurement of contaminants in water or soil. Reductants of contaminant ions like nitrate, nitrite, phosphate and ammonia are able to be detected by electrochemical method which could be easily applied to portable instruments. Organic pollutants like industrial solvents and chlorinated solvents which have a large refractive index change could be detected by portable colorimetric sensing techniques which are based on the localized surface plasmon resonance principle.

The study of biosensors discussed in this dissertation is based on the sens-

ing principle at the liquid-solid interface. As for electrical biosensors, the electrochemical method is the core to convert bio-signals into electrical signals. While for optical biosensors, the plasmonic phenomenon is the primary sensing principle for spectral, imaging or colorimetric sensing applications. The following two sections will discuss in detail these two sensing principles primarily used in biosensors.

1.2 Principle of electrochemical biosensor

Electrochemistry is an area that studies the phenomenon at the electrode interface, where electrode kinetics and diffusion are generally involved, such that most sensing principles are based on the balance of these two mechanisms. Figure 1.1a demonstrates the diffusion and electron transfer process at the electrode surface.

The most commonly used sensing technique in electrochemistry is the voltammetry method, which retrieves the current signal by changing the potential at the electrode interface. Next the cyclic voltammetry is presented as an example to show the balance between electrode kinetics and diffusion. Figure 1.1b shows a typical I-V curve from the cyclic voltammetry (CV) method.

Cyclic voltammetry is a type of potentiodynamic electrochemical measurement. In a cyclic voltammetry experiment, the working electrode potential is ramped linearly versus time. Unlike inlinear sweep voltammetry, after the set potential is reached in a CV experiment, the working electrode's potential is ramped in the opposite direction to return to the initial potential. These cycles of ramps in potential may be repeated as many times as desired. The current at the working electrode is plotted versus the applied voltage (i.e., the working electrode's potential) to give the cyclic voltammogram trace. Cyclic voltammetry is generally used to study the electrochemical properties of ananalyte in solution [1–3].

For an electrochemical system with only oxide in the solution, the governing equation for a single side linear voltage sweeping is [1]:

$$E = E^{0'} + \frac{RT}{nF} \ln \frac{C_O(0,t)}{C_R(0,t)} \tag{1.1}$$

$$E(t) = E_i - vt \tag{1.2}$$

$$-J_O(0,t) = \frac{i(t)}{nFA} = D_O \left[\frac{\partial C_O(x,t)}{\partial x}\right] \tag{1.3}$$

$$\frac{\partial C_O(x,t)}{\partial t} = D_O \frac{\partial^2 C_O(x,t)}{\partial x^2} \tag{1.4}$$

$$\frac{\partial C_R(x,t)}{\partial t} = D_R \frac{\partial^2 C_R(x,t)}{\partial x^2} \tag{1.5}$$

At the interface of the metal electrode and solution, the boundary equations are [1]:

$$C_O(x,0) = C_O^* \tag{1.6}$$

$$\lim_{x\to\infty} C_O(x,t) = C_O^* \tag{1.7}$$

$$C_R(x,0) = 0 \tag{1.8}$$

$$\lim_{x\to\infty} C_R(x,t) = C_R^* \tag{1.9}$$

$$D_O(\frac{\partial C_O(x,t)}{\partial x})_{x=0} + D_R(\frac{\partial C_R(x,t)}{\partial x})_{x=0} = 0 \tag{1.10}$$

By solving the above equations and boundary conditions, the peak current intensity could be written as [1]:

$$i_p = (2.69 \times 10^5) n^{3/2} A D_O^{1/2} C_O^{1/2} v^{1/2} \tag{1.11}$$

The current density is linearly proportional to the concentration of analyte at the fixed voltage sweeping rate. Despite the ramp function for electrode potential, other functions could also be applied to the electrode interface to retrieve the corresponding current signal, like step function or more compli-

cated functions for differential pulse voltammetry (DPV) and square wave voltammetry (SWV).

Unlike the voltammetry method which collects the current signal, electrochemical impedance spectroscopy (EIS) instead analyzes charge transfer resistance and diffusion impedance, which is another useful tool for electrochemical sensing. With electrode potential set at 0 volt, the EIS system can be converted into an impedance spectroscopy (IS) system, which is a relative powerful method of characterizing many of the electrical properties of materials and their interfaces with electronically conducting electrodes. It could be used to investigate the dynamics of bound or mobile charge in the bulk or interfacial regions of any kind of solid or liquid material: ionic, semiconducting, mixed electronic-ionic, and even insulators (dielectrics) [4].

Any intrinsic property that influences the conductivity of an electrode-materials system, or an external stimulus, can be studied by IS. The parameters derived from an IS spectrum fall generally into two categories: (a) those pertinent only to the material itself, such as conductivity, dielectric constant and mobility of recombination rates; and (b) those pertinent to an electrode-material interface, such as adsorption-reaction rate constants, capacitance of the interface region, and diffusion coefficient of neutral species in the electrode itself [4].

The classic model for impedance spectroscopy is mixed controlled by kinetic and diffusion. At the interface of the electrode and electrolyte, the equivalent circuit could be considered as shown in Fig. 1.2a.

The parallel elements are introduced because the total current through the electrode interface is the sum of distinct contributions from the faradaic process and double-layer charging. The double-layer capacitance at the electrode interface is nearly a pure capacitance; hence it is represented in the equivalent circuit by the element C_d. The faradaic process cannot be represented by a simple linear circuit element. One way to represent this is to separate a pure resistance, R_{ct}, the charge transfer resistance, from another general impedance, Z_W, the Warburg impedance, which represents a kind of resistance to mass transfer. R_π represents the resistance of solution. By taking into consideration of the frequency, which affects the value of Z_W and

C_d, the total impedance for the real and image parts could be derived as [1]:

$$Z_{Re} = R_\pi + \frac{R_{ct} + \sigma\omega^{-1/2}}{(C_d\sigma\omega^{1/2}+1)^2 + \omega^2 C_d^2 (R_{ct} + \sigma\omega^{-1/2})^2} \tag{1.12}$$

$$Z_{Im} = \frac{\omega C_d (R_{ct} + \sigma\omega^{-1/2})^2 + \sigma\omega^{-1/2}(\omega^{1/2} C_d\sigma + 1)}{(C_d\sigma\omega^{1/2}+1)^2 + \omega^2 C_d^2 (R_{ct} + \sigma\omega^{-1/2})^2} \tag{1.13}$$

$$\sigma = \frac{RT}{n^2F^2A\sqrt{2}} \left(\frac{1}{D_O^{1/2} C_O^*} + \frac{1}{D_R^{1/2} C_R^*} \right) \tag{1.14}$$

n is the number of transfer electron; F is Faraday constant; A is the electrode surface area; R is gas constant; T is temperature; D is diffusion constant; C^* is the bulk concentration.

For low-frequency limit approximation, the relationship between the real part and imaginary part of impedance could be written as:

$$Z_{Im} = Z_{Re} - R_\pi - R_{ct} + 2\sigma^2 C_d \tag{1.15}$$

For high-frequency limit approximation, the relationship between the real part and imaginary part of impedance could be written as:

$$\left(Z_{Re} - R_\pi - \frac{R_{ct}}{2} \right)^2 + Z_{Im}^2 = \left(\frac{R_{ct}}{2} \right)^2 \tag{1.16}$$

By sweeping from low frequency to high frequency, the real part and imaginary part of impedance could be drawn on the same plot, which is called the Nyquist plot shown in Fig. 1.2b. From the Nyquist plot, the charge transfer resistance (R_{ct}), double-layer capacitance (C_d) and peak frequency of the Nyquist circle could all be derived. The conductivity and permittivity which are related to electrolyte concentration at the electrode interface could be characterized from these parameters.

As discussed above, electrochemistry is the study at the electrode interface. Parameter changes at such interfaces could be used for bio-sensing. For ion concentration quantification, the diffusion flux which is due to the concentration gradient could be used to obtain the current signal for sensing. For many bio-target quantification applications, the electrode coverage due

to surface binding is another merit for sensing. Among these applications, both the charge transfer process and the diffusion process can be applied to build an optimized sensing system.

1.3 Principle of plasmonic biosensor

Electrochemistry is the study of electrical signal at the sensing interface, while plasmonics is the study of optical signal at such an interface, normally between liquid and solid.

Surface plasmon is collective oscillations of the free electrons at the interface of two materials. Noble metals like gold (Au) and silver (Ag) have been reported to exhibit strong surface plasmon polariton (SPP) in the visible wavelength at the condition of momentum matching [5]. This condition can be expressed as:

$$\boldsymbol{k}_0 \sin\theta = \boldsymbol{k}_{spp} \tag{1.17}$$

where $\boldsymbol{k}_0$ is the wavevector of incident light, θ is the incident angle and $\boldsymbol{k}_{spp}$ is the wavevector of SPP mode [6], [7]. $\boldsymbol{k}_{spp}$ can be expressed as:

$$\boldsymbol{k}_{spp} = \boldsymbol{k}_0 \sqrt{\frac{\varepsilon_m \varepsilon_d}{\varepsilon_m + \varepsilon_d}} \tag{1.18}$$

where ε_m and ε_d are the dielectric constants of the surface metal and surrounding materials [6–9]. Although prism coupling could satisfy this condition by increasing the dielectric constant which increases the incident in-plane wavevector, this massive configuration is out of date for convenient bio-sensing application. Nano-array structures could achieve this momentum matching condition in the form of sub-wavelength grating without a bulky optical component. The matching condition can be described by Braggs coupling equation:

$$\boldsymbol{k}_0 \sin\theta \pm \upsilon \boldsymbol{G} = \boldsymbol{k}_{spp} \tag{1.19}$$

where υ is the grating order for the reciprocal grating vector $\boldsymbol{G}$ ($\boldsymbol{G} = \frac{2\pi}{a}$, a is the grating period) [7–9]. The resonance condition for SPP can be tuned by changing the incident angle (θ), period of nano-array structure (a) or

dielectric constant of material (ε_d) over the metal surface. The minimum condition of $\varepsilon_m(\omega) + \varepsilon_d(\omega)$ is the foundation for refractive index sensing [7].

Nano-array structures with specifically designed size and shape can even exhibit localized surface plasmon (LSP) which is normally confined to metal particles or curved surface [6], [7], [10]. The resonance condition for LSP is quite different from the condition for SPP due to the different boundary conditions in modeling. If an ideal sphere metal nano-particle with sub-wavelength size is analyzed, the scattering field will reach its maximum at the minimum condition of $\varepsilon_m(\omega) + 2\varepsilon_d(\omega)$ [7]. This resonance mode derived from a noble metal particle can also be estimated from Mie scattering. Due to the confines of LSP resonance (LSPR) by nature, the short decay length is an intrinsic property that enhanced scattering field is only effective within a short distance ($\sim$10 nm) from the metal surface. This property leads to ultra-sensitivity of LSPR-based nano-arrays for bio-sensing whenever the analyte in question is very close to the metal particle surface [11]. Figure 1.3 illustrates the electric field distribution from both SPP and LSPR. The decay length of these two modes were also demonstrated.

The LSPR mode is the key feature that both the highly sensitivity to refractive index change and enhanced scattering field within its decay length can be utilized for ultra-sensitive bio-sensing. As for sensing by refractive index change, the sensing performance is usually evaluated by the figure of merit (FOM), which is related to sensitivity (S) and the full-width at half maximum (FWHM) at the resonant peak [12]. The sensitivity is measured by wavelength shift per refractive index unit (RIU), which is often defined by the structures intrinsic parameters like depth and metal coverage. The FWHM indicates the ability of the structure to confine EM fields at resonance mode, which determines selectivity.

$$\text{FOM} = \frac{\text{S (nm/RIU)}}{\text{FWHM (nm)}} \tag{1.20}$$

It is important to have high RI sensitivity and resolution for effective ion or bio-target quantification. In terms of common ion quantification, a SPR-based sensor with high sensitivity often displays its advantage with a stronger signal than LSPR, since the change of target concentration is uniform within the decay length of wave propagation. But for the case of certain metal ions or bio-targets which accumulate or bind closely at the nano-array surface,

LSPR sensors show an ultra-sensitive response to low concentration change.

Despite the refractive index sensing, the locally enhanced electro-magnetic field near the plasmonic structure surface can be used for fluorescence and absorbance enhancement. Due to the curved nano-structure, a locally enhanced field behaves like an energy hot-spot, which confines energy at high intensity. The fluorophore or chromophore which absorbs light acts as an acceptor while the plasmon acts as an energy donor, similar to Foster resonant energy transfer (FRET). By matching the fluorophore or chromophores absorbance peak and the devices plasmonic resonance peak, the absorbance of fluorophore or chromophore could be enhanced. The performance is normally evaluated by an enhancement factor, a comparison with a plane metal surface.

The portable plasmonic biosensor discussed in this dissertation was used for both refractive index sensing and absorbance enhancement sensing.

1.4 Overview of dissertation

In this dissertation, the development of portable electrochemical and plasmonic biosensor is discussed in detail, as well as the sensor integration in the system level. Chapter 2 summarizes current state-of-the-art approaches to portable biosensors, especially smartphone and microfluidic based, for biomedical application. Chapter 3 mainly includes the characterization of a novel plasmonic biosensor with a nano-cup array structure. Portable solutions for both refractive index sensing and absorbance enhancement sensing were demonstrated. Chapter 4 demonstrates a miniaturized electrochemical sensor integrated to the smartphone-based sensing system, which makes use of frequency modulation through an audio jack. Chapter 5 illustrates a preconcentrate interdigitated electrode for bacteria sensing using an impedance spectroscopy method. The sensing system is based on wireless communication. Chapter 6 shows a novel paper-based interdigitated electrode, which can effectively do white blood cell quantification using physical adsorption and a diffusion blockage mechanism. In addition, different parameters for such paper-based electrochemical sensor is characterized. In Chapter 7, a further study on paper-based electrochemical sensors is performed and the filtering function of such electrodes for both separation and sensing is devel-

oped.

1.5 Figures

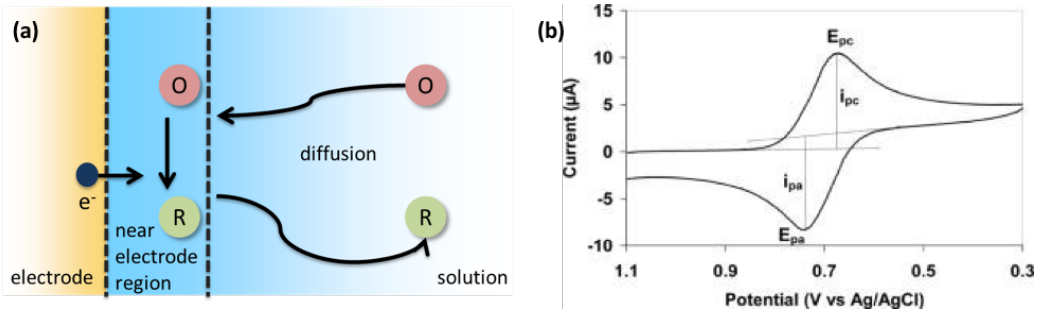

Figure 1.1: Electrochemical principle and method. (a) Diffusion and electron transfer near the electrode surface. (b) Cyclic voltammetry curve with current at y axis and potential at x axis.

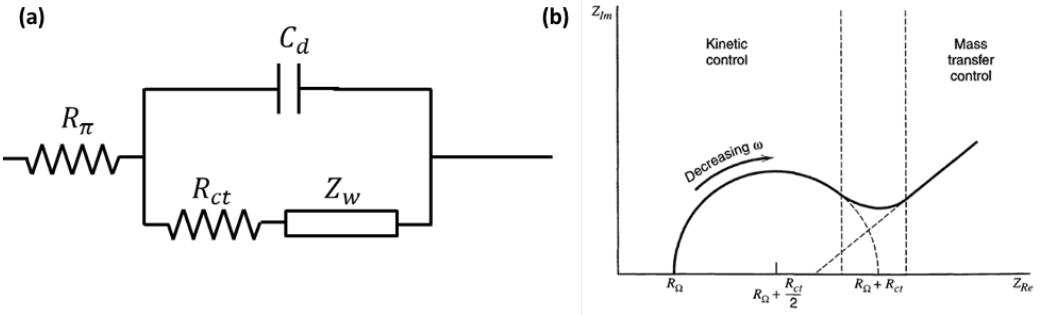

Figure 1.2: Principle of electrochemical impedance spectroscopy. (a) Equivalent circuit at the electrode and solution interface. (b) Nyquist plot with both mass transfer control and kinetic control.

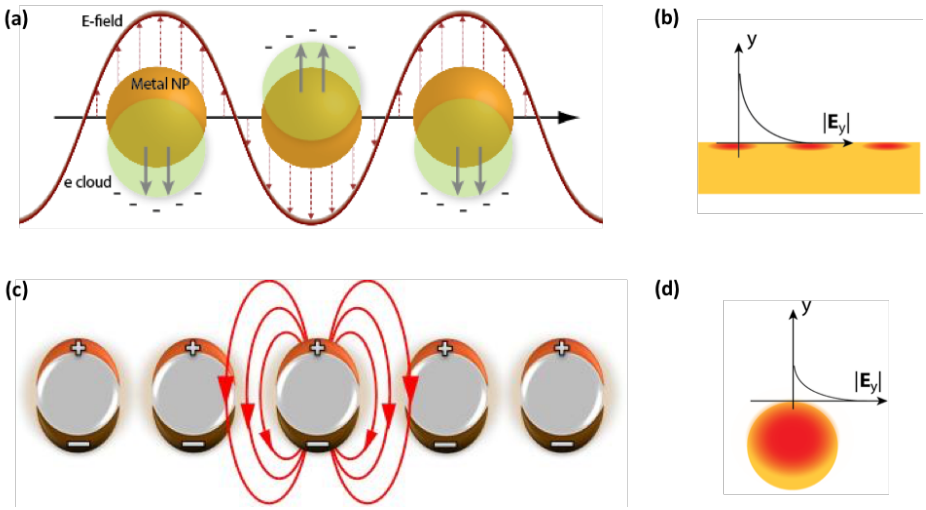

Figure 1.3: Comparison between SPR and LSPR. (a) Illustration of SPR. (b) Decay length for SPR. (c) Illustration of LSPR. (d) Decay length for LSPR.

CHAPTER 2

BACKGROUND AND MOTIVATION

In this chapter, a review on current portable devices for biomedical sensing will be introduced. Both optical and electrical solutions for such portable sensing will be shown. A paper-based microfluidic technique which has been very popular in recent years will also be introduced. The advantages and challenges of each technique will be discussed as well. In the last section of this chapter, considerations in system design will be discussed.

2.1 Introduction

There have been many portable bio-sensing devices which are mainly applied to clinical diagnosis and environmental monitoring. The targets for bio-sensing can be ions, small molecules, proteins, DNA or large cells. The physical and chemical properties vary a lot among these targets. Most of the sensing techniques can be classified into two categories in terms of principle: optical and electrical. The optical sensors usually make use of fluorescence, plasmonic, colorimetric or chemiluminescence to generate optical signals which will be used for quantification. The electrical sensors, mostly electrochemical or impedance sensors, characterize electrical signals like voltage, current or impedance to quantify the sensing target. The following two sections will specifically focus on optical and electrical solutions for portable sensing.

2.2 Portable biosensing with optical solution

The use of portable optical bio-sensing usually involves an optimized light source, sensitive sensing technique and advanced image processing method. In the world of labeling sensing, fluorescence is still a reliable technique where

strong and stable optical signals can be obtained through a portable instrument like a smartphone. So a fluorescence microscopy imaging system is first integrated into a portable instrument.

Oscan's group at UCLA led the use of an embedded camera in a smartphone for different kinds of medical, biological and environmental applications (see Fig. 2.1). They developed a smartphone-based handheld platform that allows the quantification of mercury ions in water samples with a parts per billion (ppb) level of sensitivity. A plasmonic gold nanoparticle and aptamer-based colorimetric transmission assay was first implemented in disposable test tubes. They quantified mercury ion concentration in water samples by using a two-color ratiometric method employing light-emitting diodes (LEDs) at 523 nm and 625 nm, where a custom-developed application was utilized to process each acquired transmission image on the same phone to achieve a limit of detection of $\sim$3.5 ppb [13]. In the food industry, a cellphone based imaging platform for a microsphere fluorescence immunoassay that detects the presence of anti-recombinant bovine somatotropin (rbST) antibodies in milk extracts was developed [14]. In the field of biology, Q. Wei *et al.* [15] demonstrated imaging and length quantification of single-molecule DNA strands using a compact, lightweight and cost-effective fluorescence microscope installed on a mobile phone. As another environmental application, Koydemir *et al.* [16] demonstrated a field-portable and cost-effective platform for detection and quantification of Giardia lamblia cysts, one of the most common waterborne parasites, which has a thick cell wall that makes it resistant to most water disinfection techniques including chlorination. The platform consists of a smartphone coupled with an opto-mechanical attachment, which utilizes a handheld fluorescence microscope design aligned with the camera unit of the smartphone to image custom designed disposable water sample cassettes.

In the world of label-free bio-sensing, it requires either high sensitivity in the visible wavelength from the device or an embedded miniaturized spectrometer system. Cunningham's group at UIUC utilized photonic crystal as the sensing substrate, which showed very high-quality factor. The embedded camera on smartphone was used as a spectrometer to read out signals from the ELISA assay [17].

Instead of a physical process, some chemical process or reaction could also be utilized for optical sensing. The most common method is the colorimetric

sensing by chemical reactions. Shen *et al.* used an advanced image processing algorithm to achieve colorimetric sensing on strips by analyzing images taken from a smartphone [18].

2.3 Portable biosensing with electrical solution

Most of the portable electrical bio-sensing is based on an electrochemical principle, which converts a signal from a bio-target into an electrical signal in terms of voltage, current or impedance. The most successful case is the handheld glucose meter. Three-electrode miniaturization is the key in portable electrochemical sensing.

Lillehoj *et al.* [19] presented a microfluidic based amperometric sensor for fast quantification of PfHRP2, which is an important indicator for malaria (see Fig. 2.2a). By monitoring the electrochemical current when constant potential is applied, the biomarker quantification could be implemented. The communication between phone and sensing board was achieved by micro-USB, which is a universal interface on phones.

Whiteside's group developed an inexpensive, handheld device that couples the most common forms of electrochemical analysis, like cyclic voltammetry, anode striping, and differential pulse voltammetry, for use in resource-limited settings (see Figs. 2.2b and 2.2c). The device is designed to operate with a wide range of electrode formats, performs on-board mixing of samples by vibration, and transmits data over voice using audio, an approach that guarantees broad compatibility with any available mobile phone [20].

Besides the electrochemical method for sensing, the impedance method was also applied for bio-sensing in recent years. Zhang *et al.* proposed an impedance sensor system which made use of screen printed electrodes for 2,4,6-trinitrotoluene (TNT) detection. The electrochemical impedance spectroscopy method was first applied to verify the peptide binding on the electrode. Bluetooth was used for portable sensing through the smartphone, in which the sensing data could be sent to a smartphone wirelessly. In order to simplify the sensing hardware requirement, single frequency impedance was used and the critical frequency was optimized by analyzing the EIS response [21].

2.4 Portable biosensing with paper-based microfluidic technique

Although a microfluidic technique enabled portable sensing such as lab-on-a-chip technique, it still suffers some disadvantages which keep it from a real point-of-care application. Most microfluidic techniques are based on PDMS or silicon as the sensing substrate, which involves a time-consuming fabrication process and is not sufficiently cost effective. Even if such a microfluidic chip could be finalized for mass production, the driving force for microfluid is absent. People still need to rely on external forces like cringer pumps to drive the fluid flow [22]. Other problems like channel clogging also brings up more challenges for robustness of the whole system [23]. The paper-based microfluidic technique has been on a trend to take over traditional microfluidics in recent years mainly because of its pump-free character [24], [25]. The capillary force within the paper fiber finally successfully gets rid of the bulky instrument. Its low cost, flexibility, ease of patterning and disposable properties make this approach a promising candidate for practical point-of-care applications [24]. There is much research on this paper-based sensing technique in most recent years for both optical and electrical bio-sensing.

The Whiteside group, who invented conventional microfluidic technique, still pioneered this area for paper-based sensing (see Fig. 2.3). They made their first paper-based micro-pad (PAD) as early as 2007, which implemented colorimetric sensing for glucose and protein [26] (see Fig. 2.3a). They then proposed three-dimensional paper microfluidic devices which enabled multiple testing simultaneously with high throughput. They also made it possible for new analytical protocols inexpensively without any external pumps [27], [28] (see Fig. 2.3b). Besides the colorimetric sensing, they achieve electrochemical sensing using paper microfluidic chips with electrodes embedded in the three-dimensional paper system. All the electrochemical voltammetry methods could be applied on this new disposable platform [29], [30] (see Fig. 2.3d).

Within these two recent years, more fabrication techniques and sensing principles were invented for paper-based microfluidic chips for bio-sensing (see Fig. 2.4). Rattanarat *et al.* proposed their implementation of combining electrochemical and colorimetric principle together for multiple ion detection (see Fig. 2.4a). This kind of device made use of the sensing prop-

erty of discrete ions, among which some are better for colorimetric testing while some can only be measured by special electrochemical methods like anode stripping [31]. Paper-based optical sensing was also achieved by Delaney *et al.* using electrochemical-luminescence through smartphone [32]. In 2015, the sensing target showed a transition from small ions or molecules to large cell, which is more cytological. Su *et al.* achieved cancer cell detection using electrochemical method which had the potential for portable early cancer detection [33] (see Fig. 2.4b). The principle is mainly based on the reaction between protein bio-marker and HRP. Besides the guided flow within paper which was normally used, the trapping and filtering property of paper began to be utilized as well. Recent attempts were reported to capture WBC on porous membrane substrate by physical trapping [34] or capture antibodies [35] (see Fig. 2.4d). The quantification method was based on imaging processing with either fluorescent dyes [35] or gold nanoparticles [34] labeling (see Fig. 2.4c).

2.5 Consideration for system design

Portable sensing technique is not just the art of sensors, but a whole picture of both sensors and sensor integration. This section is mainly focused on integration of sensors into portable systems.

In terms of fabrication, the most common process to make microfluidic channels is by wax printing or photoresist patterning [36]. As for more complicated structure like three-dimensional or stacked paper devices, double-sided tape or other hydrophobic material was often used [36].

In the electrical sensing system, power management and battery choice should be taken into consideration when designing the portable sensing system. Take electrochemical sensing as an example, in which the voltammetry potential range and corresponding sensing current range directly define the specs of the integrated circuits (IC). Those specifications include the supply voltage, frequency bandwidth, maximum current bias, common mode rejection ratio, and power signal rejection ratio. With functional IC determined, the ADC and DAC for data communication should be chosen according to the sensing accuracy needed. This requires complete investigation of the front-end sensor's sensitivity and limit of detection analysis. After finalizing all the

functional and data communication ICs, power management ICs like switch-mode regulators or LDOs should be chosen. The golden rule is to ensure highest efficiency and lowest ripple amplitude for the supply voltage. The battery should also be selected by considering the voltage range across the whole state of charge. Finally, the interface communication method should also be taken into consideration. There are generally three types of interface communication methods: audio jack, micro-USB and wireless (Bluetooth). Battery-free may be achievable only for the audio jack interface, but this also limits the signal types generated from such an interface. Further, the power consumption is difficult to regulate. The micro-USB interface usually needs an FTDI chip with bus protocols like UART, I2C or SPI, to communicate with a micro-controller. Data communication in this way is more reliable and usually can achieve the best power efficiency. The wireless method is more convenient than micro-USB, which can achieve remote sensing but, of course, is companied with more power consumption. Since the specific IC should be used for wireless communication, a micro-controller with suitable bus protocol is still necessary for such method.

In the optical sensing system, regardless of whether it is colorimetric or optical imaging, image processing technique is always the analyzing method. So the resolution and focal length of the camera should be verified after analyzing the sensing resolution and limit of detection from the sensor itself. Some mechanical fixture with an adjustable position may be necessary for adaptive focusing. Besides the detection component, the light source also plays an important role in portable sensing. Unlike the ideal light source used in a lab which often shows uniform intensity across a wide wavelength range, the light source for portable sensing are not uniform. So the emission spectrum should be analyzed first and some prediction should be made about its effect on the sensing results. Furthermore, the ambient light affects the camera performance a lot if a consistent light environment is not provided. The most common solution is to create a dark room with a diffusive reflection surface to make sure the camera only receives light from the sensor itself. Although some self-calibration method was used to cancel out the effect from ambient light, the settings for a camera at the software side should be very consistent.

2.6 Figures

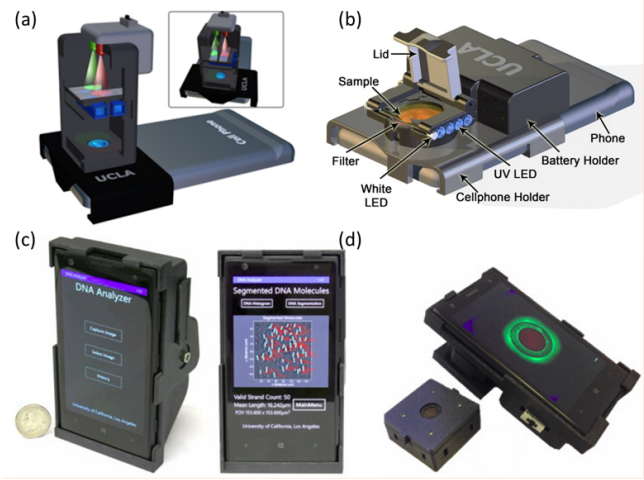

Figure 2.1: Collection of optical solution for portable sensing. (a) Smartphone based mercury sensor. (b) Smartphone based fluorescence sensing for rbST antibody. (c) Smartphone based microscope for single molecule DNA strand detection. (d) Field-portable and cost-effective fluorescence microscope for detection and quantification of Giardia lamblia cysts.

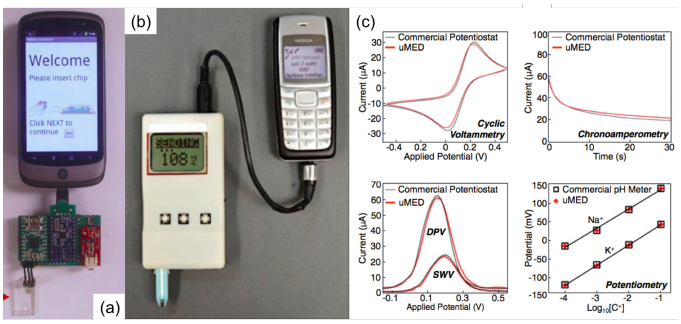

Figure 2.2: Collection of electrical solution for portable sensing. (a) Smartphone based amperometric sensing with microfluidic chip. (b) Universal mobile electrochemical detection platform using audio jack as communication interface. (c) Different voltammetry methods and testing waveforms from universal electrochemical detection platform.

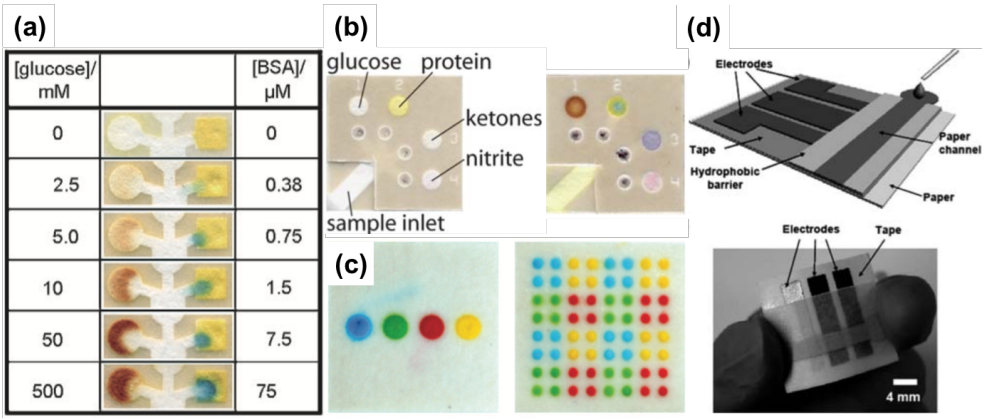

Figure 2.3: Collection of paper-based microfluidic sensing. (a) Paper-based micro-fluid chip for simultaneously detection of glucose and protein. (b) Two-layer paper structure for multi-target detection. (c) Three-dimensional paper structure for multi-target testing with high throughout. (d) Paper-based chip with embedded electrodes for electrochemical detection.

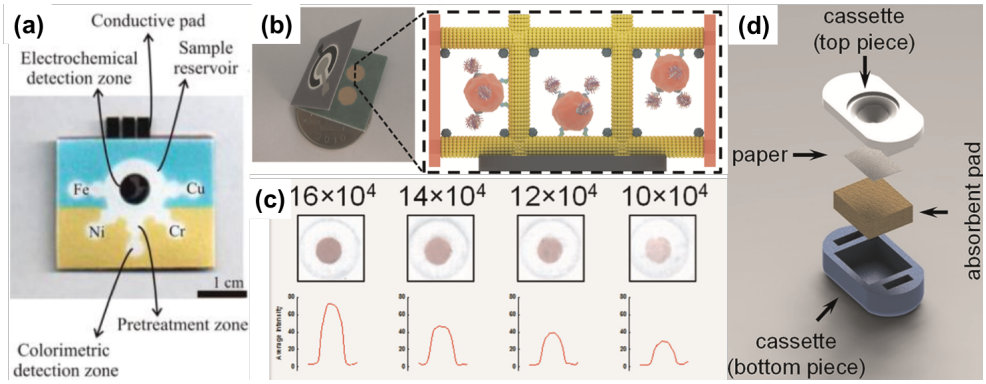

Figure 2.4: Most recent paper-based microfluid sensing. (a) Paper-based microfluidic chip for ion quantification with both electrochemical and colorimetric method. (b) Paper-based electrochemical chip for cancer cell detection. (c) Image processing method used for quantification of gold nano-particle density. (d) Setup for paper trapping and filtering.

CHAPTER 3

SMARTPHONE-BASED NANO-PLASMONIC SENSOR FOR COLORIMETRIC SENSING

3.1 Introduction

In this chapter a nano-cup array plasmonic structure is demonstrated with high sensitivity and colorimetric properties. Simulation with FDTD (Finite-Difference Time-Domain) is implemented to analyze the plasmonic resonance mode. The potential for its sensitivity in refractive index sensing is verified using glycerol. The enhanced scattering field at resonance mode is also utilized to amplify absorbance, which is later applied to colorimetric sensing for protein.

As we know, noble metallic nanostructures have been demonstrated to be used in the application of biological sensing [37], [38], imaging [39], [40] and energy harvesting [41], [42] in recent years, mainly due to the advantage of their unique plasmonic property. Noble metal shows collective electromagnetic resonance due to their negative refractive index in the visible range, which leads to surface plasmon resonance (SPR) or localized surface plasmon resonance (LSPR) [7], [43]. Both SPR and LSPR techniques are widely used for label-free biological sensing [44–47]. Compared with classical Krestchmann configuration, which involves complex prism integration [48], noble metallic nanostructure is more adaptive to be integrated in portable devices to achieve point-of-care applications [49]. Another advantage of plasmonic nanostructure is the ability to perform colorimetric sensing, generally due to its relatively large wavelength shift as refractive index changes. Although quite a few sensing devices have been demonstrated for refractive index sensing (resonance peak wavelength shift sensing), they suffer from either relative low sensitivity [47], [50] or resonance wavelength beyond visible region [9]. Compared with chemical binding-based colorimetric sensing [51], [52], plasmonic colorimetric sensing provides advantages such as faster readout [49],

elimination of chemical preparation or mitigating other limitations like vapor pressure and chemical flow control which brings additional complexities, for example, in colorimetric gas sensing [53]. In terms of point-of-care applications, several groups have developed portable platforms using commercial sensors and image processing method to do colorimetric sensing, but the sensor lacks lower limit of detection (LoD) as required for sensitive biofluids detection [18, 54, 55]. Further, in order to achieve repeatability and reliability in the measurements, the sensors require a reference sample (sensor with standard colorimetric properties) to account for the variation in light source intensity, type of light source, Bayer filter algorithm, and sensitivity of camera to incoming light.

Here we demonstrated a self-referenced portable nanoplasmonic imaging platform for colorimetric biomolecule sensing, by using image processing method under well-controlled optical imaging conditions. Unlike the classical extraordinary optical transmission (EOT) structure which usually gives rise to multiple spectrum features [56], the transmission spectrum of our plasmonic device has its single resonance wavelength in the visible light region [8]. We are able to demonstrate colorimetric sensing with a refractive index change due to its SPR and LSPR phenomena [8], [57]. The mechanism of improved limit of detection for biomolecules quantification is due to the matching of resonance wavelength of the sensor after refractive index changes to that of absorbance wavelength of the analyte. Absorbance is, thus, enhanced at this resonance wavelength under amplified electromagnetic intensity near the substrate surface [58]. The portable plasmonic platform showed about two-orders of magnitude improvement in sensitivity and LoD compared to other portable platforms using commercial chemical testing strips.

3.2 Material and methods

3.2.1 Plasmonic nanohole sensor

Norland Optical Adhesive 61 (NOA 61) was used as a UV curable polymer in this dissertation. NOA 61 is a transparent liquid photopolymer, which can be cured by ultraviolet light with maximum absorption within the range

of 320∼380 nm with peak sensitivity around 365 nm. Optically transparent and flexible polyethylene terephthalate (PET) film with the thickness of 250 μm was used as the substrate for the UV curing nanoreplica process. The UV curing process was done by Dymax 2000-EC UV curing flood lamp, which was designed to effectively limit output energy to longwave (UVA) for general purpose, low-intensity curing of UV adhesives, coatings, and inks.

Before the nanoreplica process, a glass master mode with nano-cone arrays was first immersed into dimethyldichlorosilane ($Si(CH_3)_2Cl_2$) solution for 30 minutes. The periodicity, height and width of the nano-cone are 350, 500 and 200 nm separately. The mold was then rinsed with DI water and ethanol to form a monolayer of saline on the surface. The hydrophobic saline surface helps the removal of UV-curable polymer (NOA-61) and ensures the validity of pattern transfer. After evenly spreading ∼10 μL UV-curable polymer on the nano-cone surface, constant UV light with power density of 105 mW/cm^2 was applied to the substrate for solidification. An E-beam evaporation system was used after replication for metal deposition on the polymer nanostructure. The deposition was performed in a sequence of Ti (9 nm) and Au (90 nm) with rate controlled at 1 Å/s to ensure uniformity. The nanostructure of nanoLCA is shown in Fig. 3.1a.

3.2.2 Glycerol

Glycerol (Sigma-Aldrich, for molecular biology, >99%) was used for measuring the resonance peak shift with the change of surrounding material due to its stable refractive index change with the solution concentration.

3.2.3 Coomassie (Bradford) protein assay reagent kit

In order to measure the concentration level of BSA, the Coomassie protein assay reagent kit (Thermo Scientific) was used. The Coomassie Protein Assay Kit is a quick and ready-to-use colorimetric method for total protein quantitation which was modified from the well-known Bradford Coomassie-binding. When Coomassie dye binds protein in an acidic medium, an immediate shift in absorption maximum occurs from 465 nm to 595 nm with a concomitant color change from brown to blue. It can be performed in either test tube

or microplate format. Protein concentrations are estimated by reference to absorbance obtained for a series of standard protein dilutions, which are assayed alongside the unknown samples.

3.2.4 BSA

Bovine Serum Albumin (BSA, Sigma-Aldrich, lyophilized powder, >96%) was dissolve in the DI water to simulate different levels of concentration for total protein testing.

3.2.5 Artificial urine sample

Urinalysis simulated urine kit was used to perform the practicality of sensing system for biological testing. The kit contains four different testing samples, which are labeled as control, patient A, patient B and patient C. Control was used as the reference to compare with three other samples, which had certain specific molecules exceeding the normal human body concentration. Patient A, B and C referred to glucose, protein and calcium under abnormally high concentration level, respectively.

3.2.6 Microplate reader

The Biotek Synergy HT microplate reader was used to prove the capability of the plasmonic nanohole sensor on self-referenced sensing. The Synergy HT Multi-detection reader is a robotic-compatible microplate reader that can measure absorbance, fluorescence, and luminescence.

3.2.7 Bradford array preparation

Standard microplate protocol was used for preparation. For the protein concentration within the range of 100∼1500 μg/mL, 5 μL of each sample was added into the appropriate microplate wells. The 250 μL of the Coomassie Reagent was then added to each well and mixed with plate shaker for 30 seconds. If the protein concentration was low (in the range of 1∼25 μg/mL), 150 μL of each sample was added to microplate wells, followed by 150 μL

of the Coomassie Reagent. After shaking for 30 seconds, all of the samples were incubated for 10 minutes at room temperature for the most consistent results.

3.2.8 Absorbance measurement with microplate reader

Absorbance spectrum (400∼800 nm) was measured for Bradford assay with and without nanoLCA substrate for comparison. The standard protein solution set prepared as reference has a concentration range of 0.001∼4 mg/mL. Absorbance at 595 nm was also measured for prepared assay with and without nanoLCA.

3.2.9 Smartphone platform setup

A portable platform was made for smartphone colorimetric sensing. Flat-surface white LED background was used to illuminate the sample area, assisting a camera at the top of the platform to capture uniform transmission image (see Fig. 3.1b). The testing sample was injected inside a PDMS (polydimethylsiloxane) micro-cavity embedded with a nanoLCA substrate at the bottom. The whole plasmonic device was supported by a piece of glass slide, which helped to remove/insert easily to the portable platform. Standard square color patterns (red (255,0,0), green (0,255,0) and blue (0,0,255)) were printed around the PDMS micro-cavity for color calibration. In order to block light underneath from transmitting the whole glass slide, a plastic sheet with printed black except the sensing and calibration regions was used to eliminate the interference of transmission light from the region besides sensing area. The glass slide with a sample was inserted through a sample slot at the side of the portable platform. The top of the platform could be adjusted horizontally in the X-Y plane while the height of the smartphone could also be adjustable to fit the focal length (see Fig. 3.1c).

An iOS application was used for capturing the transmission image from smartphone device. The application enabled the controllability on the values of camera settings as ISO, exposure time, white balance and gain factor, which helped to provide a consistent exposure condition in image analysis. The parameters for portable platform sensing were set as: ISO = 100; S

(exposure time) = 1/30 s; Gain = 1.5; white balance = 5100 K.

3.2.10 Numerical simulation

The electro-magnetic field distribution was analyzed by FDTD software from Lumerical Solutions, Inc. A TM polarized electromagnetic wave was set to propagate normal to substrate and the boundary condition was set periodic along x and y directions. The maximum mesh size around the metal particles was set 1.5 nm.

3.2.11 Image analysis method

Intensity of red (R), green (G), blue (B) channels was retrieved separately from the transmission image. The RGB values from tested sample were calibrated according to the standard RGB transmission images next to the sample. These standard RGB transmission images were only used to calibrate their corresponding channel.

3.3 Results and discussion

3.3.1 Portable colorimetric sensing using refractive index change

Due to plasmon-molecule interaction and increase in polarizability of the plasmons, a red shift in resonance peak is expected with the increase of refractive index of surrounding medium [8], [57] (see Fig. 3.2a). The resonance peaks in the transmission spectrum of the plasmonic sensor are mainly due to the surface plasmon polariton-Bloch wave (SPP-BW) mode [59], [60], [61] and localized surface plasmon resonance (LSPR) from the Mie scattering model [62], which has been discussed in our previous work [8], [57]. To characterize the performance (sensitivity) of the nanoLCA device on the portable platform, glycerol solutions with different concentrations (0%, 10%, 20%, 30%, 40%) were used to map surrounding refractive index range from 1.333 to 1.384 (expected range of typical biological fluids at low concentration).

The images taken from smartphone showed a color change to more bluish with the increase in glycerol concentration (see Fig. 3.2b). The RGB color space method was used here instead of HSV since HSV was applicable for a single peak wavelength shift device under a uniform light source; while neither the devices transmission spectrum nor the LED light source spectrum was so ideal in our case. The RGB channels were normalized according to the standard RGB color patterns captured on the same image. The equation for normalization (red channel for example) could be expressed as: $R_{norm} = \frac{R_{sample}}{R_{redpattern} \times 255}$. In order to cancel out the variation of light source intensity in every image, one more step normalization was performed as: $R'_{norm} = \frac{R_{norm}}{\sqrt{R^2_{norm}+G^2_{norm}+B^2_{norm}}} \times \sqrt{3 \times 255^2}$. This method acted as an internal reference and circumvented any effect of variation in light source intensity, type of light source, Bayer filter algorithm, and sensitivity of camera to incoming light on the acquired images. This portable platform showed good linear correlation with different concentrations of glycerol in RGB channels (see Fig. 3.2c). The normalized color intensity in RGB channels was mainly affected by light source spectrum, transmission spectrum of nanoLCA substrate and spectral sensitivity of RGB channels in the camera. Although blue channel displayed highest intensity owing to the sharp dominant peak at 450 nm from white LED (see Fig. 3.2d), the smallest amount of change was found because of relatively small change at the blue region in nanoLCAs transmission spectrum. The red channel should be most sensitive from the aspect of transmission spectrum, but the green channel actually showed highest sensitivity. The combination of the red shift of the transmission spectrum and red channel sensitivity should lead to an increase in red channel intensity, but it contradicted with the decrease in the red region from light source. The green channel, instead, showed a decrease trend in both spectral sensitivity and light source with the red shift in transmission spectrum, which made it the most sensitive channel for characterization.

3.3.2 Portable colorimetric sensing using absorbance enhancement

Firstly, absorbance enhancement of nanoLCA was verified with Bradford assay and BSAs on a microplate reader. Since the bound dye to protein in

Bradford assay has an absorption spectrum maximum at 595 nm, wavelength was fixed at 595 nm in the microplate reader to compare the absorbance with and without nanoLCA. The absorbance without nanoLCA shows its LoD (Limit of Detection) for BSA quantization at 0.1 mg/mL while the LoD with nanoLCA can achieve 0.001 mg/mL, which is 100 times more sensitive [63] (see Figs. 3.3a and 3.3b). It was already illustrated the transmission spectrum of nanoLCA with solution media showed a dominant peak at around 600 nm (see Fig. 3.2a). The absorbance enhancement is mainly due to this plasmonic resonance wavelength of nanoLCA in transmission spectrum matching with the absorbance peak wavelength of the bound dye in Bradford assay (595 nm in this case) [58]. The enhanced localized electrical field at resonance wavelength facilitates the additional light absorption of the bound dye.

Since the absorbance spectrum has its peak wavelength in red region, white LED with low red intensity is not a suitable light source. Another light source (halogen light) from Princeton Instrument with the peak around 600 nm was used to achieve higher image intensity (see Fig. 3.2d). The red channel should be the most sensitive channel and will be proportional to the concentration. So the intensity change of the red channel was applied to the image analysis on the portable colorimetric sensing platform. Bradford assay with BSA was added separately to the micro-fluid chamber on the portable platform, from 100 ng/mL to 10 mg/mL. The volume of micro-fluid chamber is only 20 μL, which is much smaller than the volume in 96-well plate (255 or 300 μL). The intensity of the channel was retrieved from an image taken by a smartphone and normalized (calibrated) using the standard color patterns around the sample area. Intensity of the red channel was normalized only with the standard red color pattern since the standard green and blue pattern show much less intensity, which is not stable and may cause larger error due to the noise. Normalized intensity of the red channel was scaled two times larger to enhance comparison and displayed in gray image (see Fig. 3.3c). It showed a linear correlation with the concentration in logarithmic scale (see Fig. 3.3d). The coefficient of determination (R^2) was 0.97. The intensity of red channel decreased with the increase of BSA concentration because of the higher absorbance in red color region. The LoD obtained in the imaging processing method was close to 0.01 mg/mL, which was larger than that obtained from the microplate reader. This is probably either due to higher

sensitivity of the optical sensor in bulk instrument or the shorter optical path compared with 96-well plate. The shorter optical path leads to much smaller change in transmission according to the Beer-Lambert law which illustrates an exponential relation between transmission and optical depth. In the comparison with the case without nanoLCA, it was demonstrated that higher sensitivity and better linearity can be achieved with nanoLCA (see Fig. 3.4). Compared with commercial protein testing strips which normally showed LoD at 0.3 mg/mL and sensitivity at 1 mg/mL, enhancement at about 30 times in LoD and 100 times in sensitivity was achieved on our portable sensing platform.

3.3.3 Application for urine testing

Protein concentration measurement in urine is often used as a criterion to identify proteinuria, a disease caused by kidney failure [64]. Four samples from artificial urine were used to simulate the identification of such kidney disease by a self-referenced portable sensing platform. These four samples indicate abnormal glucose, protein, calcium and reference, respectively. All of them were combined with Bradford assay using high concentration protocol and tested with the same procedure as described above. The intensity of red channel from the sample image was calibrated according to the standard red color pattern and scaled four times larger in gray scale to enhance comparison (see Fig. 3.5a). The retrieved color intensity from sample B looks darker than other samples. The normalized intensity from sample B is much smaller than other samples, indicating that sample B has a higher concentration of protein (see Fig. 3.5b). Therefore, this portable colorimetric platform provided a solution for quick diagnosis of kidney failure related diseases.

3.4 Conclusion

In summary, a self-referenced portable colorimetric sensing platform has been demonstrated. The system works on the principle of refractive index change and absorbance enhancement. In refractive index sensing application, characterization of sensor substrate was made using an image processing method by self-referenced normalization. The effect of the light source and spectral

sensitivity on intensity change was analyzed. It was shown that the most sensitive channel satisfies the same tendency in both light source and spectral sensitivity with a resonance peak shift in the transmission spectrum. In the case of absorbance enhancement application, Bradford assay was used to quantify protein concentration due to the match of absorbance peak wavelength of the dye with plasmonic resonant wavelength, where an electric field with a higher intensity near the substrate surface facilitated light absorption. Improvement of about 30 times in LoD and 100 times in sensitivity was achieved compared to other commercial protein testing strips. The urine test was then performed to show the ability of our platform to diagnose kidney failure by identifying protein concentration at an abnormal level. Our platform also showed potential and capability to adapt different light sources to target analytes with different absorption spectra for colorimetric sensing.

3.5 Figures

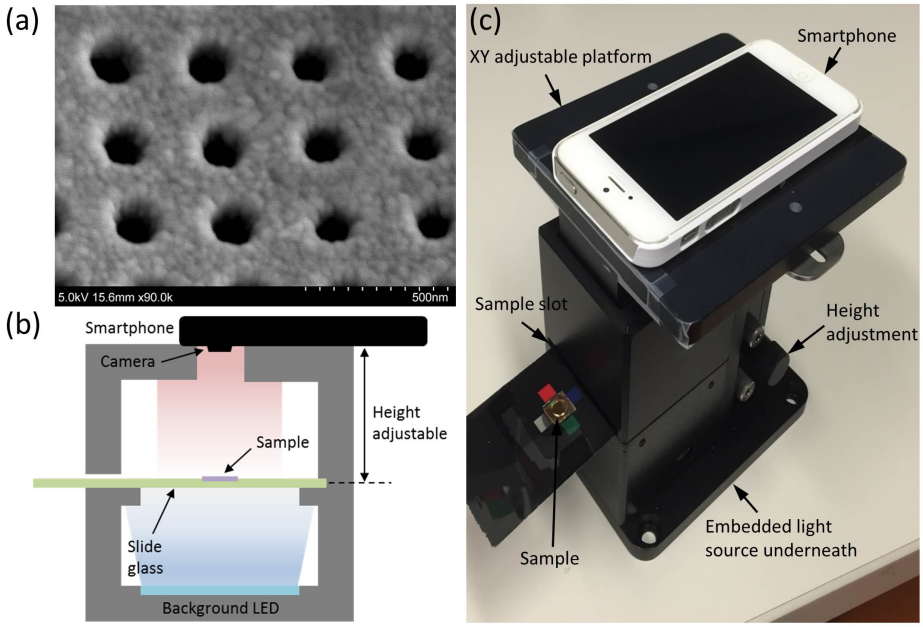

Figure 3.1: Smartphone based portable colorimetric sensing platform. (a) SEM image of nanoLCA. (b) Schematic of internal optical detection system setup. (c) Real image of optical detection setup.

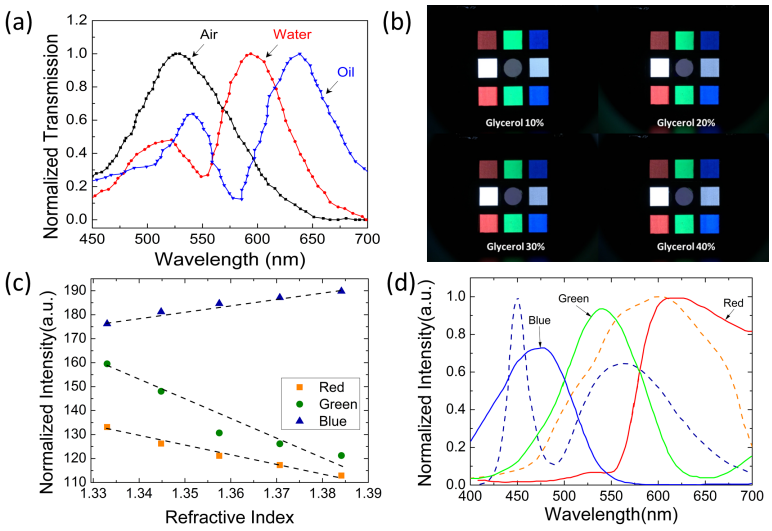

Figure 3.2: Sensing using refractive index change. (a) Normalized transmission spectrum of air, water and oil from nanoLCA. (b) Images taken from glycerol at different concentrations (10% $\sim$ 40%) on nanoLCA substrate from current optical platform. (c) Normalized intensity change of RGB channels with refractive index change when white LED was used as background light source. (d) Normalized spectrum of white LED and light source from Princeton Instrument. (The dashed blue curve was spectrum of white LED while the dashed orange curve was spectrum of light source from Princeton Instrument.) RGB spectral sensitivity (solid curve).

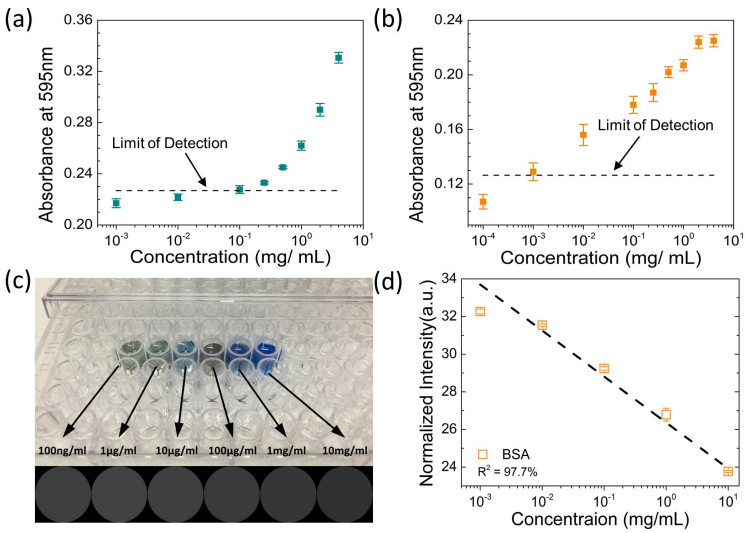

Figure 3.3: Sensing using absorbance enhancement. (a) Limit of detection without nanoLCA in terms of absorbance at 595 nm. (b) Limit of detection with nanoLCA in terms of absorbance at 595 nm. (c) Bradford assay test of BSA at varies concentrations (100 ng/mL $\sim$ 10 mg/mL) and corresponding intensity of red channel in gray scale. (d) Normalized intensity of red channel with the change of BSA concentration.

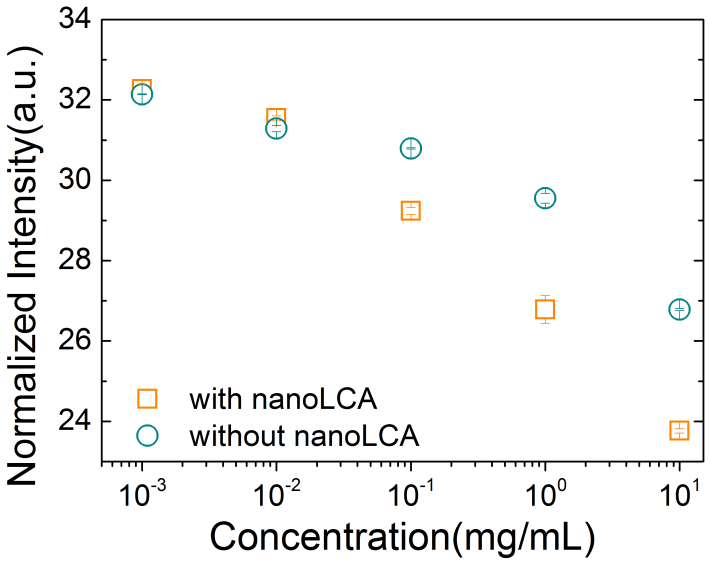

Figure 3.4: The comparison between cases with and without nanoLCA for protein (BSA) quantification on portable platform. Maximum intensity was normalized within these two cases. Results with nanoLCA showed higher sensitivity and better linearity.

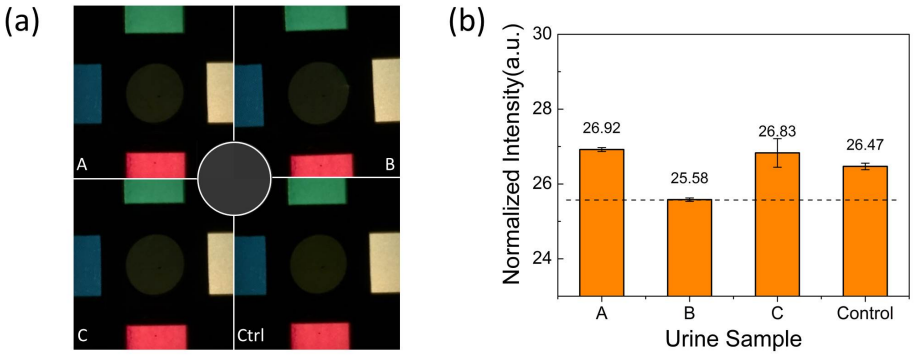

Figure 3.5: Urine sample testing. (a) Color images taken for urine sample testing and corresponding intensity (×4) of red channel in gray scale. (b) Bar chart of normalized intensity in red channel for different urine samples.

CHAPTER 4

SMARTPHONE BASED ELECTROCHEMICAL IONIC SENSOR FOR NITRATE QUANTIFICATION

4.1 Introduction

This chapter describes a portable platform with miniaturized three-electrode systems to do nitrate ion quantification. The novelty of this platform is the miniaturized sensor integration and the frequency modulation mechanism used for sensing through an audio jack. The motivation of portable nitrate sensing was first introduced, followed by specific experimental methods. The results were discussed in the last section.

Even though nitrogen is a vital part of living organisms such as amino acids, proteins and nucleic acids (DNA), excessive nitrogen has adverse health and environmental impact [65]. In the United States, the Environmental Protection Association (EPA) regulates the maximum allowable contamination level for nitrate as nitrogen (NO_3-N) to be 10 ppm (10mg/L) so as to prevent adverse health effects on population. Nitrite (NO_2^-), a reduced form of nitrate, is also a major cause of poisoning in fish and is toxic to human health as well. Therefore, the effective and accurate detection of nitrate concentration has become significant and necessary.

Currently citizens are not equipped to detect invisible contaminants in water as it requires specialized instrument, a certain level of expertise and is associated with high cost (equipment and chemicals) to measure them. In addition to the general public, people such as environmentalists, tourists and farm owners are often likely to determine the water contamination. So an easy-to-operate, low-cost and portable platform for nitrate detection is an unmet need. Moreover, a nitrate sensor operated by a mobile phone platform will be quite helpful in achieving mapped information of contaminants, since such information come with location and temperature information. Also, this data can be sent to a social platform normally connected to a cloud server

for wider dissemination.

Many existing methods, such as spectroscopic, chromatography, capillary electrophoresis and electrochemistry, are available to determine nitrate concentration [66]. The spectroscopic method is broadly used for nitrate determination, mainly using UV/Vis or fluorimetric emission [67]. This method normally involves the use of chemical reactions like Griess reaction to form highly fluorescent compounds to be compared and measured using a spectrophotometer [68–70]. The detection limit achievable by this method is in between 0.28 ppb and 28 ppb [66]. But multiple reaction steps make this method time consuming; also the instrument for fluorescence spectroscopic detection is not accessible to common citizens. Chromatography method, either gas chromatography or ion chromatography, is also commonly used in laboratory set-up [71–74]. Although the process is accurate, some experiment requirements like high pressure for HPLC (high-pressure liquid chromatography) and long column (200 mm) [72] makes it difficult to be miniaturized. The flow rate control of mobile phase is also sensitive to vibration or trembling and hence unsuitable for a portable device. Further, due to the associated high cost and large form factor, it is unlikely to be adopted by regular citizen for routine nitrate measurements. For capillary electrophoresis method, the column used is even longer and the set up for fluorescence detection is complicated [75], [76].

Compared with other methods, electrochemistry method is relatively easy to operate and can be transformed to a portable platform [66]. In electrochemical methods, due to the application of voltage potential between reference and working electrodes, oxidation or reduction of electro-active species happens [77]. Cyclic voltammetry is a popular method often used in electrochemistry systems [65], [78], [79] because of its ease of data interpretation. Miniaturized or microscale electrodes along with microfluidic integration greatly reduce the required liquid sample volume and will make the whole package portable [80].

Here we presented a lab-on-a-chip mobile sensing system (MoboSens), which includes a miniaturized electrochemical sensor, mobile phone platform (mobile phone application and controlling circuit) to control the sensor and microfluidics to handle the liquid samples. The use of a miniaturized electrode has several advantages such as low ohmic drop, low capacitive current, small time constant and fast mass transport [1], [81]. A user-friendly

mobile application interface is developed which enables a simple and easy-to-use testing procedure. Due to its lightweight (∼65 g) and small form factor, the whole system is portable. Unlike some smartphone-based sensing platforms developed previously [82], [83], our platform makes use of audio jack as the sensing interface instead of camera. The embedded camera on smartphone enables people to do image or spectrum analysis in the mobile application [13], [14], [17], [84], but the application is limited only to retrieving signal. The use of an audio jack can break through this one-way communication by setting a mechanism which will both send and retrieve signals, just like the way people listen to the music and record a voice. The use of micro-USB interface to perform electrochemical testing was made previously, but this could not achieve cross-platform testing easily because of the different protocol for different smartphones like Samsung (Android system) and iPhone (iOS system) [19]. In addition, an audio jack has been used to generate voltage excitation signal for electrochemiluminescence detection [32]. However, it suffers from cross-platform compatibility problems since the voltage value generated from an audio jack varies among different phones. Instead, what we generated and received from the audio jack is not the volume of sound but the tone frequency, which can break through this cross-platform limitation. This enables us to do different electrochemical testing by generating smooth waveforms. Recently, the audio jack was also used to send control signals from a phone to an external integrated potentiostat to perform different electrochemical tests [20]. In contrast, by making use of the CPU, ADC and DAC from the phone itself, instead of external electronic components, we are able to minimize the form factor and cost (∼ $10) of our package to achieve one handheld platform to do electrochemical testing. Currently, the smartphone-based system is designed for nitrate concentration measurement. Further development of the sensor is underway to include detection of other ions like phosphate or microbial contaminants like bacteria [85].

4.2 Material and methods

4.2.1 Design of MoboSens system

The schematic model of MoboSens is shown in Fig. 4.1a and Fig. 4.1b. A photograph of the complete package of MoboSens including the microfluidics, mobile apps and the controlling circuits is shown in Fig. 4.1c. Due to its uniformity in design and availability in all mobile phones, we decided to use the audio jack for the electrical signal input and output of the MoboSens system (instead of the USB port). Figure 4.2 shows the component level description of the MoboSens system. The sequence of events during the detection of nitrate using MoboSens are as follows: the sweep voltage required for driving the nitrate electrochemical sensor is first generated by the speaker D/A module in the mobile phone. The output voltage from the sensor is simultaneously retrieved by the A/D module embedded in microphone. In order to achieve frequency match between mobile phone and nitrate sensor, a circuit board with modulation and demodulation components is added to the MoboSens system.

A software platform in mobile phone is developed to drive and retrieve the data from the nitrate sensor. There is an option to perform real-time calibration or to use stored calibration curve for the nitrate measurements. The calibration measurements are performed using standard nitrate solutions with different concentrations. Finally, after measurements of the nitrate concentration of field water samples, the results can be shared (on social network like Twitter) or stored in remote server (for example, cloud server) for further analysis along with the information of geographical location (latitude and longitude), temperature and user inputs (meta data). The schematic of the entire system is shown in Fig. 4.2.

4.2.2 Sensor microfabrication

The miniaturized nitrate sensor is fabricated on glass substrate. The layout and image of sensor are shown in Fig. 4.3a and Fig. 4.3b. The electrodes are designed in a circular fashion to enable uniformity in the current flow in the electrochemical system. The surface area of counter, working and reference electrode are 9.05×10^{-4} cm^2, 7.05×10^{-4} cm^2 and 3.47×10^{-4}

cm^2, respectively. The area of counter electrode is designed to be the largest for preventing oxygen-bubble formation on its surface due to hydroxide oxidation at high current density [81]. The schematic of fabrication process is described in detail in Fig. 4.3c. We first patterned the counter electrode by optical lithography and deposited 200 nm gold by electron beam (e-beam) evaporation. After lifting off with acetone, the gold inside counter electrode region will be left. With the same method another layer of silver (200 nm) is fabricated as reference and working electrodes. Ag/AgCl is usually used as reference electrode, but it may also provide chloride contamination during nitrate detection. Instead, silver is used as reference electrode due to its simplicity in fabrication and sufficient stable potential in 0.1 M NaOH electrolyte [81]. It has been reported that silver has high sensitivity for reducing nitrate ions in alkaline environment [86], [87]. Although copper electrode also shows this good property in acidic solution [88], [89], it was found to dissolve during the reduction of nitrate [88]. That is why we chose silver as the working electrode here. For better adhesion on glass, one layer of titanium (20 nm) instead of chromium was deposited before gold and silver evaporation because chromium adhesion layer severely corrode during electrochemical activation process [81]. In order to minimize uncompensated resistance (R_u) between reference and working electrodes, these two electrodes are kept at close distance (10 μm) to increase accuracy. As an advantage of miniaturized electrode, this will directly result in much smaller cell time constant, which is the product of R_u and double-layer capacitance (C_d). A smaller cell time constant leads to the lower limit of experimental time scale.

4.2.3 Cyclic voltammetry method

The cyclic voltammetry method is used to obtain the reduction/oxidation reaction in the electrochemical system. The voltage sweeping range available for MoboSens is -1.6 V $\sim$ +1.5 V. Sodium hydroxide (NaOH) is used as electrolyte and sodium nitrate with different concentrations is added to the electrolyte for testing. The concentration of electrolyte (NaOH) is made to be 100 mM to eliminate the contribution of migration to the mass transfer of electro active species. The potential of hydrogen evolution will also be pushed to a more negative value at such an alkaline environment [90]. The

electrodes are first activated by sweeping the potential from -1.5 V to 1.0 V for 20 cycles (scan rate 1 V/s) with final potential at -1.5 V. This activation process will remove the possible oxidation layer at the surface of working electrode [82], [83], [91]. In order to avoid oxidation of silver working electrode and to make nitrate reduction happen, the sweeping voltage between working and reference electrode is chosen from 0 V to -1.5 V with a sweeping rate of 100 mV/s for cyclic voltammetry testing. This sweeping rate guarantees only 30 seconds for one cycle measurement without severe distortion which normally occurs at high sweeping rates due to an extra charging current from double-layer capacitance. We start from the cathodic sweeping because the reversal process is always less precise by referencing forward process which is uncertain in folded faradaic response [1]. The reduction peak of nitrate will be detected when sweeping toward -1.5 V. The whole testing involved four cycles and the data from the fourth cycle was used for calculation as the reduction peaks were stabilized in roughly three cycles.

4.2.4 Design of circuit board

Since there is a frequency limitation (which must be greater than 20 Hz) for input and output signals from both mobile phone audio jacks and microphones, a sine wave at constant amplitude with frequency increasing from 5300 Hz to 7600 Hz and decreasing from 7600 Hz to 5300 Hz is generated from mobile phone audio jack. The 5300 Hz is corresponding to 0 V while 7600 Hz is corresponding to -1.5 V. A frequency demodulation module is added to the circuit to convert frequency to voltage for sweeping voltage detection. This frequency demodulation mechanism enables MoboSens to break through the limitations of different types of smartphones without considering the different speaker volume settings. Since it is common to have some drift within FM chips and resistors, a variation of the order of 25 mV is expected when converting frequency values to voltages. The cyclic sweeping voltage is then added to reference potential and the working electrode is connected to ground which makes the input voltage between working and reference electrode varying from 0 V to -1.5 V and back to 0 V. Although the sweeping range could be -1.6 V $\sim$ +1.5 V, positive potential is avoided in case of oxidation of the silver working electrode. Integrated operational amplifiers

are used in circuit as potentiostat and a trans-impedance circuit is applied to convert the current to voltage. Since the frequency of this output voltage is low (which is below the detection limit of mobile phone microphone) and the amplitude is higher than the detection limit of the microphone input, a frequency modulation (FM) module is added to the circuit to convert the sensing data to the signal with the allowed frequency range of the microphone jack.

4.2.5 Software implementation

The software is operated on a Samsung make mobile phone with Windows Phone 7.5 OS (Android and iOS applications have also been developed; here, as an example, we describe Windows-based applications). The structure of software application is provided in Fig. 4.4. There are three layers from low to high, which are the basic functions provided by Microsoft, sensor API (Application Programming Interface) and user interface. The sensor API is the core of this platform, which packages functions provided by Microsoft and is called by users commands. In the user interface, there are four basic functions, namely, start, sensing, display and stop. The start function enables the sweeping voltage to drive the nitrate sensor; it also provides library of waveforms. The sensing function is mainly used to retrieve data from the output of nitrate sensor, and to analyze data including FM demodulation, down sampling and calibration. The display function is used for plotting the results for visualization. The stop function can be used for terminating these functions during operation.

4.2.6 Data processing

Since the raw data recorded by mobile phone platform is a series of square waves at different frequencies from the FM integrated circuit (CD4046), averaging of frequency data over a window is performed to obtain the raw data. The FM property of CD4046 was first characterized. Then a calibration method is employed to transform the frequency values to voltage values. The sampling rate of cellphone is 32000 bytes/s and each voltage value is stored as a short integer, so 16000 data points are recorded each second. The

output from CD4046 is a square wave with amplitude larger than 0.7 V, but the input/output to the microphone inside Windows phone is limited to 200 mV (this value will differ for different make of phones). Hence, the recorded wave is a truncated square wave with maximum and minimum values of + 32767 (215 for signed short integer with 16 bits) respectively. Frequency value is calculated by counting the number of steps from maximum to minimum by setting 1600 samples as one period. Calibration is performed to convert the output frequency from the frequency modulation integrated circuit into voltage and finally to oxidation-reduction current using trans-impedance circuit. Based on the frequency modulation module, the relation between current and frequency follow equation:

$$\mathrm{C}urrent(\mathrm{A}) = (\mathrm{f}requency \times 0.5627 + 0.3552 - 4.1)(\mathrm{V})/\mathrm{r}esistor(\Omega) \quad (4.1)$$

4.2.7 Sensor integration to mobile platform

The final packaging of the sensor is required for two reasons: portability and easy handling. In order to fulfill portability, a small circuit box was made attached with a light fixture frame fabricated using rapid prototyping manufacturing process. The fixture mechanism will make the circuit box stable when attached to a mobile phone. For ease in handling, a microfluidic chamber made up of PDMS is used. The microfluidic chamber was made hydrophilic by exposing it to oxygen plasma for 1 min and was bonded to the active region of the electrochemical sensor on the glass slide. The volume of the microfluidic chamber is about 7 μL. By virtue of the capillary design of the test chamber, the sample liquid will be automatically dragged into the microfluidic chamber by capillary action, when a sample is placed at the sensor opening to perform testing.

4.3 Results and discussion

4.3.1 Miniaturized nitrate sensor characterization

Nitrate reduction in alkaline media is either a two electrons (94%) or eight electrons (6%) process as given below [78], [79]:

$$NO_3{}^- + H_2O + 2\,e^- = NO_2{}^- + 2\,OH^- \tag{4.2}$$

$$NO_3{}^- + 6\,H_2O + 8\,e^- = NH_3 + 9\,OH^- \tag{4.3}$$

Standard testing samples with different nitrate concentrations from 100 μM (1.4 ppm NO_3–N) to 4000 μM (64 ppm NO_3–N) were first measured by a commercial potentiostat (CHI600) with a sweeping rate of 100 mV/s. The reduction current peaks were found around -1.35 V in Fig. 4.5a, which shows a linear relationship with concentration. The fact that the peak potential is more negative compared with previous experiments from other research groups [78], [79], [91], [92] can be attributed to more positive standard reduction potential of the reference electrode. This current peak is caused by the reduction of nitrate since the peak value increases with the increase of nitrate concentration. Since we used silver (Ag/Ag^+) as our reference electrode which acts as a pseudo reference electrode (not ideally nonpolarizable electrode), it showed modest drift (about 20 mV) at higher concentration of nitrate [81]. In order to quantify the effect of interference on nitrate detection due to common soluble anions like chloride, carbonate, sulfate and phosphate, the interfering ionic solution were mixed with the nitrate standard solution. Nitrate standard solution with a concentration of 250 μM was mixed with chloride, carbonate, sulfate and phosphate at the same concentration respectively. Figure 4.5b shows the similar location (-1.4 V $\sim$ -1.38 V) for nitrate reduction peak, with a coefficient of variation (CoV) of only 0.4%, which means the measurement is not interfered much by those interference ions. The CoV is calculated by taking ratio of standard deviation and the mean value. We found that the CoV for the magnitude of reduction peak current is only 1.7%, which indicates the accuracy of the sensor for measuring nitrate. This indicates the material of working electrode (Ag) and the

strongly alkaline environment shows higher selectivity to nitrate reduction.

The effect of electrolyte concentration was characterized by mixing nitrate standard solution of same concentration to the sodium hydroxide solution at different concentrations. In Fig. 4.5c, the positions of nitrate reduction current peak shifts from -1.35 V to -1.45 V while decreasing the concentration of sodium hydroxide from 0.1 M to 0.01 M. The main reason for such shift could be due to the increase of uncompensated resistance (R_u) between working and reference electrode as the electrolyte concentration is decreased by ten times [1]. So we keep the electrolyte concentration at 0.1 M to keep the reduction peak away from the sweep turning point (-1.5 V) for accuracy. Different pH value may also has some effect on the potential shift. Since the nitrate reduction process is irreversible [90], the peak potential where the peak current is could be expressed in theory as [1]:

$$E_p = E^{0'} - \frac{RT}{\alpha F}\left[0.780 + \ln\left(\frac{D_O^{1/2}}{k^0}\right) + \ln\left(\frac{\alpha F v}{RT}\right)^{1/2}\right] \tag{4.4}$$

where $E^{0'}$ is the formal potential of an electrode; R is gas constant; T is temperature; F is the Faraday constant; α is transfer coefficient; v is voltage sweeping rate; D_O is diffusion coefficient of oxidant; k^0 is the standard heterogeneous rate constant. It has been reported that the diffusion coefficient will increase with the decrease of pH value of the solution, especially with significant slope at low and high pH environment [93]. This can help explain the negative shift of peak potential shown in our experiments.

Further experiment was implemented to simulate the effect from soil water at different pH levels. Standard pH solutions containing same amount of nitrate varying from very strong acid (pH: 4.5 $\sim$ 5.0) to strongly alkaline (pH: 8.5 $\sim$ 9.0) [94] were dragged separately into micro-fluid chamber where sodium hydroxide solution at 0.1 M was pre-dried inside. Figure 4.5d shows about 30 mV positive shift of peak potential as the pH value increases, which indicates a wide coverage of MoboSens platform for soil water at different pH levels.

The temperature effect was also determined by adding nitrate solution at 1 mM from environment under 45 °C, 22 °C and 4 °C respectively in Fig. 4.5e. The coefficient of variation (CoV) is within 2%, which indicates temperature has little effect on the nitrate reduction current peak position.

Finally, repeatability of the miniaturized electrode was characterized by running cyclic voltammetry 100 times in nitrate solution at 1 mM in Fig. 4.5f. The nitrate reduction peak current began to stabilize after the 4th cycle. By analyzing data from the 5th, 40th and 80th cycle, the CoV was found to be 1.5%, which indicates this platform could be used for repeatable testing.

4.3.2 Measurement on MoboSens platform

Sodium nitrate solutions at different concentration (100 μM (1.4 ppm NO_3-N) to 5 mM (70 ppm NO_3-N)) with 0.1 M NaOH electrolyte medium were tested by the MoboSens platform. Figure 4.6a shows the recorded frequency changing with sweeping voltage. The frequency values were converted to voltage first, by using the linear voltage to frequency relationship shown in Fig. 4.6b. The current values were then calculated by dividing the resistance value of the resistor where the current pass through and shown in Fig. 4.6c. During the forward sweeping process (0 V to -1.5 V), there are current peaks which occur at around -1.35 V $\sim$ -1.4 V. The magnitude of the reduction current peaks is dependent on the concentration of nitrate present in the solution. The position of the reduction peak shifts about 50 mV to more negative value as the concentration of nitrate increases. This shift could be due to the existence of uncompensated resistance (R_u). Unlike commercial potentiostat which has a good control of $E+iR_u$ between working and reference electrode (E is the potential applied to working electrode); we controlled the true potential applied on working electrode. The practical effect of uncompensated resistance is to shift the reduction peak toward more negative potentials, especially in higher scan rate and higher concentration conditions which cause larger reduction current [1]. The small wide peaks around -0.9 V could be attributed to hydroxide desorption process on silver electrode [78], [95]. In the anodic sweeping process, an anodic current peak occurs at around -1.25 V, which is due to the electro-chemisorption of hydroxide ions [92], [95].

The calibration curve is obtained from the current reduction peak values after data processing in Fig. 4.6d. With linear fitting method, calibration equation could be written as:

$$\mathrm{C}urrent(\mathrm{A}) = -4.851 \times 10^{-7}\mathrm{C}oncentration(\mathrm{ppm}) - 4.397 \times 10^{-5} \quad (4.5)$$

The relation between reduction current and concentration shows linearity within the concentration range in 100 μM (1.4 ppm NO_3–N) $\sim$ 5 mM (70 ppm NO_3–N). The blue data points in Fig. 4.6d are measurement from standard nitrate solution while red data points are measurement from field water samples provided by Department of Agriculture at University of Illinois. The statistical error bar is based on four testing results using the same concentration. For the standard nitrate solution, samples with low concentration ($\sim$2 ppm) show larger standard deviation compared with samples having higher concentration of nitrate. Since there is always oxygen dissolved in solution, the deviation from linearity could be due to oxygen reduction. This reaction interferes with nitrate measurement by taking place at a more positive potential than nitrate reduction [78], [90]. We anticipate this effect will be more pronounced at lower concentration of nitrate ($<$ 2 ppm), and hence, will not challenge the reliability of sensor to measure nitrate at higher concentration ($>$ 2 ppm).

4.3.3 Field water sample testing

The field water samples are first filtered using a 0.1 μm Whatman filter paper to remove the suspended particles. For comparison, the concentrations of nitrogen in nitrate were measured by Dionex Ion Chromatography with a detection limit of 0.08 ppm. Figure 4.6d shows nitrate concentration of field water samples (red circle) measured by MoboSens platform and compared them with the calibration curve obtained with nitrate standard solution (blue square). The inset of Fig. 4.6d shows the comparison of MoboSens results with that of Ion Chromatography measurement for the same field water samples. The measurements are within $\pm$15% deviation at low concentration (2.2 ppm) and $\pm$5% deviation at high concentration (22 ppm). This verifies the ability of MoboSens platform to perform farm based field water testing.

4.3.4 Environmental water testing

In addition to the field water sample, MoboSens was utilized to measure nitrate concentration in environmental water samples. By adjusting the transimpedance from 20 kΩ to 100 kΩ, the detection limit could be pushed to

more diluted nitrate solution (around 10 μM (0.14 ppm)). The principle of trans-impedance is to convert current to voltage and voltage is converted to frequency as mentioned earlier. This adjustment is to fit a lower concentration range into a wide frequency range. Figure 4.7a shows the results of standard nitrate solution with low concentration (less than 1.4 ppm). The reduction current peaks are calibrated in Fig. 4.7b. Testing was then performed for environmental water samples. These water samples were collected from different sources like lakes, streams and local wells. The raw data was processed with the method described in Section 4.2.6 and the peak current was fitted into the calibration equation. To verify the accuracy of measurement results obtained using this mobile sensor platform, methods like cadmium reduction and ultraviolet (UV) absorption spectroscopy were performed for comparison [90]. The cadmium reduction method was based on the reduction of nitrate to nitrite on cadmium as a catalyst, followed by Griess reaction to form a fluorescent chemical. Cadmium reduction method is normally considered the gold standard for the detection of nitrate level. The UV absorption spectroscopy method was performed by scanning wavelength in a range from 190 nm to 450 nm. Nitrate concentration was calibrated from the absorption spectrum at different concentrations. The comparison of nitrate concentration of different water samples after calibration using the three different methods is shown in Fig. 4.7b.

From the results, the coefficient of variation (CoV) of nitrate concentration in crystal lake and lake of the woods with respect to cadmium reduction method is 4.1% and 4.7%, respectively. The concentration of nitrate ion tested by MoboSens from these two water sources is consistent with the cadmium reduction method. Water from streams and bored wells shows much lower concentration in MoboSens compared to other methods, especially a large CoV with respect to cadmium method. The large CoV is attributed to presence of nitrite in the sample as cadmium reduction methods convert nitrite into nitrate first and then measure the total nitrogen. Above all, the nitrate concentrations of all water samples were far below 10 ppm, which satisfied the requirements for water safety prescribed by EPA.

4.3.5 Network integration to the nitrate sensing

The application on a Windows phone is further developed to integrate the location of testing (longitude and latitude) to the nitrate sensing and displayed it on Bing maps. The temperature data is also included in the nitrate sensing. The phone application also enables users to add any metadata (such as user comments and graphics) along with the shared nitrate sensing information provided by the user. The user has the option to send this sensing data to social network sites such as Twitter for public dissemination or upload it to a secure cloud server for further analysis. An example of the developed phone application interface is given in Fig. 4.8. Figure 4.8a shows the main page of application. Figure 4.8b displays a plot from a testing result. In the interface showed in Fig. 4.8c, users will be able to send metadata along with the testing results. Figure 4.8d shows the location of the performed test on a Bing map. After sending metadata to Twitter, a message about nitrate information could be seen posted on Twitter website, as showed in Fig. 4.8e. Figure 4.8f shows the satellite view of the location where testing is performed with nitrate information labeled.

4.4 Conclusion

In summary, we have demonstrated an audio jack-based mobile sensing system for rapid and real-time nitrate concentration measurement. It contains a microfabricated three-electrode sensor, a mobile application and a circuit board developed for communicating with the sensor. The mobile sensing platform was used to test nitrate ion in field water as well as environmental water samples and compared with existing analytical testing methods. The mobile platform based sensing was found to be comparable with the traditional sensing methodology. Finally, the measured concentration value, location of testing site and metadata such as user inputs are communicated and shared at social network websites and secured cloud server for further analysis.

4.5 Figures

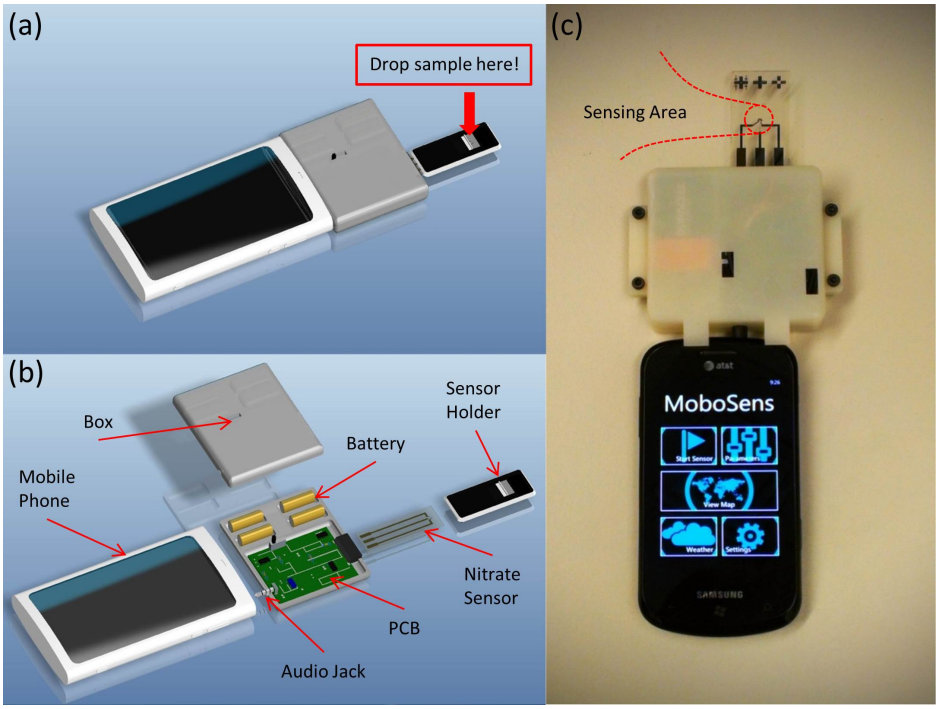

Figure 4.1: Concept design and real package of MoboSens. (a) Assembly view of MoboSens. (b) Detailed components of MoboSens. (c) Photograph showing the complete MoboSens system.

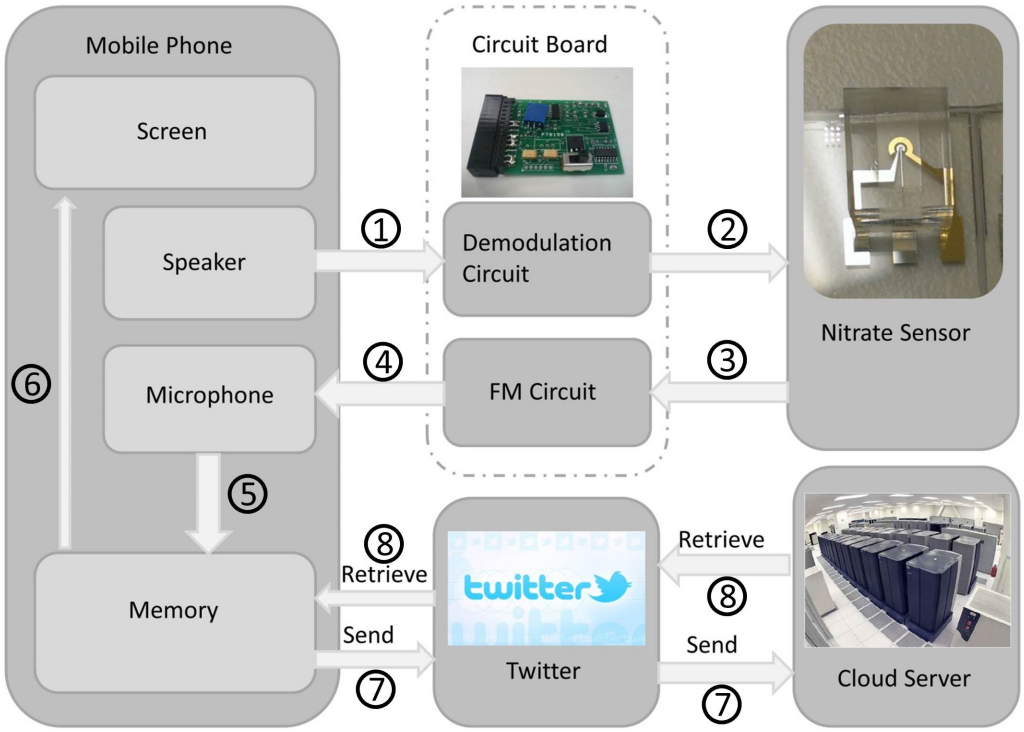

Figure 4.2: Schematic of operation of MoboSens system. (1) Signal with changing frequency is generated from speaker to demodulation unit. (2) Signal was demodulated to sweeping voltage for cyclic voltammetry testing. (3) The output current from miniaturized sensor was transformed to voltage and sent to frequency modulation unit. (4) Output signal from sensor was modulated to send to microphone. (5) Recorded raw data was transformed to frequency and analyzed in memory. (6) Frequency vs time plot was shown on mobile screen. (7) Analyzed results were sent to social platform (like Twitter) and stored by cloud server. (8) Information from cloud server or social platform could also be retrieved to smartphone for analysis.

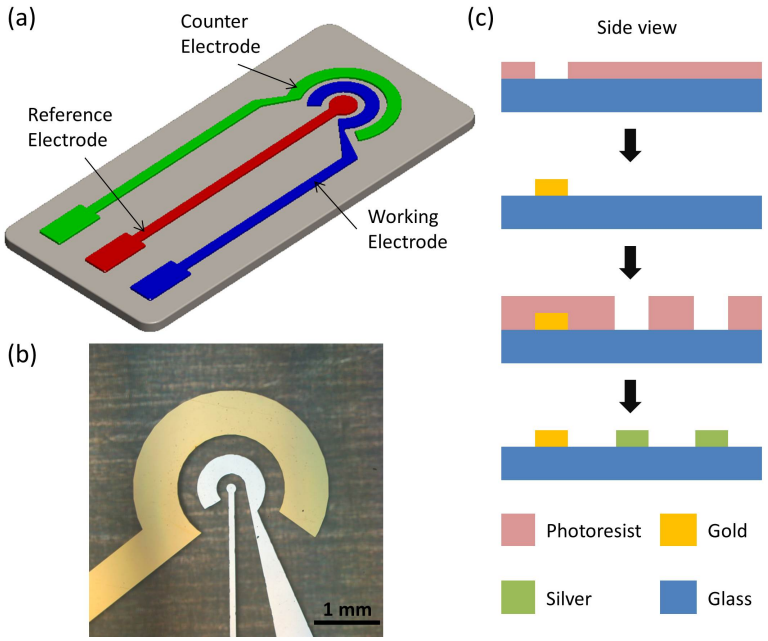

Figure 4.3: Sensor electrodes and fabrication process. (a) Schematic showing the three-electrode electrochemical sensor utilized in the MoboSens. (b) Optical image of the fabricated sensor electrodes. (c) Schematic showing the fabrication process involving series of photolithography and lift off to fabricate the electrochemical miniaturized sensor.

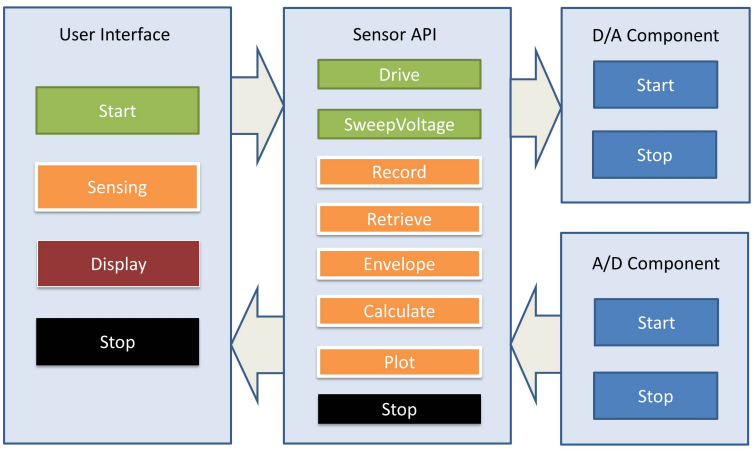

Figure 4.4: User interface and API structure. Four functions will be shown to users in the user interface while API functions in lower level are well defined to be called by the basic fourfunctions. D/A (play) and A/D (record) functions are called by API functions whenever signal transmission is needed through audio jack.

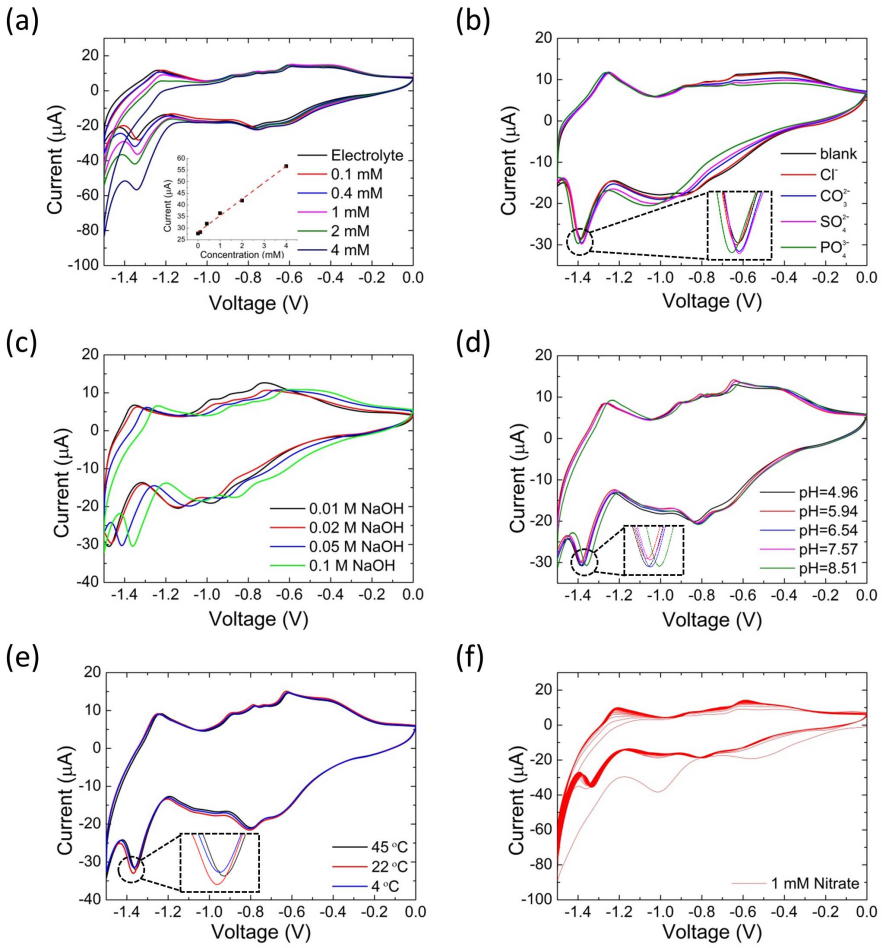

Figure 4.5: Characterization of miniaturized sensor. (a) Raw data and calibration curve of standard nitrate solution (0.1 mM $\sim$ 4 mM) using commercial potentiostat. The electrolyte (NaOH) concentration is 100 mM. (b) Effect of interfering ions: separate tests were performed by mixing NaCl (0.25 mM), Na_2CO_3 (0.25 mM), Na_2SO_4 (0.25 mM) and Na_3PO_4 (0.25 mM) solution to nitrate standard solution of 0.25 mM. The electrolyte (NaOH) concentration is 100 mM. (c) Effect of electrolyte concentration: cyclic voltammetry for 1 mM nitrate standard solution at different electrolyte (NaOH) concentrations (pH value: 12 $\sim$ 13). (d) Effect of pH of the test solution: cyclic voltammetry for 1 mM nitrate standard solution at simulated soil water pH environment showing little effect of solution pH on the reduction peak position. The electrolyte (NaOH) concentration is 100 mM. (e) Effect of temperature of the solution: 1 mM standard nitrate solution was tested under different temperature with 100 mM electrolyte (NaOH). (f) Stability of sensor: cyclic voltammetry testing was performed for multiple times (100 times). The sweeping rate for cyclic voltammetry method above is 100 mV/s.

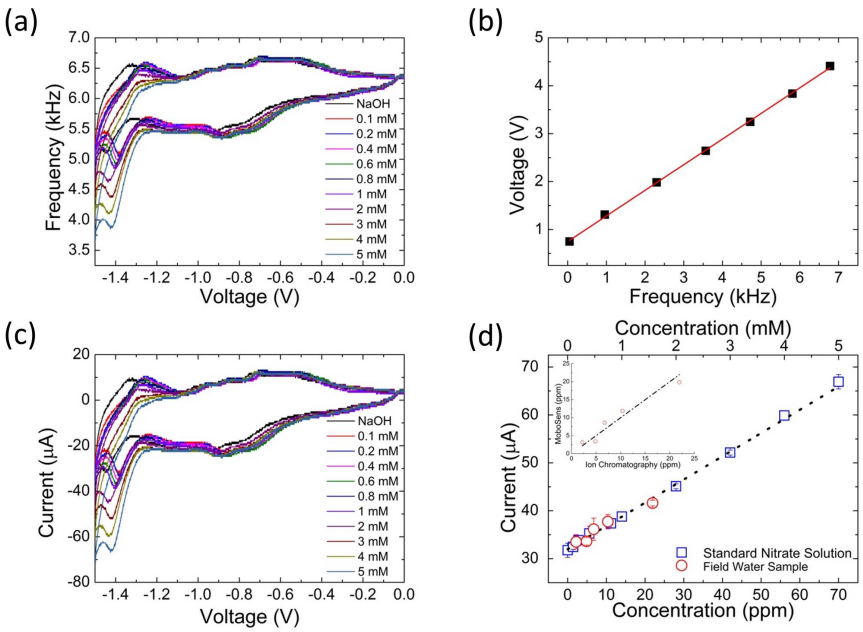

Figure 4.6: Measuring nitrate using MoboSens. (a) Raw data from MoboSens platform as frequency values. (b) Calibration curve of CD4046 to convert frequency values to voltage. (c) Cyclic voltammetry testing of standard nitrate solution at 0.1∼5 mM (1.4∼70 ppm NO_3–N) using MoboSens platform at a scan rate of 100 mV/s. (d) Measurement of nitrate concentration in field water sample using MoboSens platform. For comparison, the field sample data are shown directly on the calibration curve obtained from standard nitrate solution shown in (c). Inset of (d) is the MoboSens deviation from ion chromatography data by fitting experimental data into calibration curve. The electrolyte (NaOH) concentration is 100 mM.

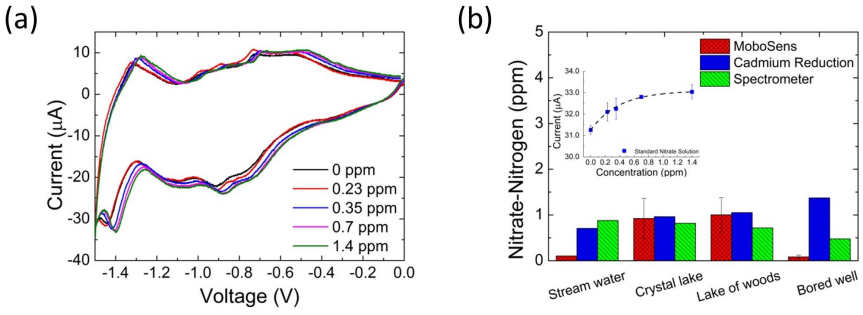

Figure 4.7: Limit of detection of MoboSens platform. (a) Cyclic voltammetry testing for standard nitrate solution at sub-ppm concentration using MoboSens platform at a scan rate of 100 mV/s. (b) Comparison of different analytical methods to measure nitrate concentration in environmental water sample. The electrolyte (NaOH) concentration is 100 mM.

Figure 4.8: User interface and network connection of MoboSens app. (a) Front page of the app. (b) Testing results plotted on the phone screen. (c) Interface showing the ability to input user metadata, along with the ability to pull publicly available data (e.g. USGS weather data) and showing them in one map. (d) Bing map interface with the current location of experiment shown on the map. (e) Message posted on Twitter website through the MoboSens platform. (f) Satellite view of recently posted data.

CHAPTER 5

SMARTPHONE BASED IMPEDANCE SENSOR FOR PRE-CONCENTRATED BACTERIA MEASUREMENT

5.1 Introduction

This chapter demonstrates a novel impedance sensor to quantify *Escherichia Coli* (*E. coli*) with two-layer filtering structure which pre-concentrates target bacteria. The portable system was achieved by Bluetooth communicating with a smartphone.

With the improving life quality in many developed and developing countries, citizens are more concerned about food and water safety [96] and eager to know whether their drinking water or food are contaminated by nitrate [90], harmful bacteria [97] or heavy metal ions [98]. Some species of *E. coli* and Salmonella bacteria have been known to have caused serious food and water contamination issues which can severely threaten civilians health conditions [99]. In order to quantify the amount of bacteria quickly, researchers have developed fluorescence detection techniques and DNA-biosensors to count *E. coli* [100] for various bacteria detections. However, fluorescence detection needs dye labeling [101] which requires high expense and professional training for operation. DNA-biosensor is also required to perform Polymerase chain reaction (PCR) as the first step [102] which is a complicated procedure in need of complicated facilities. So researchers also invented a series of label-free detection methods including quartz crystal microbalance (QCM) [103], microfluidic [104] and electrochemical methods [97]. Some of the techniques can detect the bacteria rapidly and accurately, however most of these detection methods have to be performed in specialized laboratory environments with the assistance of sophisticated equipment. Among these detection techniques, the electrochemical impedance spectroscopy (EIS) method is able to elucidate the electronic and physical properties of electrochemical systems including diffusion coefficients, adsorption mechanisms, capacitances, charge

transfer resistances, and electron transfer rate constants. Due to its sufficient sensitivity, simplicity and cost-effectiveness, it has been increasingly applied in bio-sensing with numerous methods in the past few years [105]. It has also been implemented as a label-free detection tool for quantification of bacteria with minimal sample preparations [106]. Additionally, by coating the electrodes with different antibodies, people used EIS method to detect different pathogens like *E. coli O157* [107]. However, high limit of detection and low sensitivity have prevented the application of EIS from being used practically in-field as a bacteria sensor. Meanwhile, microfluidic chips based measurement platforms which are affordable, portable and accessible to the public [108] have not been developed yet. Fortunately, as the smartphone is becoming more popular in our daily life, researchers have started to explore for the possibilities to make use of this powerful and portable platform for biological sensing.

In 2012, the smartphone is becoming more prevalent in the U.S. market with 115.8 million users accounting for ∼37% of the U.S. population, expected to rise to ∼61% by 2016. With the integration of GPS [109], powerful CPU, touch-screen displays, internet connection capability, and intelligent operating system [110], smartphones are able to provide extensive user-friendly services. Affordable smartphone peripheral devices with sensing capabilities will immensely help citizens to learn more environmental information like air and water quality at any location and at anytime [111], [112]. Bacteria sensing information collected by the phones can also be transmitted to cloud computing sites through 3G/4G networks for further data processing and establishing a participatory water-borne bacteria sensing map on the internet for information broadcasting.

In this chapter, we report the design, fabrication and integration of a low-cost, handheld, and sensitive microfluidic EIS bacteria pre-concentrator and sensor based on a smartphone through wireless connection. It enables smartphone users to detect the density of as low as 10 *E. coli* cells per milliliter of water. Our integrated microfluidic sensor has interdigitated sensing electrodes on micro-hole array silicon substrate and a sensing microfluidic chamber bounded by a nano-porous filter paper which is also used to preconcentrate bacteria in sample solutions. A specifically designed impedance network analyzer chip with a microcontroller together performs EIS measurement and analysis. An Android application program (App) has been

developed to enable recording and visualization of testing results as well as control of the sensor electronics. The real-time measurement data will be transmitted to a smartphone by a Bluetooth circuit module.

5.2 Materials and methods

5.2.1 Principle and design

The principle of our miniaturized bacteria sensor is EIS theory which has been developed and applied in bacteria quantification [107], [113], [114] for more than a decade. According to the Randles model, the equivalent circuit includes ohmic resistance (R_s) of electrolyte, Warburg impedance (Z_w) resulted by the diffusion of ions from bulk electrolyte to the interdigitated electrodes, electron-transfer resistance (R_{et}) and double-layer capacitance (C_{dl}) shown in Fig. 5.1a. R_s and Z_w represent the features of the electrolyte solution diffusion at the probe, while C_{dl} and R_{et} depend on the insulating and dielectric properties at the interface of electrolyte and electrodes and are affected by the property change occurring at the electrode interface. The distribution of bacterial cells between the interdigitated electrodes affects the interfacial electron-transfer kinetics thereby increase or decrease the electron-transfer conductivity in electrolyte environment. R_{et}, the electron transfer resistance is a parameter that can be observed at higher frequencies corresponding to the electron-transfer-limited process and can be measured as the diameter of the semicircle portion in the Nyquist plot in Fig. 5.1b. The intercept of the semicircle with the Z_{re} or the real axis at high frequency is equal to R_s. The linear part in Fig. 5.1b, which is the characteristic at lower frequencies, represents the diffusion-limited processes.

The design of multi-stage filtering is comprised of one layer of silicon chip having a large array of through holes with diameter of 10 microns and one layer of nano-porous filter paper with submicron pore size. Figure 5.1c shows the cross-sectional view of the integrated bacteria sensor. When the sample solution containing bacteria is injected from the bottom inlet, large particles in the solution will be blocked by the silicon filter while bacteria of our interest can go through the 10-micron-in-diameter silicon holes and are then blocked by the nanoporous filter, staying in the microfluidic sensing

chamber. The pre-concentrated bacterial cells distributed around the interdigitated electrodes are subject to impedance sensing. The entire integrated components are packaged by Polydimethylsiloxane (PDMS) material. Figure 5.1d shows the concept design of our packaged device. Users can take a certain amount of suspicious water sample which may contain bacteria into a syringe, and then inject the liquid through the channel as shown in Fig. 5.2a. Since all the bacteria are blocked by the filter and only 30 μL of liquid remains as a result of our geometric design, this sensor package allows users to pre-concentrate the bacteria solution before the measurement. The capacities of most standard syringes range from 1 mL to 60 mL, so we can pre-concentrate the bacteria by 10 to 2000 folds after excess liquid leaves the chamber from the outlet. Thus, our detection limit can be improved to as low as 10 bacterial cell per milliliter. The actual miniaturized bacteria sensor package is as large as one US quarter-dollar coin as shown in Fig. 5.2b.

5.2.2 Wireless system for sensor

A schematic diagram illustrating the main components of the wireless system is shown in Fig. 5.2c. Our wireless sensor system has been designed applicable for most of Bluetooth transceiver as well as for Android phones. Our system includes an Android cellphone (HTC ONE X), a Bluetooth shield (Seed SLD63030P), a micro controller (Arduino), a chip for impedance converter network analyzer (AD 5933), and our packaged sensor.

An Android App has been developed for users to set the start/end frequencies and the frequency sweeping step size in impedance analysis. The Connect button allows the cellphone to connect the sensor through Bluetooth. The benefits of Bluetooth connectivity include efficient power consumption of less than 10 mW [115] and standardization for smartphones and computers. Then Arduino microprocessor board generates corresponding commands according to the input parameters from the smartphone and asks the AD 5933 chip to send out sinusoidal signals to the bacteria sensor. Depending on the concentration of the bacteria, the corresponding signals acquired by the AD 5933 chip is sent back to the smartphone through the Arduino board and the Bluetooth shield. After this process completes, the smartphone App plots the impedance value with respect to frequency on the screen as shown

in Fig. 5.2c. It can also calculate a calibration curve after measuring several standard bacterial solutions, and then users can measure the bacterial concentration of an unknown sample.

Figure 5.2d illustrates the basic diagram of the wireless LCR sensing platform which communicates with the mobile phone through the Bluetooth and can drive our packaged bacteria sensor to quantify bacteria. Microcontroller writes commands to the impedance converter chip and passes the start/end frequency and sweeping step data from the cellphone to the chip. The on-chip oscillator module of impedance converter generates corresponding sinusoidal waves as the input signal of the bacteria sensor. The output signals of the bacteria sensor containing attenuated amplitude and phase change information are analyzed by an on-chip digital signal processor with 1024 points Discrete Fourier Transform. Real and imaginary parts of the results are sent to the micro-controller for converting into impedance and phase information. Eventually, these results are transmitted back to the cellphone through the Bluetooth and displayed on the smartphone screen. After calibration by standard solutions, our platform and app can provide accurate quantification information for tested bacterial solution.

5.2.3 Sensor microfabrication

The sensing part of miniaturized bacteria sensor is a pair of interdigitated electrodes fabricated on a piece of silicon chip with micro-scale through-hole arrays. Because interdigitated microelectrodes have advantages over conventional electrodes for analytical measurements including high signal-to-noise ratio, low resistance, small solution volumes requirement and rapid attainment of steady state [116], we adopt this design as the sensing part of our sensor in this research. The top view image of this part is shown in Fig. 5.3a. The diameter of the holes is 16 μm. The spacing between the electrodes is 20 μm while the width of the electrodes is 10 μm. Starting from 380 μm thick silicon wafer (University wafer 1815, p type, Boron doped, 4" 5$\sim$10 Ω), 1 μm of SiO_2 was deposited with Plasma-Enhanced Chemical Vapor Deposition system (PlasmaLab) first at 300 °C. Then, a layer of 100 nm Al_2O_3 which would be used as a hard mask for through holes was deposited uniformly and firmly on the SiO_2 layer by Atomic Layer Deposition (ALD) system (Cam-

bridge NanoTech) at 250 °C as what Fig. 5.3b① shows. Al_2O_3 deposited by ALD has been proved to be a good mask for fluoride based Si deep reactive ion etching (DRIE) in our experiment. The 100 nm Al_2O_3 allows ∼200 μm Si to be etched through. Then, photolithography and patterning were done with AZ 5214 photoresist and Karl Suss aligner as shown in Fig. 5.3b②. The 15 nm of Ti for adhesion and 200 nm of gold were deposited by electron beam evaporation (Temescal). After the metal on the photoresist was lifted off by acetone bath, the gold layer on the exposed region remained as the pair of interdigited electrodes as shown in Fig. 5.3b③. After the fabrication of electrodes, another layer of micro-hole array mask was aligned and patterned. The holes were located between the electrodes and were designed for the bacteria to pass through while blocking big dirt particles in water samples. Buffered oxide etcher (1:10 HF: NH_4F) was applied to etch the Al_2O_3 and SiO_2 (see Fig. 5.3b④, Fig. 5.3b⑤) hard mask. Then, XeF_2 etching (XACTIX) was performed on the back side of the silicon on the exposed part to thin down the silicon by half of its total thickness so that the micro-holes could be etched through by Bosch process with STS Advanced Silicon Etcher (see Fig. 5.3b⑥, Fig. 5.3b⑦) for only around 1.5 hrs.

5.3 Results and discussion

5.3.1 Concentration measurement

E. coli samples were provided by Institute for Genomic Biology from University of Illinois at Urbana and Champaign with the strain number of DH5a. The *E. coli* stock solution was centrifuged and rinsed with deionized water twice and diluted by 10, 100 and 1000 times respectively. The *E. coli* concentration for the stock solution is about 10^7 ml^{-1} measured by hemocytometer.

The prepared *E. coli* solution was injected into our device in the order of increasing concentration. To test the performance of packaged sensor electronics, a commercial LCR meter, Agilent 4284A, was used as the benchmark to measure the bacteria impedance by sweeping the signal frequency from 1 kHz to 1 MHz with 1 kHz step size.

Figure 5.4a shows the Nyquist plot of the results of bacteria impedance measurement. At low frequency the bacteria sensing is mass transfer con-

trolled, while at high frequency the bacteria sensing is kinetics controlled. In the kinetics controlled region, the diameter of the semicircle on Nyquist plot indicates the electron transfer resistance R_{et}. We found the relationship between bacteria concentration and electron transfer resistance in logarithmic form in Fig. 5.4b. The fitting formula is:

$$\log R_{et} = -0.153 \log C_{bac} + 4.187 \tag{5.1}$$

The electron transfer resistance R_{et} and bacteria concentration C_{bac} could be related by Randles equivalent circuit of electrochemical impedance spectroscopy. According to Fig. 5.1a and Fig. 5.1b, at high frequency, the Warburg impedance becomes negligible compared with R_{et}. Therefore, the Faradaic impedance could be simplified to only electron transfer resistance R_{et}. Due to charge-transfer kinetics, the electron transfer resistance could be defined as:

$$R_{et} = \frac{RT}{nFi_0} \tag{5.2}$$

where R is gas constant; T is absolute temperature; n is the number of transfer electrons; F is Faraday constant and i_0 is exchange current. In the theory of electrode kinetics, the exchange current at equilibrium condition could be defined as:

$$i_0 = FAk^0(C_O^*)^{1-\alpha}(C_R^*)^{\alpha} \tag{5.3}$$

where k^0 is standard heterogeneous rate constant. Since *E. coli* is negative charged in neutral pH environment [117], we can assume that electrons spread out on the surface of bacteria so that the movement of cells contribute to the electron transfer current. The concentration of bacteria could be expressed as:

$$C_{bac} = (C_O^*)^{\beta_1} = (C_R^*)^{\beta_2} \tag{5.4}$$

The exchange current could be simplified as:

$$i_0 = FAk^0 C_{bac}^{\beta} \tag{5.5}$$

In this case, the relation between electron transfer resistance and bacteria concentration could be expressed as: $R_{et} \propto C_{bac}^{\beta}$. Figure 5.4b displays this relationship from experimental data and parameter β equals 0.153, which is consistent with theoretical derivation. Furthermore, in the condition of high frequency, the semicircle in Nyquist plot could be expressed as the function of real part (Z_{Re}) and imaginary part (Z_{Im}) as:

$$\left(Z_{Re} - R_{\pi} - \frac{R_{et}}{2}\right)^2 + Z_{Im}^2 = \left(\frac{R_{et}}{2}\right)^2 \tag{5.6}$$

The imaginary peak point on the semicircle satisfies the relationship:

$$\omega = \frac{1}{R_{et} C_{dl}} \tag{5.7}$$

where ω is the voltage frequency while C_{dl} is the double-layer capacitance. By considering the Gouy-Chapman double-layer model, which involves a diffusion layer of charge in the solution, the double-layer capacitance can be related to bacteria concentration in logarithmic form as linearity. This relationship could be proved by the fitting curve in Fig. 5.4b.

Here is one issue worth noting. In most other journal articles for bacterial detection [114], the electron-transfer resistance (R_{et}) increases as the concentration of bacteria increases. However, our testing data show that R_{et} decreases as the bacteria concentration increases. To explain this phenomenon, we need to review Fig. 5.1a where R_s is the ohmic resistance of the electrolyte. In other cases, researchers used conductive electrolyte like $1\times$ Phosphate-Buffered Saline (PBS) whose high conductivity is associated with low R_s. In those models [114], antibody-treated electrodes trapped bacterial cells close to the electrodes and the double-layer of lipid bilayer membrane of the cells retarded the electron transfer in the electrolyte. As a result, R_{et} increased while the concentration of cells increased. In our case, deionized (DI) water (18 MΩ) was applied to dilute *E. coli* bacteria after centrifuging and rinsing from culture medium before testing, since *E. coli* at around neutral pH environment carries charge [117], higher concentration of *E. coli* induced resistance R_{et} lower than the resistance of electrolyte, R_s.

The reason why we used DI water as the background solution to detect the concentration of bacteria is that our project investigated a new method for direct detection and quantification of bacteria on mobile detection platform in

no need of pretreating field water samples, like centrifuging and diluting with 1× PBS and other redox molecule additives like $[Fe(CN)_6]^{3-}/[Fe(CN)_6]^{4-}$. Current result is a proof of concept to find the correlation between bacteria concentration and EIS in natural waters.

5.3.2 Smartphone software application

The software was developed on the Android operating system. Implemented with multiple functions of sending sensor control commands, receiving data and plotting, this software is able to remotely control microcontroller (Arduino) through a Bluetooth Shield transceiver board. Connected with the miniaturized bacteria sensor, the smartphone App is able to implement the same functions as a commercial LCR meter does. The user interface of the App is shown in Fig. 5.2c.

In order to characterize the sensing capability of the smartphone bacteria sensor system, we have performed the tests with different concentrations of *E. coli* solutions and measured impedance spectra by sweeping the frequency from 2 kHz to 100 kHz, as shown in Fig. 5.5a. Figures 5.5b and 5.5c show the magnified chart of Fig. 5.5a. We diluted the stock bacteria solution into different concentrations and used a 60 mL syringe to let 60 mL of calibration sample solutions with the cell concentrations of 10 mL^{-1}, 100 mL^{-1}, 1000 mL^{-1}, and 10000 mL^{-1} to pass through the sensor. A Nyquist diagram was plotted on the smartphone screen as the thin lines in Fig. 5.5b. Then the program can automatically extract the R_{et} value by calculating the peak imaginary resistance from the curve in Fig. 5.5b and plot the R_{et} versus *E. coli* concentrations diagram as shown in Fig. 5.5c. A blue fitting curve has been derived as:

$$y = 79249x^{-0.21} \tag{5.8}$$

where x is the concentration of *E. coli* and y is the imaginary impedance peak, R_{et}.

Then we performed a measurement of prepared bacteria solution with calculated concentration of 333 cells per milliliter. The result is shown as the thick orange curve in Fig. 5.5b, where R_{et} equals 25727.4 Ω which is plotted as the green cross in Fig. 5.5c. According to the fitting curve, the measured

concentration is 212 cells per milliliter so that the relative error is 36.4% with respect to the actual concentration. Note that this tested cell concentration is extremely low with less than one cell per microliter.

One difference between the Nyquist plot results obtained by the bench-top LCR meter and those acquired by our wireless impedance sensing platform is the shape of the curve. First, the linear part disappeared in our sensor. Because the linear part represents the diffusion-limited process and corresponds to low-frequency response. While the bench-top LCR meter can sweep frequency starting from 1 kHz, our wireless impedance sensor starts sweeping from 2 kHz where kinetic control dominates. Second, since the upper frequency limit of the bench-top LCR meter is 1 MHz and that of our wireless sensing platform is only 100 kHz, the measurement results in the Nyquist plot converge to the origin for the bench-top equipment measurement but not for the wireless sensing platform. When we use R_{et} for calibration, because R_{et} peak for concentrations of bacteria higher than 1000 cells mL^{-1} will fall out of the measurable frequency range, this instrument limitation shrinks the upper dynamic range to 1000 cells mL^{-1}. As the R_{et} peak exists for low concentration solutions, the limit of detection is not degraded.

5.4 Conclusion

In summary, we have performed the design, fabrication and testing of a low-cost, miniaturized and sensitive wireless bacterial sensor that can preconcentrate bacteria solution to obtain a detection limit of as low as 10 cells per milliliter. In order to enable citizens to perform EIS measurement conveniently and understand whether their drinking water has been contaminated, we designed and tested a smartphone-based miniaturized impedance spectroscopic measurement platform with Bluetooth connectivity. We have used commercial bench-top LCR meter to benchmark the performance and stability of our bacteria sensor. Additionally we integrated our sensor with the wireless impedance sensor platform to conduct a natural water sample testing after calibration. The limit of detection for the bacteria sensing is 10 *E. coli* cells per milliliter and its dynamic range is from 10 *E. coli* cells mL^{-1} to 1000 cells mL^{-1}. We compared the measured *E. coli* concentration with the actual cell concentration, and got the result on the same order of

magnitude with an error of 36.4%. Finally, we have also proved that our Android app in the smartphone worked properly with our low-cost wireless impedance bacteria sensing platform, which enables smartphone users to measure bacteria contamination in their daily-used water conveniently and cost-effectively. Moreover, the same wireless sensing platform and multi-stage pre-concentration filtering sensor package can be extended for specific pathogen detection by coating antibodies on the electrodes where users can detect the concentration of each kind of bacteria with a single device after performing one test.

5.5 Figures

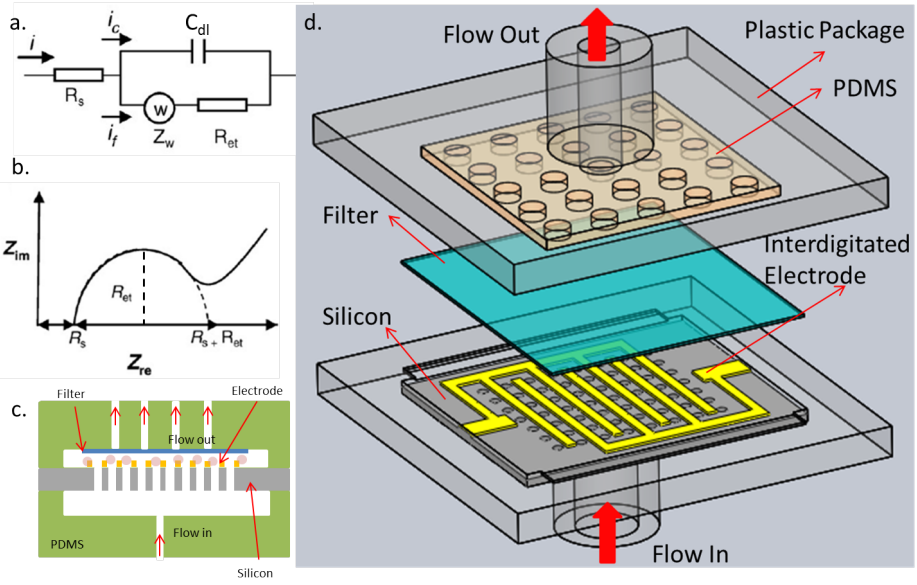

Figure 5.1: Electrochemical Impedance Spectroscopic (EIS) sensing principle. (a) Randles equivalent circuit of EIS. (b) A typical Nyquist plot for EIS. (c) Cross-sectional view of the integrated EIS bacteria sensor. Bacteria will pass through micro-hole silicon filter and be blocked by nonporous filter above the interdigitated sensing electrodes. (d) 3D model of the EIS bacteria sensor package.

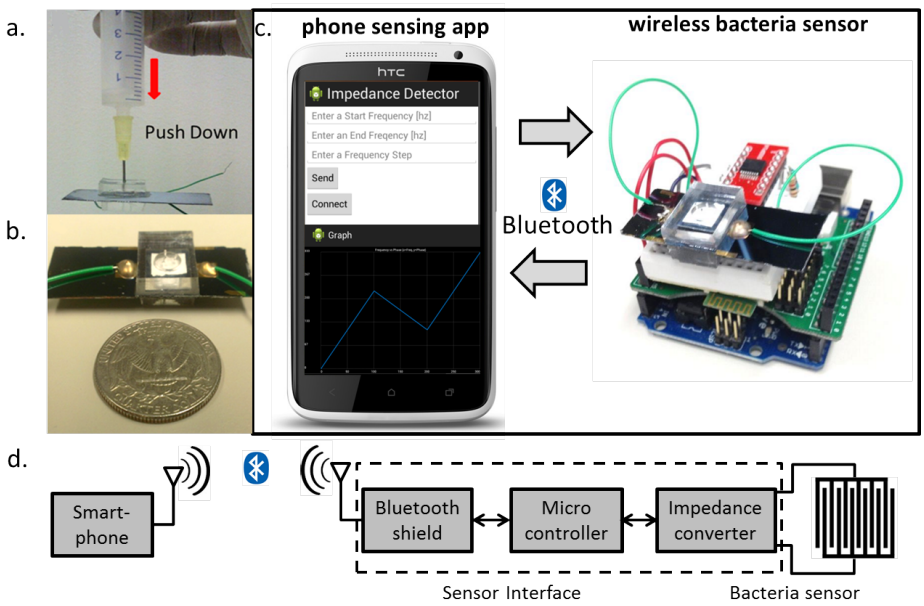

Figure 5.2: Wireless mobile phone bacteria sensing system. (a) Picture showing syringe injection of testing liquid into the sensor package. (b) Close view of the EIS bacteria sensor package. (c) Picture showing communication scheme between smartphone sensing app and wireless bacteria sensor. (d) Diagram of wireless sensing system.

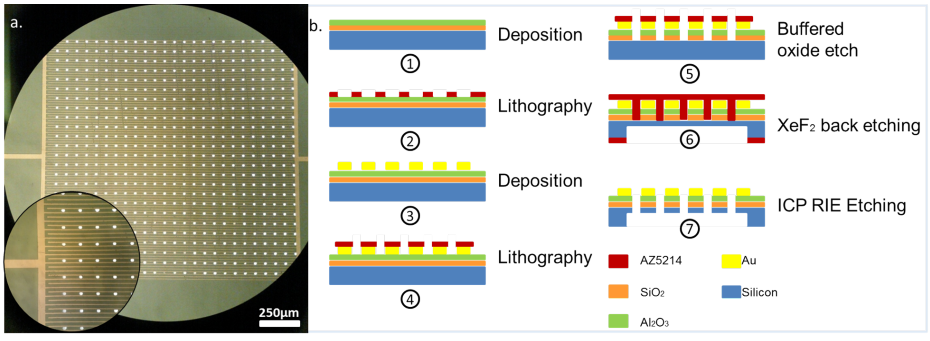

Figure 5.3: Sensor micro fabrication. (a) Top view microscopy images of the micro-hole array and interdigitated electrodes. (b) Fabrication process of the silicon sensor chip.

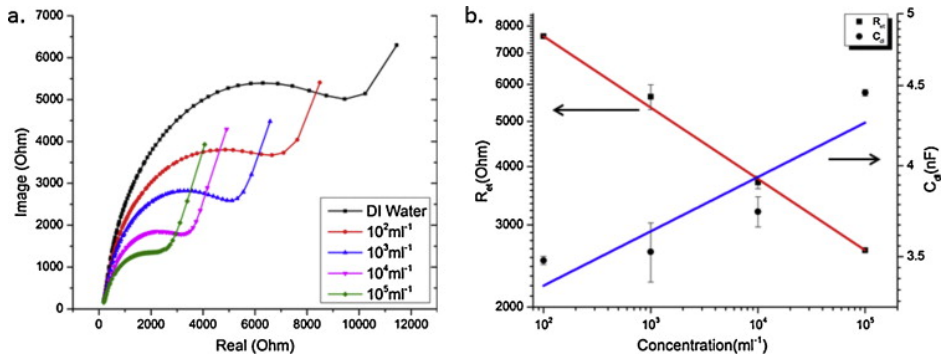

Figure 5.4: Two methods of concentration measurement using EIS bacteria sensor. (a) Nyquist plots (real and imaginary parts of the complex impedance) of bacteria solutions at different concentrations. (b) Logarithmic calibration between electron transfer resistance (R_{et}) and concentration and fitting curve (red line) and logarithmic calibration and fitting curve between double-layer capacitance (C_{dl}) and concentration (blue line). (For interpretation of the references to color in text, the reader is referred to the web version of this article.)

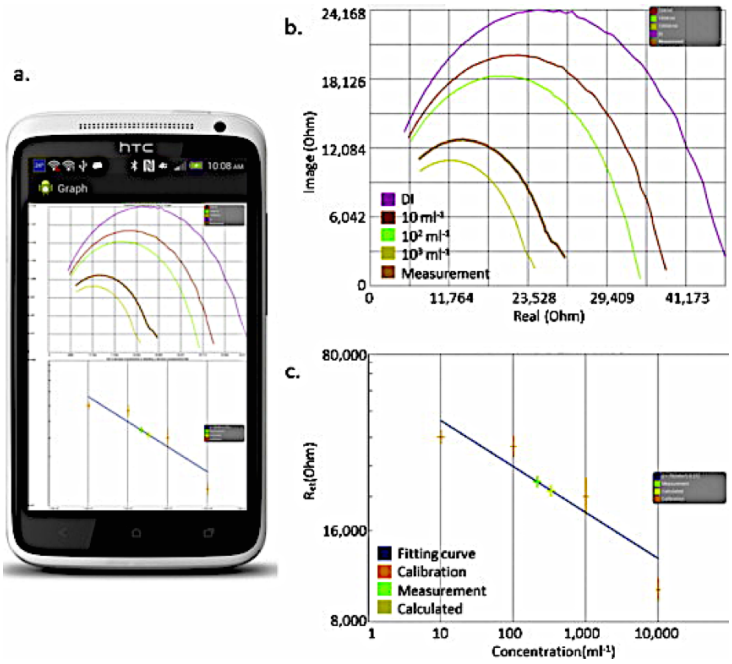

Figure 5.5: Calibration and sample measurement by the wireless cellphone bacteria sensing system. (a) Cellphone display of the impedance measurement results. (b) Zoomed-in image of Nyquist plots on the cellphone, with four solutions of known bacteria concentrations used for sensor calibration, DI water and one sample solution to be tested. (c) R_{et} vs concentration plot and the fitted calibration curve. The *E. coli* concentration of the unknown sample was derived from fitting the measurement results into the calibration curve and corresponding formula, as the green cross shows; while the yellow shows the calculated (actual) concentration and corresponding R_{et}.

CHAPTER 6

PAPER-BASED ELECTROCHEMICAL SENSOR FOR CELL AND BACTERIA QUANTIFICATION WITH SMARTPHONE

6.1 Introduction

Although the pre-concentration property makes the bacteria quantification easier, there are still some problems with that platform for real point-of-care application. The fabrication process for the sensing platform is too labor intensive and the electrolyte as distilled water is not quite stable for electrical sensing. The chapter here demonstrates an innovative paper-based porous electrode, which makes use of physical adsorption and diffusion block mechanism for quantification sensing.

White blood cell (WBC), also called leukocyte, originates in the bone marrow and circulates throughout the bloodstream. WBC is the main effector cell in the immune system. The main physiology function of WBC is to fight infections from bacteria, viruses, fungal that invade the body. The normal range of WBC is $4500 \sim 11500\ \mu L^{-1}$ [118] in healthy condition, while in pathology condition, the number will be out of this range. The case when concentration is higher than $11500\ \mu L^{-1}$ is called leukocytosis [118], which is mostly caused by bacteria infection instead of viral infection [119], [120]. Accordingly, WBC is a cell marker to discriminate the early diagnose of bacteria or viral induced infection and impact the therapy decision the antibiotic therapy or antiviral therapy [121]. The case when WBC concentration is lower than $4500\ \mu L^{-1}$ is called leukopenia [118], which is commonly caused by medical intervention such as long-term use antibiotics [122] and chemotherapy in cancer [123], [124]. In order to perform safe treatment, WBC concentration needs to be frequently checked to monitor the side effect of chemotherapy and adjust treatment plan, just like glucose management in patients with diabetes mellitus. WBC count provides high diagnosis value in acute infections and chronic disease management. Therefore WBC counting becomes

a routine in clinical testing [118] and it is in high demand to have a rapid, easy-to-use, low cost WBC counting point-of-care system in order to meet this significant diagnostic need.

Traditionally WBC counting is done by using hemocytometer under microscope [125] but this method has limited point-of-care applications. Automated high-efficiency WBC counting were achieved for clinical use [126] by measuring the optical scattering [127], fluorescence labeling [128] or electrical impedance of WBC [129]. Such automated hematology analyzer requires bulky instrument and trained operators, which limits the use for point-of-care applications especially in developing countries with limited resources and thus demands a miniaturized portable hematology analyzer. Several miniaturized platforms for WBC counting have been achieved with microfluidic separation and collection of WBCs however are still lack of system portability because of the use of microscope as detection system [130–132]. WBC counting on microfluidic electrical impedance sensors based on Coulter principle [129] suffers channel-clogging problem and compromised system robustness [22], [23]. External bulky equipment for liquid pumping and signal acquisition in the aforementioned microfluidic systems limit their application to only laboratory benchtop settings.

Paper (membrane) based liquid sample handling approaches overcome many drawbacks in traditional microfluidic technique and realize pump-free microfluidic flow owing to the capillary force along the paper fibers [24], [25]. Its low cost, flexibility, ease of patterning and disposable properties make this approach a promising candidate for practical POC applications [24], [25]. Most paper-based microfluidic devices have been coupled with the optical colorimetric [133] or electrochemical method [134] to quantify ions [31], [135] and small molecules such as glucose [29], DNA [136], [137] or proteins like cancer bio-marker [33], [138]. But they suffer from delivery problems limited by pore size when applied to large particles like WBC. Recent attempts were reported to capture WBC on porous membrane substrate by physical trapping [34] or capture antibodies [35], and quantify using the imaging process with either fluorescent dyes [35] or gold nanoparticles [34] labeling which adds to the complexity of these attempts. Our work takes the advantages of both the physical property of membrane substrate and ease of electrochemical method at the same time to achieve label-free WBC quantification.

As the most widely used mobile device in the world, the smartphone is

continuously advanced in computing, information collection and data sharing capabilities, making it an ideal portable receiver by nature for point-of-care applications [139–141]. Colorimetric sensing using image analysis is one of the most common methods can be applied to paper-based applications [18, 142–145]. But owing to variations under different test conditions, more consideration needs to be taken on self-reference and calibration to obtain accurate results [54]. Electrochemical sensing instead is easy to be made compactable to smartphones using audio-jack [91], micro-USB [146] or Bluetooth [85] communication interfaces.

We, therefore, for the first time propose a paper microfluidic sensor coupled with smartphone electrochemical measurement for label-free WBC counting. The physical trapping of WBC was implemented on our polyvinylidene fluoride (PVDF) membrane with microfabricated interdigitated electrodes and analytical ion probes (ferricyanide/ferrocyanide) were used for electrochemical quantification. The electrochemical impedance spectroscopy (EIS) method was often used for such electrode surface analysis on planar solid substrates [114], [147], [148] but not effectively on porous substrates. Considering the porous property of the membrane electrodes which provides plenty of charge transfer pathways, the differential pulse voltammetry (DPV) method was used to quantify diffusion blockage by trapped WBC. Based on our previous efforts on smartphone-based platforms for electrochemical sensing [21], [85], [91], we implemented a handheld smartphone DPV measurement system through wireless Bluetooth communication and thus made it ready for point-of-care applications. The dynamic range of our portable system covers three orders of WBC concentration ($10^2 \sim 10^4$ μL^{-1}), which enables point-of-care diagnosis even in leukopenia and leukocytosis cases.

6.2 Materials and methods

6.2.1 Electrode fabrication

Our sensor used three-electrode system for electrochemical testing which was designed using AutoCAD2011. The designed pattern was cut open on planar acrylic material with laser cutting tool (Universal Laser Systems X-600) as a shadow mask. The total sensing area for one electrode is about 1 cm^2 and

the width of interdigitated electrode is 500 μm. Metal evaporation deposition (CHA SEC-600 E-Beam Evaporator) was used to deposit in a sequence of 10 nm titanium and 250 nm gold on PVDF filter membrane (Durapore Membrane Filters, 5.00 μm SVPP, EMD MILLIPORE). The metal thickness was optimized in considering uniform electrode finger resistance and cost effectiveness. Membrane electrode was treated with oxygen plasma (Pico Diener Oxygen Plasma System) for 1 min before use followed by an activation process. Cyclic voltammetry method was used for this activation process, sweeping from -0.5 to 0.5 V at the rate of 200 mV/s for 20 cycles.

6.2.2 Cell preparation

Cells were cultured and retrieved before electrochemical testing. Hela (ATCC CCL-2) was cultured in DMEM media (Life Technologies, USA) with 10% fetal bovine serum (LifeTechnologies, Carlsbad, California, USA) in 5% CO_2 at 37 degree. The white blood cell (WBC) was retrieved from healthy human blood (Zen-Bio, Research Triangle Park, North Carolina, USA) by centrifuging. Both Hela cell and WBC were mixed with 1 mM ferricyanide/ferrocyanide in 10 mM PBS solution. The cell number was counted manually using hemocytometer under a microscope as the reference before testing.

6.2.3 Voltammetry method

In the electrochemical testing, an advanced potentiostat (CHI660D, CH Instrument) was used to achieve all the voltammetry methods including CV (cyclic voltammetry), OCV (open circuit voltage), Tafel plot, EIS (electrochemical impedance spectroscopy) and DPV (differential pulse voltammetry). Electrolyte used in these voltammetry methods was chosen to be ferricyanide/ferrocyanide at 1 mM in 10 mM PBS (pH = 7.35) solution. The concentration ratio of ferricyanide and ferrocyanide was controlled at 1 to stabilize potential according to Nernst equation and to be robust to possible evaporation. Electrolyte with too high concentration would make solvent easy to condense out in PVDF membrane especially at low liquid volume. The ratio between analytical ion ($[Fe(CN)_6]^{3-}/[Fe(CN)_6]^{4-}$) and electrolyte was fixed at 1:10 to make voltammetry method diffusion controlled because

of good screening effect of electrolyte [1]. CV was performed at a scan rate of 0.1 V/s between -0.5 V and +0.5 V. OCV was performed in a duration time of 20 minutes. Standard Ag/AgCl reference electrode (Fisher Scientific) was used when OCV was performed. Tafel plot measurement was executed in a scan rate of 0.1 mV/s while DPV method was executed with sweeping step at 4 mV. The pulse amplitude of DPV was set at 50 mV and the pulse width is 50 ms. EIS was performed at the voltage of -0.5 V at the frequency span from 10 Hz to 100 kHz.

6.2.4 Simulation

Finite element method (FEM) was applied to validate sensing principle, which was based on diffusion limited by bio-targets. Electroanalysis module in COMSOL Multiphysics 4.4 was used to explore the change by adding cells in diffusion path (no flux boundary condition). The electroanalytical Butler-Volmer equation was defined as electrode kinetics boundary condition; while the whole domain simulating the region around single finger on interdigitated electrode follow Ficks law of diffusion. Voltage step function and cyclic voltammetry were applied to electrode surface separately to study concentration distribution near electrode surface and current density due to diffusion coefficient variation. The default diffusion coefficient (D) of ferricyanide/ferrocyanide was estimated as 0.75×10^{-5} cm^2/s [149]; heterogeneous rate constant (k^0) is defined as 4.7×10^3 cm/s; transfer coefficient (α) is 0.23 and over-potential is set as -0.1 V. Parametric sweeping of D was studied from 0.1×10^{-5} cm^2/s to 1×10^{-5} cm^2/s at step size of 0.1×10^{-5} cm^2/s.

6.2.5 Portable system

Portable system design was addressed from electrical and mechanical side. In electrical system, Arduino UNO (ATmega328P) was integrated with external 12-bit DAC (MCP4725) and 16-bit ADC (MCP34265) as analog transmit/receive center. Two operational amplifiers (OPA2378) were built as simplified potentiostat with a first-order low-pass filter. Sensed signal received by Arduino was finally transmitted through Bluetooth module (HC-05 Blue-

tooth Serial Module) to smartphone. Maximum value in the DPV curve was used for data analysis.

Mechanical design in portable system was implemented by Solidworks 2012. The designed model was printed using a 3D printer (Ultimaker 2+, PLA material) at the resolution of 60 μm. PDMS was mixed with a curing agent at the weight ratio of 10:1. After degassing in vacuum desiccator for 30 minutes, PDMS was poured into a PLA model and put in an oven at 60 centigrade for 12 hours. All the PDMS components were finally assembled together with the membrane electrode and wires.

6.3 Results and discussion

6.3.1 Sensing system design and principle

The system diagram of our paper-based portable sensing platform was illustrated in Fig. 6.1a. Voltammetry signal was generated from portable potentiostat after WBC sample was trapped in the membrane (paper) electrode. Electrochemical sensing current during the voltammetry test was retrieved at the same time and transmitted through Bluetooth to smartphone. The smartphone App analyzed the collected data and gave out concentration value of WBC with internal calibration.

The electrochemical sensor head was designed as three gold electrodes which were patterned on a PVDF membrane by e-beam evaporation (see Fig. 6.1b). Working and counter electrodes were designed as interdigitated electrodes to make current flow evenly distributed. The reference electrode was designed closer to the working electrode to decrease uncompensated resistance. For the simplicity of the fabrication process [150], gold was used for all three electrodes due to its relevant low chemical reactivity and good conductivity. The feasibility of the gold reference electrode was validated by OCV (Open Circuit Voltage) measurement versus standard Ag/AgCl reference electrode. The measured coefficient of variation (CoV) of OCV value was only 0.45% (see Fig. 6.2). PVDF was chosen as porous membrane substrate because of its excellent antioxidation, superior thermal and chemical stability, outstanding physical adsorption as well as good mechanical property [151–153]. Higher conductivity (4.69×10^6 S/m) with thin film metal

deposition (250 nm) was found for PVDF membrane substrate compared with other materials like nitrocellulose membrane (open circuit). The average pore size of PVDF membrane was about 5.0 μm, smaller than the size of normal human white blood cell ($\sim$10 μm). The three-dimensional porous structure covered with a thin gold layer electrode can provide current amplification. The porous, rough and adsorptive PVDF membrane surface could provide an ideal platform for cell trapping as shown in Fig. 6.1c.

The electrochemical sensing principle within the membrane electrode was the diffusion blockage effect by the trapped cells which causes a reduced current response (see Fig. 6.1a). This principle could be elucidated by a simple EIS measurement in which an upward bending of diffusion impedance appeared at lower frequencies when more Hela cells were added to the membrane electrode (see Fig. 6.1d). This bending indicated more depletion of ions arriving at electrode (similar to the case with more negative over-potential) primarily owing to the cells capacitive blocking. Such capacitive blocking normally followed by typical Warburg-like part (with slope close to unity) was manifested by the diffusion impedance which was determined by frequency, concentration, diffusion coefficient and over-potential [154]. To further prove this concept, a simulation was made to show the concentration profile of target oxidant ions around the electrode surface after diffusion for the same duration time (see Figs. 6.3a and 6.3b). The cells trapped on or between electrodes blocked ion diffusion pathway and lowered the concentration of target ions reaching the electrode surface. Similar simulation was performed to show the current density decrease in CV due to the lowered concentration resulted from the cell blocked ion diffusion (see Figs. 6.3c and 6.3d). It was also noticeable that the change of charge transfer resistance was extremely small, mainly due to the numerous current path ways within porous membrane electrode (see Fig. 6.1d). According to Ficks second law, cells blockage effect could also be considered as a decrease in effective diffusion coefficient (D). It was illustrated in Juan Bisquert's work that the diffusion coefficient D was a function of diffusion response and diffusion impedance had a negative correlation with the diffusion coefficient [154–156].

The benefit of the porous membrane substrate was studied assuming that the cell trapping could be considered as a change in D. To study both the electrode kinetics and diffusion property of the membrane electrode, Tafel plot measurement was performed as shown in Fig. 6.1e. The ideal case (no

mass transfer effect) for current-overpotential relation can be written as:

$$i = i_0 \left[e^{-\alpha f \eta} - e^{(1-\alpha) f \eta} \right] \tag{6.1}$$

where i_0 is the exchange current; η is over-potential; $f = F/RT$ (R is gas constant; T is absolute temperature). The slope of the cathodic branch in this ideal case is $-\alpha F/2.3RT$ even for large over-potential. In reality, this slope will be flattened owing to the diffusion limit at very large over-potential indicated by the Tafel plot of a wire electrode in Fig. 6.1e. In comparison, the slope in the Tafel plot of membrane electrode was more flattened even at small over-potential. This phenomenon indicated a relatively strong diffusion limit in membrane electrodes, corresponding to a smaller background diffusion coefficient. The effect of background diffusion coefficient on the sensitivity of cell particle sensing was simulated (see Fig. 6.1f). A larger diffusion coefficient was observed to lead to higher current density but the current density slope at a lower diffusion coefficient was much larger, indicating a more sensitive change with the same amount of variation in the diffusion coefficient. Therefore, the membrane electrode with diffusion limit property was proved to be a potential more sensitive platform for particle sensing using diffusion block mechanism.

6.3.2 Membrane electrode characterization

Double-layer capacitance was investigated since it could be key to the voltammetry method selection [1]. The double-layer capacitance in our system was estimated according to sensed current and voltage scan rate by the cyclic voltammetry method. A comparison of the double-layer capacitance between wire and membrane electrode was made for electrolyte (10 mM PBS) only samples. The double-layer capacitance of membrane electrode (73.5 μF) was 14.7 times larger than that of wire electrode (5 μF) (see Fig. 6.4a). Such large double-layer capacitance introduced high interfering charging/discharging current to actual Faradaic current when the voltammetry method with high scan rate was applied. This drawback was confirmed by the CV method when quantifying Hela cells as shown in Fig. 6.4b. The sensitivity of the CV method was quite small and the linear correlation was relatively poor, therefore, it was not appropriate for the membrane electrode. On the other hand,

differential pulse voltammetry (DPV) is the proper method to effectively reduce non-Faradaic current (double-layer capacitor charging/discharging) owning to its current-difference mechanism and very slow scan rate [1], [157]. Current difference is taken before and after applying a voltage pulse in order to analyze the Faradaic current caused by the small amplitude of pulse. Given the short pulse width (50 ms) as the constant diffusion response time, the number of cell particles can be quantified due to different diffusion response on membrane electrode.

The current amplification by the membrane electrode was characterized with respect to a bulk gold wire electrode using cyclic voltammetry method (see Fig. 6.4c). The membrane electrode showed 12.5 times larger peak current than wire electrode. Although the planar surface area of membrane electrode ($\sim$25 mm^2) was larger than the gold wire electrode ($\sim$5 mm^2), it took only 10 μL of sample to generate such a high current compared to the minimum liquid needed (100 μL) for the gold wire electrode. The equivalent current density amplification ratio for membrane electrode was then about 25. The Tafel plot in Fig. 6.1e showed the membrane electrode had a two orders of magnitude higher exchange current than the wire electrode, which can be explained by the large electrode surface area in the following expression [1]:

$$i_0 = FAk^0(C_O^*)^{1-\alpha}(C_R^*)^{\alpha} \tag{6.2}$$

where α is the transfer coefficient; A is the electrode surface area; F is the Faraday constant; k^0 is standard heterogeneous rate constant; C_O^* is bulk oxidant concentration and C_R^* is bulk reductant concentration.

To ensure the membrane electrode can capture cells effectively as illustrated in Fig. 6.4d, a trapping test was made by dropping $\sim$60 k Hela cells in 10 μL solution on the membrane and comparing DPV currents before and after washing the electrode (see Fig. 6.5). Only 6% increase in peak current after washing was observed, indicating excellent surface trapping property and advantage in rapid cell captures.

Two techniques were used to overcome the hydrophobic property of PVDF and further improve cell trapping. First, PDMS as hydrophobic substrate was attached underneath the membrane electrode to ensure the liquid diffuse only within the membrane first (see Fig. 6.6a). Second, oxygen plasma (OP) treatment was also applied to change membrane into hydrophilic, which

helped raise the peak current by 35% (see Fig. 6.6b) [158]. The effect of mechanical flexibility of the membrane electrode was also studied and showed excellent stability (CoV=1.6%) in different deformation (see Fig. 6.7).

6.3.3 Cell counting on membrane electrode

The Hela cell, a human cervical cancer cell, was first used as the surrogate in counting experiments because of its similar size to human WBC. The DPV curve was measured for Hela cells in the amount of 6 to 600 k in total number in a constant volume of 10 μL (see Fig. 6.8a). The reduction current peak was observed near the formal reduction potential of ferricyanide. The minor potential shift could be due to the relative slow sweeping rate (20 mV/s). The peak current is inversely proportional to the increasing amount of cells, indicating more diffuse pathways were blocked by the cells. A highly linear calibration curve was made between peak current and cell number with a coefficient of determination $R^2 = 0.994$ (see Fig. 6.8b), a large linear dynamic range covering about 6 orders ($10^1 \sim 10^6$) of magnitude of cell numbers, and a limit of detection (LoD) at 60 cells. The DPV curves were analyzed using peak maximum instead of Gaussian peak height because it is more convenient to be realized in mobile application. The feasibility was validated using Gaussian peak height calibration (see Fig. 6.9) as comparison, which showed little effect on linearity and sensing range. The PVDF membrane pore size was investigated and optimized to achieve good linearity (see Fig. 6.10). For the case that pore size is larger than target size, the target's diffusion blockage effect will be much less which causes little interference.

After sensor verification using Hela cells, we isolated and counted WBC from the peripheral blood of health individuals. WBC was tested on membrane electrode in the number ranging between 10^1 and 10^6 cells in 10 μL liquid samples. Due to the diffusion blockage effect of WBC, the DPV measurements showed a similar inverse proportion between the cell numbers and peak currents (see Fig. 6.8c). The current measurement for cell numbers ranging from 1.5 k to 150 k (150 $\sim$ 15 k μL^{-1}) showed a good linearity ($R^2 =$ 0.938), exactly covering the WBC concentrations in a healthy person (4500 $\sim$ 11500 μL^{-1}) [118], leukopenia (decrease in number) and leukocytosis (increase in number) patients [159], [160]. The WBC testing results suggested

the potential for the sensor in clinical diagnosis. It is worthy to note that some interference may occur in real blood test like red blood cell (RBC) and other small molecules in serum. Since current sensing is based on physical adsorption and diffusion blockage mechanism, small molecules like glucose will cause very little interference (see Fig. 6.11) while RBC with similar size to WBC will make a significant difference. The microfluidic cell lysing unit could be integrated as pre-separation stage for real blood portable diagnosis system [22].

6.3.4 Portable white blood cell counting

Portable electronic potentiostat system for DPV sensing and Bluetooth communication was described in Fig. 6.12. The working electrode was stabilized by connecting together with a band-gap reference potential IC (2.5 V) to an Op-Amp. Voltage on the reference electrode will be keeping sweeping voltammetry. Pulse width (50 ms) and sampling time was accurately controlled using the timer function from micro-controller. A 12-bit DAC and 16-bit ADC component were used (see Fig. 6.12a) in order to achieve high current detection resolution as high as 200 nA demonstrated in Fig. 6.13. A 10 kΩ resistor with 1% tolerance was used to in the current to voltage conversion module in the circuit. Collected voltage values from this simplified potentiostat were transmitted through a wireless Bluetooth module to smartphone. The original DPV curve is plotted on the phone and the measured cell number is calculated according to built-in calibration equation (see Fig. 6.12b). The membrane electrode was assembled using PDMS as the hydrophobic supporting substrate and was electrically connected with three gold wires to the portable potentiostat. The configuration of the system assembly is shown in Figs. 6.12c and 6.12d.

The above portable electrochemical sensor was then applied to human WBC counting in the concentration range of 195 $\sim$ 25 k μL^{-1}. The DPV peak current change in this concentration range was linearly proportional to WBC concentration (see Fig. 6.14a). The LoD for our sensing system was 195 μL^{-1}, which was 30 times lower than normal concentration ($\sim$6000 μL^{-1}) in blood. The maximal peak current change ($\sim$60 μA) was 300 times of the current detection resolution (200 nA), which provided a very broad dynamic

range for cell concentration measurement. The minimal detectable change in cell concentration can be as low as 2.6%. Normalization by taking the ratio of sample current to background current was performed based on the background current (peak current from electrolyte) to cancel out the variation among different individual membrane electrodes. The normalization method led to a better fitting in calibration. The coefficient of determination (R^2) for regression fitting was found to be 0.994 throughout the entire concentration range (see Fig. 6.14b). The calibration equation could be expressed as:

$$Concentration = 10^{116.09 - current/21.44} \tag{6.3}$$

The detection range could be divided into two regions (low and high) which are calibrated separately to get more accurate fitting (see Figs. 6.14c and 6.14d). The CoV in the low concentration was 3.3% in average while the CoV in high concentration was 4.3%. The comparison of the measurement result from the portable detection system with commercial potentiostat showed good matching (see Fig. 6.15).

6.3.5 Blood sample accuracy test

To evaluate the accuracy of portable electrochemical system for WBC counting, 12 processed blood samples of 10 μL each from healthy personal with unknown WBC concentration were quantified by both gold standard manual counting method via microscopy and our portable sensing method respectively (see Fig. 6.16a). The WBC concentration was from 200 μL^{-1} to 15000 μL^{-1}, covering majority clinical relevant disease from leukopenia and leukocytosis. The calibration curve used for quantification was derived from Fig. 6.14. The overall CoV of repeatability testing was 8.8%. The CoV for WBC counting accuracy at low concentration (<2000 μL^{-1}) was as low as 10% while that in the high concentration (>8000 μL^{-1}) was 15% as shown in Fig. 6.16. Most data points were distributed around the $y = x$ line with a coefficient of determination (R^2) at 0.993. The high accuracy and precision of our sensor especially in the low WBC concentration are crucial for applications such as monitoring therapy effects for cancer or immune-deficiency patients [123], [124]. Although slightly lower in very high WBC concentration, the counting accuracy of our sensor is more than sufficient

for quick diagnosis of bacterial infection [119], [120] in which case the WBC concentration increases over two folds. In addition, the less-than-one-minute detection time and broad range WBC counting of our portable paper sensor are critical for rapid diagnostics especially in emergency care.

6.4 Conclusion

Due to the significance of WBC counting in clinical diagnosis and the highly demand in rapid, low-cost solution for point-of-care WBC test, we demonstrated a novel platform using smartphone-based electrochemical method to achieve fast label-free WBC counting on microfabricated membrane electrode. The sensing principle was based on the diffusion blockage by the cells trapped on membrane electrodes and the consequent electrochemical signal change as the function of the cell concentration. The membrane microelectrode showed advantages in current amplification, excellent surface trapping, large double-layer capacitance, hydrophilicity and flexibility. By creating a mobile differential pulse voltammeter, the peak currents from tests on WBC at different concentrations were retrieved and transmitted to smartphone through Bluetooth protocol. The across-four-orders-of-magnitude dynamic range for our WBC sensor was able to cover healthy, leukopenia and leukocytosis conditions with excellent accuracy and precision. The current system has no cell separation unit which will be integrated in the future for direct whole blood testing. Overall, our mobile WBC counting work showed its potential in future point-of-care applications like inflammation disease diagnosis at home.

6.5 Figures

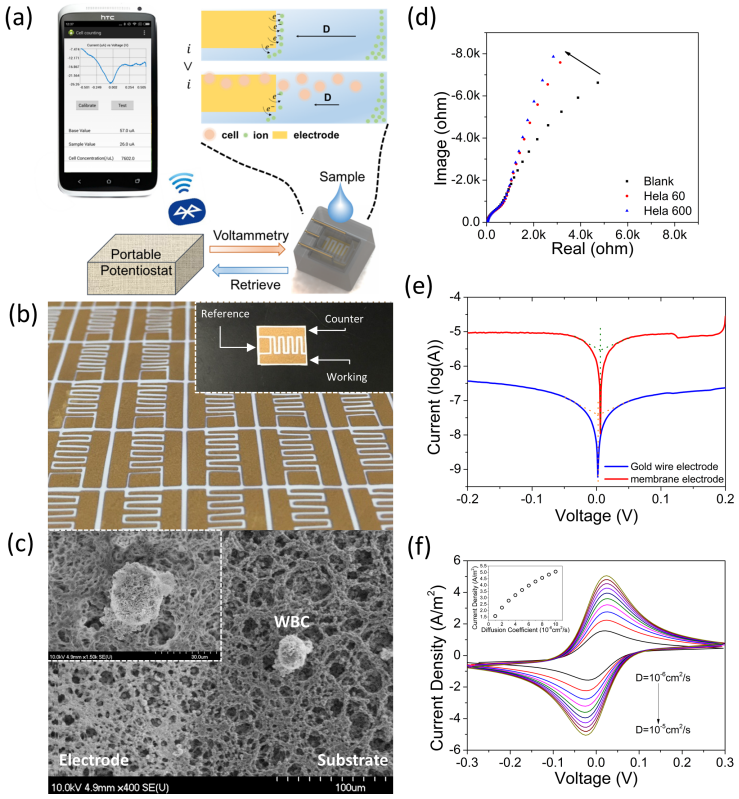

Figure 6.1: Cell counting sensor design and principle. (a) System diagram and electrochemical principle for WBC count. D is diffusion coefficient. i is the electrochemical current. (b) Gold three-electrodes on PVDF (polyvinylidene fluoride) membrane paper. (c) Scanning electron microscopy image of trapped WBC (white blood cell) on PVDF and microporous structure of PVDF membrane. (d) Nyquist plot of electrochemical impedance spectroscopy (EIS) showing the diffusion impedance upward bending by adding more Hela cells on the membrane electrode. The over-potential in EIS is -0.5 V with frequency sweeping from 10 Hz to 100 kHz. (e) Tafel plot of the membrane electrode and wire electrode in 1 mM $[Fe(CN)_6]^{3-}/[Fe(CN)_6]^{4-}$ and 10 mM PBS at the scan rate of 0.1 mV/s. (f) Simulation of cyclic voltammetry method at different diffusion coefficient in the environment of 1 mM $[Fe(CN)_6]^{3-}/[Fe(CN)_6]^{4-}$ and the inset is the peak current density change with diffusion coefficient.

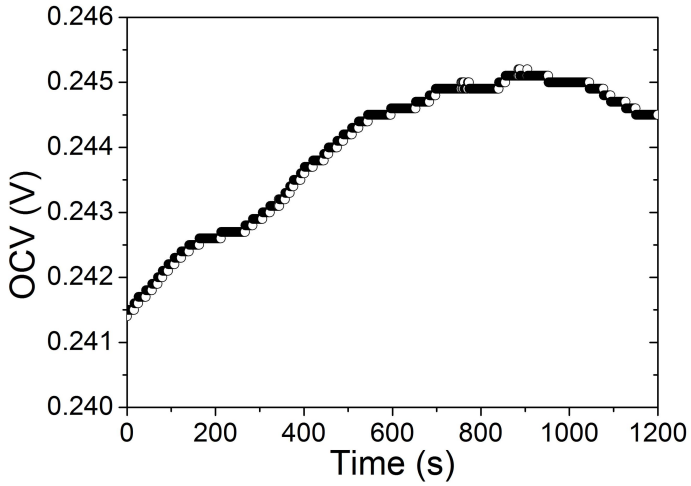

Figure 6.2: Open circuit voltage of Au membrane electrode in 1 mM $[Fe(CN)_6]^{3-}/[Fe(CN)_6]^{4-}$ and 10 mM PBS versus standard Ag/AgCl reference electrode. The average value is 0.244 V with a standard deviation of 1.1 mV.

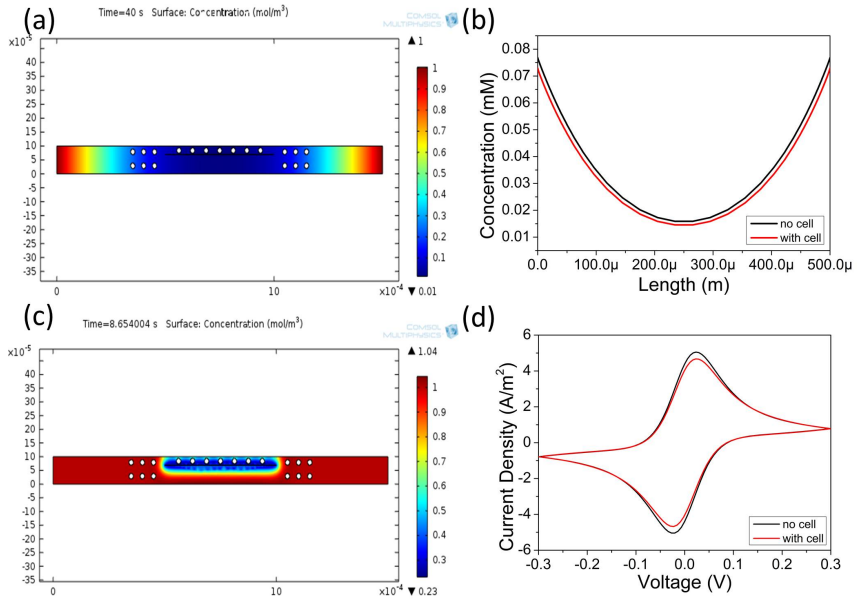

Figure 6.3: Simulation of cell blocking around electrode. (a) Concentration gradient within membrane electrode with trapped cells after step potential on electrode was applied. Initial concentration of target ion (oxidant) within the domain is zero. Left and right boundary was set as bulk concentration. (b) Concentration profile across electrode surface for the case of without and with cells trapped. (c) Concentration gradient within membrane electrode with trapped cells when surface target ions (oxidant) were depleted (reduced). (d) CV curve for the case of without and with cells trapped.

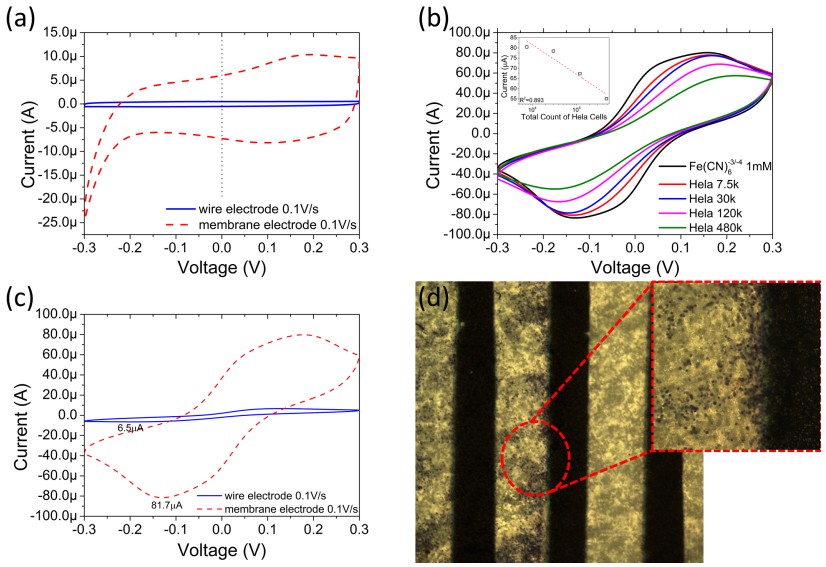

Figure 6.4: Membrane electrode characterization. (a) Cyclic voltammetry test on wire and membrane electrode in electrolyte only (10 mM PBS) at the scan rate of 0.1 V/s. Double-layer capacitance was estimated from current value at voltage 0. (b) Cyclic voltammetry for loading Hela cells at the amount of 7.5 k, 30 k, 120 k and 480 k with 1 mM $[Fe(CN)_6]^{3-}/[Fe(CN)_6]^{4-}$ and 10 mM PBS in a volume of 10 μL. The inset shows the peak current calibration with total count of Hela cells. (c) Comparison of CV curves at the scan rate of 0.1 V/s in 1 mM $[Fe(CN)_6]^{3-}/[Fe(CN)_6]^{4-}$ and 10 mM PBS. (d) Microscopy image of trapped dyed Hela cells on membrane electrode.

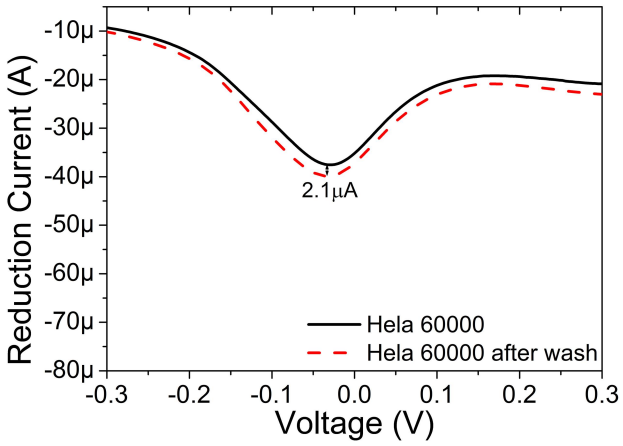

Figure 6.5: Verification of surface trapping. DPV test of 60 k Hela cells on membrane electrode before and after washing. The washing process was performed using distilled water to remove redundant ions. After drying with nitrogen gas, same volume of electrolyte solution (1 mM $[Fe(CN)_6]^{3-}/[Fe(CN)_6]^{4-}$ in 10 mM PBS) was added on membrane electrode and the second DPV test was performed.

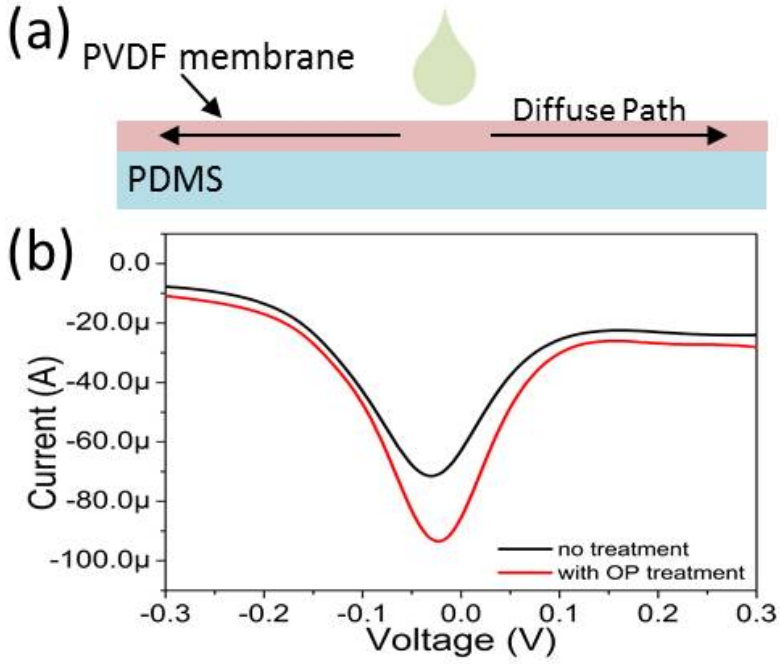

Figure 6.6: Hydrophilicity improvement of the PVDF electrodes. (a) Illustration of target liquid diffuse path with PDMS substrate. The hydrophobic property of PDMS ensures diffusion within membrane first. (b) DPV test for background (1 mM $[Fe(CN)_6]^{3-}/[Fe(CN)_6]^{4-}$ and 10 mM PBS) with and without oxygen plasma treatment at the volume of 15 μL.

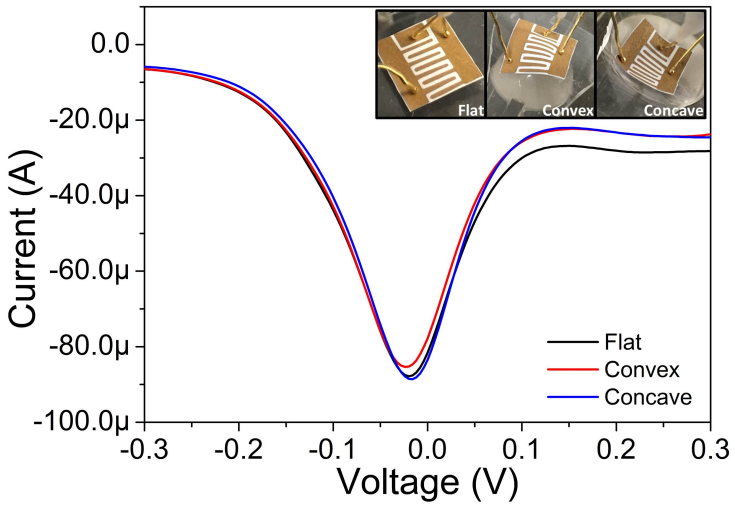

Figure 6.7: Flexibility performance. DPV measurement results with membrane electrode placed on flat, convex and concave surface separately as the flexibility test on the PVDF membrane electrodes.

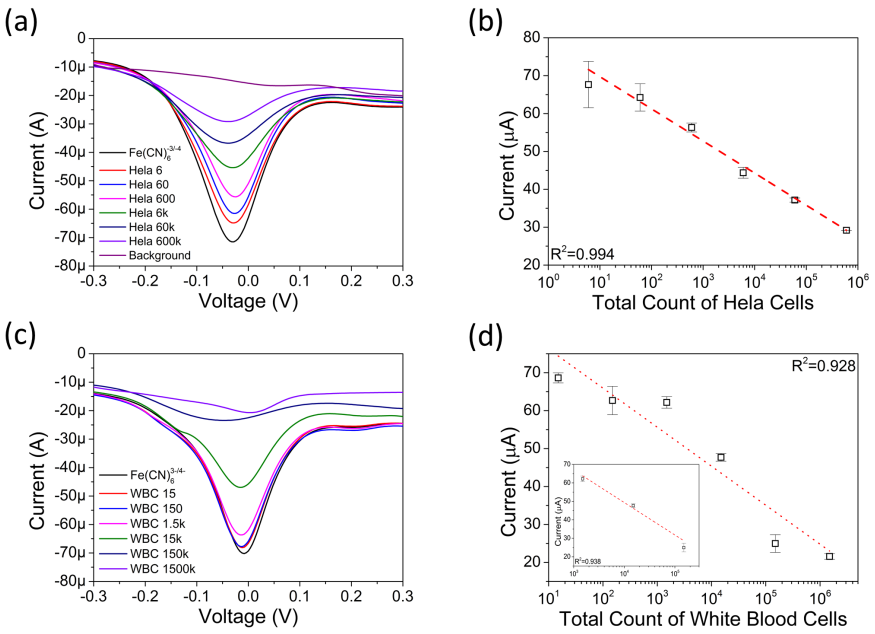

Figure 6.8: Cell counting and calibration on membrane electrode using commercial potentiostat. (a) DPV reduction peak as the function of Hela cell numbers at the amount of 6 to 600 k on membrane electrode. Background is just 10 mM PBS. (b) Calibration curve of peak current as the function of Hela cell number based on three replicates. (c) DPV reduction peak after capturing white blood cells (WBC) at the amount of 15 to 1500 k on membrane electrode. (d) DPV reduction peak as the function of WBC numbers at the amount of 6 to 600 k on membrane electrode (three replicates). The inset shows the peak current as the function of the WBC number in the range of 10^3 to 10^5. The DPV experiment was performed with incremental amplitude at 4 mV and a period of 0.2 s, as well as the pulse height at 50 mV with 50 ms pulse width. All the calibration was made with the buffer of 1 mM $[Fe(CN)_6]^{3-}/[Fe(CN)_6]^{4-}$ in 10 mM PBS.

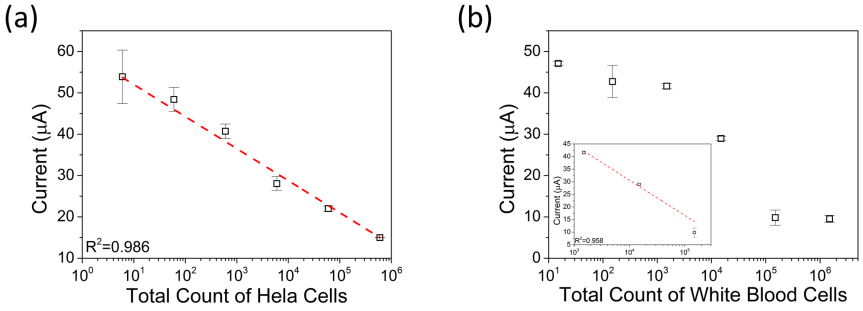

Figure 6.9: Calibration of Hela and WBC using Gaussian peak detection method for DPV curve.

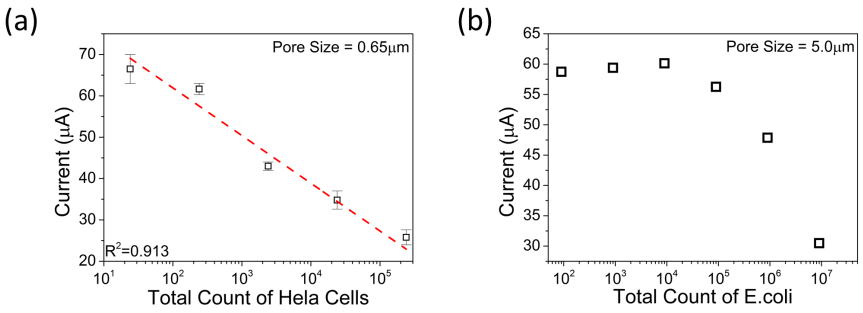

Figure 6.10: PVDF membrane pore size and target size effect. (a) Hela cell calibration on membrane electrode with smaller size (0.65 μm). The pore size here is much smaller than the target size. The linearity at this pore size was worse than the case with pore size of 5.0 μm. (b) *E. coli* calibration on membrane electrode with the same size in main context (5.0 μm). The pore size here is larger than the target size. Diffusion blockage effect was very little at low concentration.

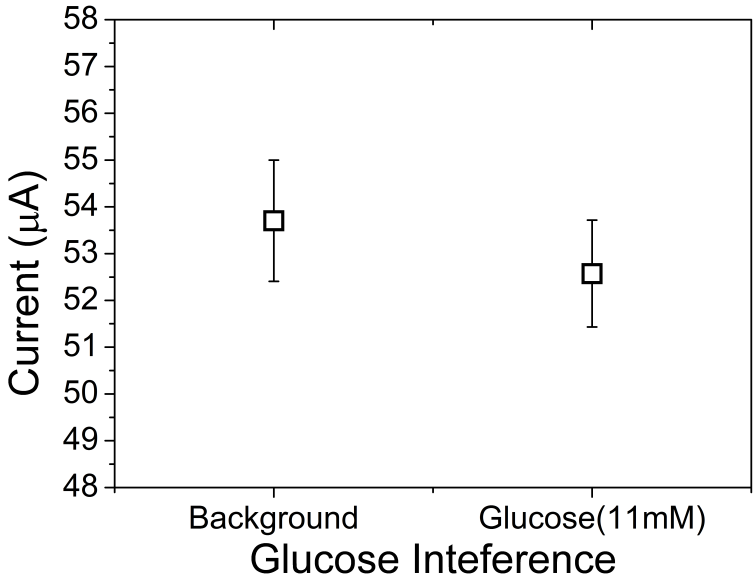

Figure 6.11: Glucose interference on membrane electrode with DPV method. The current measured from background (1 mM $[Fe(CN)_6]^{3-}/[Fe(CN)_6]^{4-}$ and 10 mM PBS) is quite close to the current measured from glucose. The concentration of glucose for testing is 11 mM, which is twice of the normal concentration in human blood.

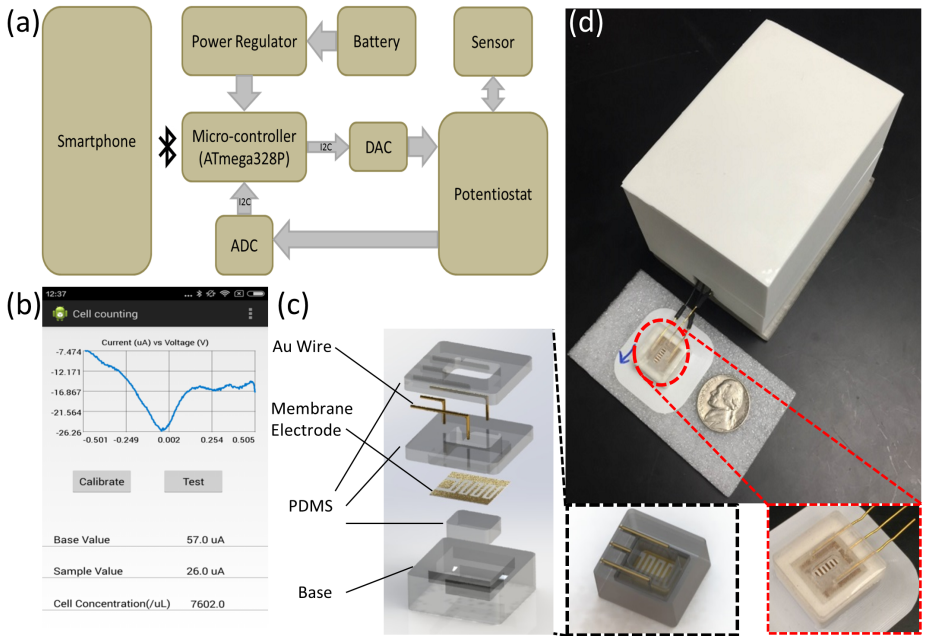

Figure 6.12: Smartphone-based electrochemical cell counting platform design. (a) Block diagram of the sensor electronics system. (b) Android App interface with received electrochemical sensing data through Bluetooth protocol plotted on smartphone screen. (c) Assembly and explosive view of the sensor package. (d) Whole package view with sensor assembly and electronic system.

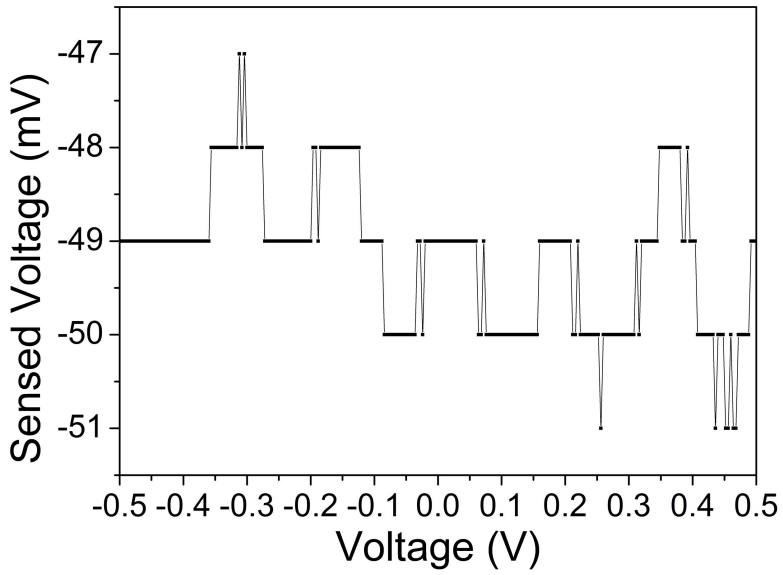

Figure 6.13: Electrochemical sensor electronics resolution. The deviation is 200 nA in average.

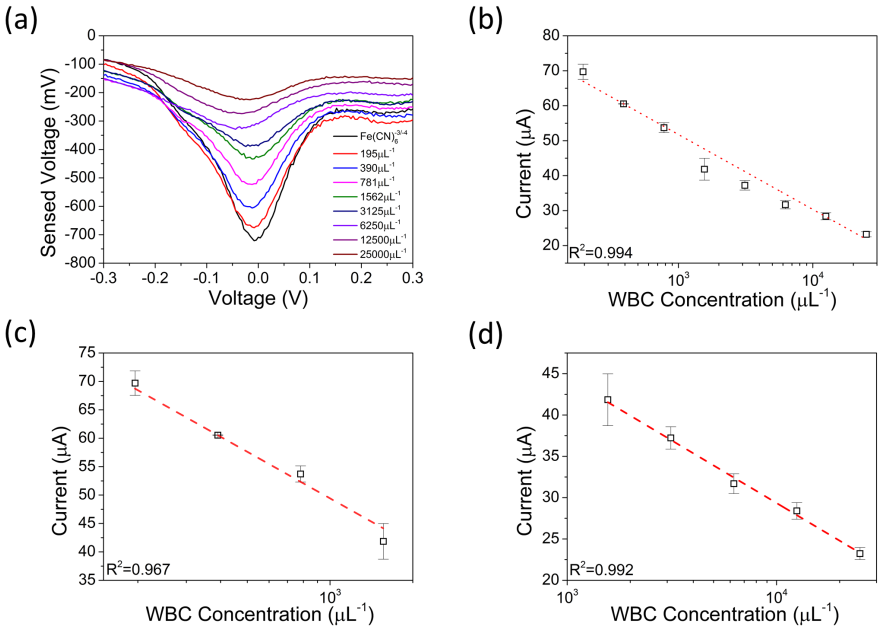

Figure 6.14: WBC counting and calibration using smartphone electrochemical platform with PVDF membrane electrodes. (a) DPV reduction current peak corresponding to white blood cells at different concentrations in the volume of 10 μL. (b) Converted reduction peak current as the function of WBC concentration calibration with R^2=0.994 (3 replicates). (c) Calibration curve for WBC concentration at low concentration range. (d) Calibration curve for WBC concentration at high concentration range.

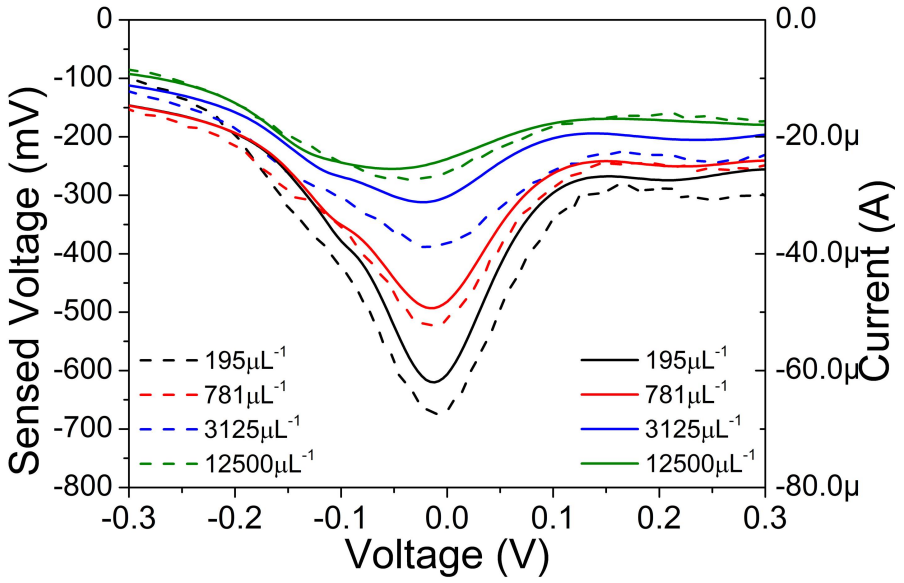

Figure 6.15: Comparison between the portable DPV system and commercial potentiostat. Dashed lines are the results for portable system while solid lines are the results for potentiostat.

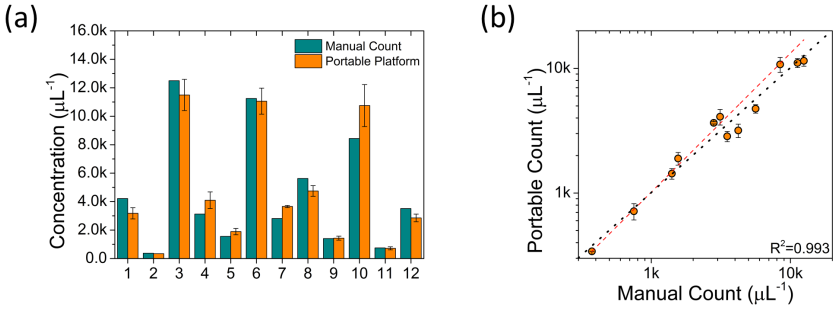

Figure 6.16: Correlation study between the portable electrochemical cell counting method and manual counting. (a) Measurement of WBC with different concentration by manual count and portable electrochemical method respectively. (b) Comparison between portable electrochemical method and manual count method. The red dashed line is the linear regression fitting curve with $R^2 = 0.993$. The black dot line is the y=x line representing the perfect matching line.

CHAPTER 7

OPTIMIZATION OF PAPER-BASED ELECTROCHEMICAL SENSOR WITH FILTERING FUNCTION

7.1 Introduction

The WBC counting application was achieved in Chapter 6 using a paper-based electrochemical sensor. There are several properties of paper electrochemical electrodes described in Chapter 6: large double-layer capacitance, high exchange current density and low effective diffusion coefficient. The sensing principle is based on the diffusion limit of such electrodes. The advantage of a low diffusion coefficient was further explored in this chapter using numerical simulation to simulate the DPV response of diffusion block electrochemical system. In addition, the optimization of paper-based electrochemical sensor was studied by researching the effect of paper pore size and bio-target size. The interference from small molecules like glucose and protein was also investigated. Lastly, the filtering function will be discussed and a new way to make paper-based micro-fluid channels will be introduced. These explorations will extend the use of the paper-based electrochemical sensor to the application of separation and multi-target testing.

7.2 Materials and methods

7.2.1 Paper-based micro-fluid channel

A mode was first designed with Solidworks 2012 and printed using 3D printer (Ultimaker 2+, PLA material). PDMS was prepared with curing agent at the weight ratio of 10:1. The prepared liquid PDMS was poured into the printed mode, left in oven at 60 degrees for 12 hours. About 100 μL UV-curable polymer (NOA-65) was evenly spread on a piece of glass, and the prepared

PDMS mode was used to stamp on the UV-curable polymer. Then the stamped PDMS transferred the UV-curable polymer to the PVDF electrode at the specific position. After exposure to UV for only one minute, the UV-curable polymer was solidified and the paper micro-fluid channel was created.

7.2.2 COMSOL simulation

Electroanalysis module in COMSOL Multiphysics 4.4 was used to explore the effect of low diffusion coefficient and diffusion block effect. The electroanalytical Butler-Volmer equation was defined as the electrode kinetics boundary condition; while the whole domain simulating the region around a single finger on interdigitated electrode follow Ficks law of diffusion. The diffusion blockage effect of cells was simulated as circle domains with very low diffusion coefficient (0.75×10^{-6} cm^2/s). The DPV voltage form was applied to electrodes with a pulse width as 100 ms and incremental rate as 0.05 V per second. The default diffusion coefficient (D) of ferricyanide/ferrocyanide was estimated as 0.75×10^{-5} cm^2/s; heterogeneous rate constant (k^0) is defined as 4.7×10^3 cm/s; transfer coefficient (α) is 0.23. Both the current density through electrode and the concentration profile around the electrode were exported.

7.3 Results and discussion

7.3.1 Diffusion coefficient effect

It was shown in Chapter 6 that the diffusion coefficient for current paper-based electrochemical sensor is low, which was verified to have higher sensitivity by simulation using cyclic voltammetry method. Since the actual voltammetry method we used in the experiment is DPV, further validation was performed. The voltage applied on the working electrode was shown in Fig 7.1a. The duration of the pulse is 100 ms while one period is 1 s. The current density was monitored for both the case with and without cell (see Fig. 7.1b). Since the DPV method takes the difference value between the after-pulse current and the before-pulse current, 50 ms was chosen as the

sampling time (see Fig. 7.1c). The sensitivity could be calculated as:

$$Sensitivity = \frac{I_{diff\ without\ cell} - I_{diff\ with\ cell}}{I_{diff\ without\ cell}}\% \tag{7.1}$$

The cases with two diffusion coefficients were compared in Fig. 7.1d and the sensitivity from the lower diffusion coefficient environment showed higher value than the other, which indicated the low diffusion coefficient is an advantage to this PVDF electrochemical sensor. When the simulation was performed, the diffusion block mechanism was simulated as circle domains with a very low diffusion coefficient. This diffusion limitation effect can be observed from Fig. 7.1e and Fig. 7.1f, which shows the concentration distribution at the same time.

7.3.2 Paper pore size and target size effect

Hela quantification with different pore size PVDF membrane was demonstrated in Chapter 6 and the data from 5.0 μm paper showed better linearity. This interested us to make a discussion about the effect from pore size and target size. In order to get more evidence, we implemented the experiment for bacteria quantification with both 5.0 μm and 0.65 μm pore size (see Fig. 7.2). The data from 0.65 μm paper shows better linearity and larger covariance than that from 5.0 μm paper. While 5.0 μm showed better performance for Hela quantification, we can make tempt conclusion that better performance can be achieved when pore size is smaller than target size in the same order. This discussion will provide useful guidance for the future design of our paper electrode.

7.3.3 Small molecule interference

Before we are able to implement filtering function use paper-based electrochemical sensor, we need to analyze the interference from small molecules. Since the filtering plus sensing stage is based on the physical trapping of large bio-targets like cells or bacteria, small molecules were expected to flow through the PVDF membrane electrode for sensing in the next stage. Two kinds of molecule targets were selected for verification test: glucose and BSA.

The concentration of glucose was made at 11 mM, which is twice the people's normal concentration (5.5 mM). A comparison was made between such glucose and background electrolyte using DPV method (see Fig. 7.3a). There was little variation between background and glucose, which means the glucose molecules successfully flow through the membrane electrode and were not physically absorbed at the porous electrode surface (see Fig. 7.3b). The similar experiment was implemented with BSA. Since PVDF was widely used for the Western Blot experiment, PVDF is able to largely adsorb proteins especially immersed in methanol. So the change of BSA concentration caused the current peak change as expected (see Fig. 7.3c) and a linear correlation could be formed for BSA in high concentration (see Fig. 7.3d). So BSA can be a strong interference for filtering function and will alter results a lot for cell/bacteria quantification. A separate stage for protein sensing is necessary if we would like to use PVDF membrane as electrode substrate.

Figure 7.4 shows the results from EIS testing on BSA quantification.

7.3.4 Filtering function for separation

Filtering function will be implemented for separating small molecules from large bio-target like cell or bacteria. The sensing of cell or bacteria could be based on our previous work while the detection of small molecules could be achieved using the colorimetric or electrochemical method. The key for filtering function and small molecule detection is the paper-based micro-fluid channel fabrication technique. The closed-form micro-fluid channel around electrode will ensure the filtering process just through electrode and the channel in post-filtering stage will guide the fluid to detection point. Here we introduced a novel way to make such paper micro-fluid channels (see Fig. 7.5). The channel material is UV polymer, which is hydrophobic to PDMS and with high viscosity. With exposure to UV light, such polymer will be solidified within 1 minute. Since this material is hydrophobic, it can be easily peeled off from PDMS and be used as micro-fluid channel to guide fluid flow. An advantage of this technique is it keeps the conductivity of electrode on PVDF membrane.

With the above paper micro-fluid fabrication technique, we are able to implement filtering function for separation and multi-target testing.

7.4 Conclusion

In summary, the optimization parameters were discussed in this chapter, which include the paper pore size, bio-target size and small molecule interference. The investigation indicated that the best performance could be achieved when the bio-target size is larger than the paper pore size, but in the same order. The interference analysis demonstrated that there is little interference from non-absorptive molecules like glucose and other ions, while the interference from protein needs to be considered seriously since it can be highly adsorbed by PVDF membrane. For the implementation of filtering function for multi-target testing, a novel fabrication method to create a paper micro-fluid channel was illustrated. This method paves the way for the future filtering function and multi-target separation.

7.5 Figures

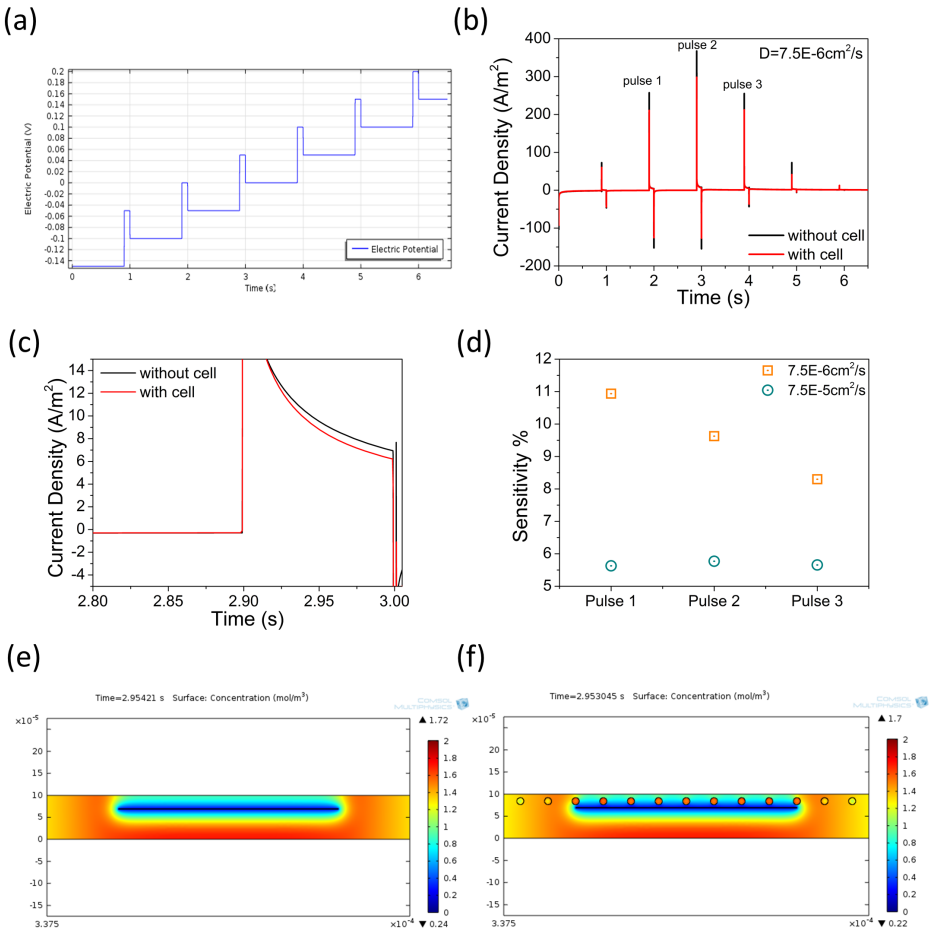

Figure 7.1: Simulation of cell blocking around electrode with DPV. (a) Electrode potential applied for DPV. (b) Current density change with time for the case without and with cells. Diffusion coefficient in the plot is 7.5×10^{-6} cm^2/s. (c) Zoom-in image of the pulse 2 current density in (b). (d) Comparison of sensitivity for lower and higher diffusion coefficient. (e) Concentration profile for the case without cell at time 2.95 s. (f) Concentration profile for the case with cell at time 2.95 s.

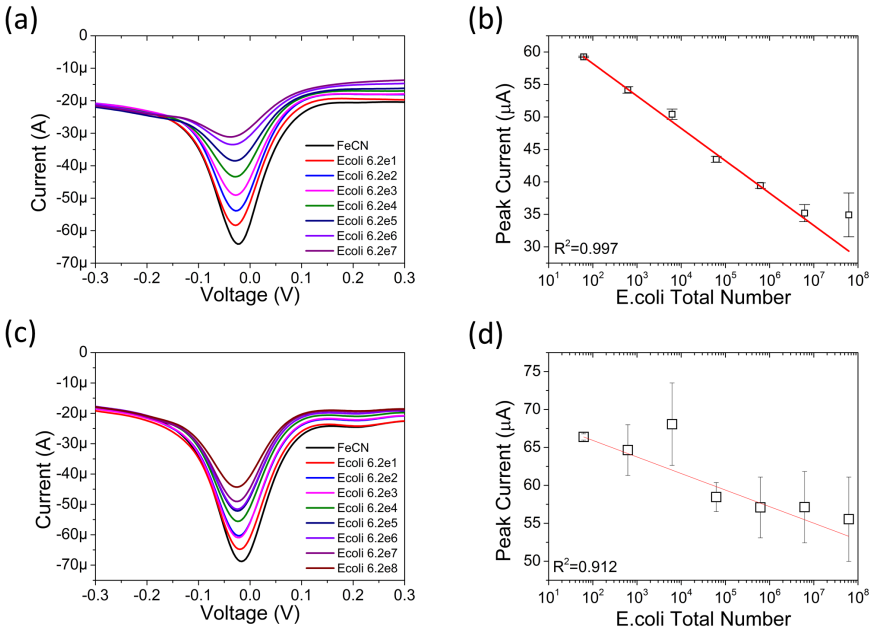

Figure 7.2: *E. coli* quantification on PVDF with pore size of 5.0 μm and 0.65 μm. (a) DPV curve for *E. coli* on 0.65 μm PVDF paper. (b) Calibration for *E. coli* quantification on 0.65 μm PVDF paper. (c) DPV curve for *E. coli* on 5.0 μm PVDF paper. (d) Calibration for *E. coli* quantification on 5.0 μm PVDF paper.

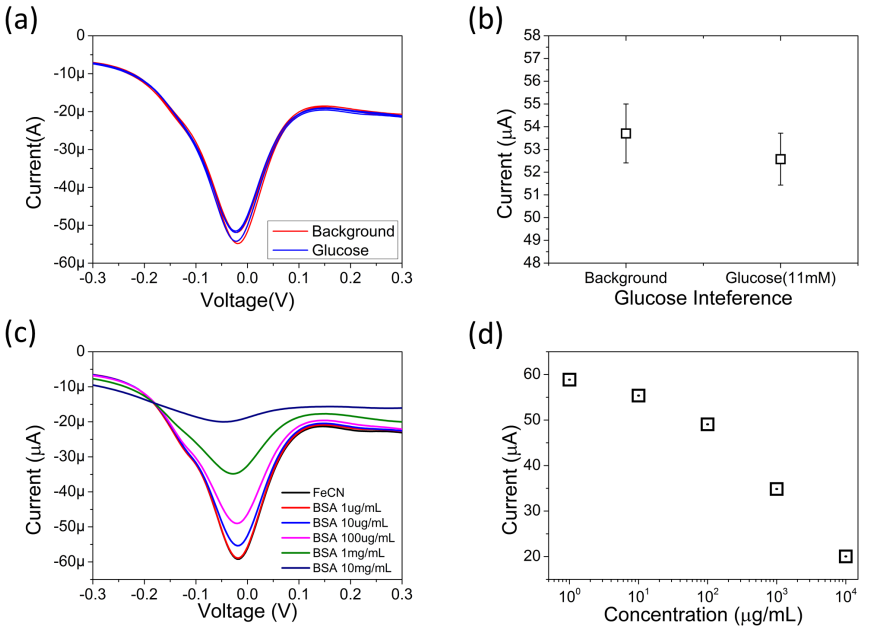

Figure 7.3: Small molecule interference analysis. (a) DPV curve from glucose and background electrolyte. (b) Comparison between glucose and background current. (c) DPV curve from BSA at different concentration. (d) Calibration for BSA concentration.

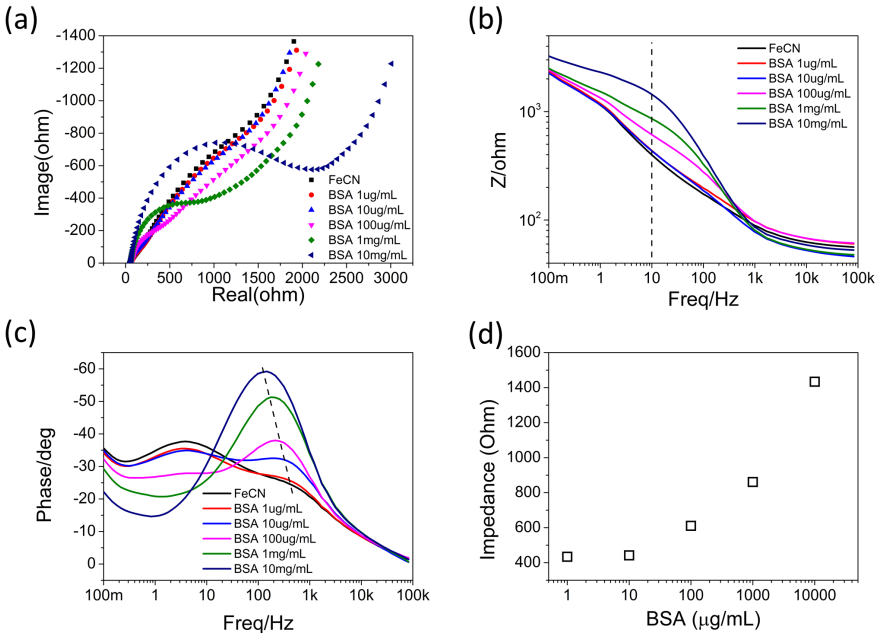

Figure 7.4: EIS analysis for BSA quantification on PVDF membrane electrode. (a) Nyquist plot of BSA EIS testing. (b) Magnitude of impedance from BSA EIS test. (c) Phase of impedance from BSA EIS test. (d) Calibration for BSA at frequency of 10 Hz.

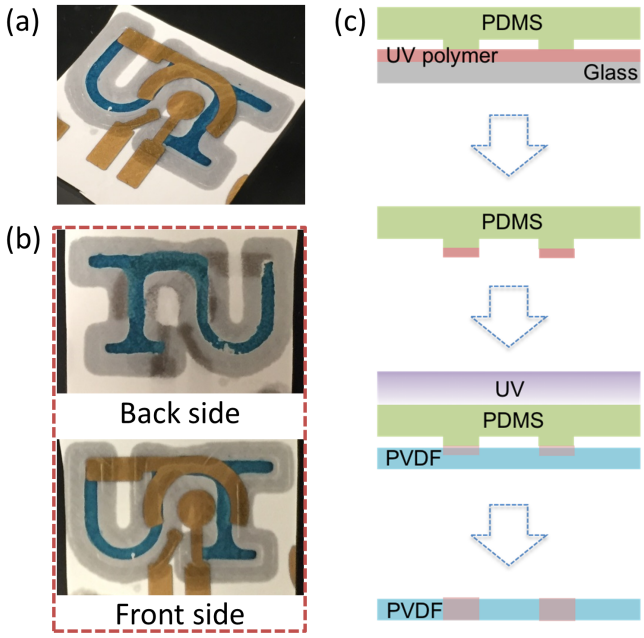

Figure 7.5: The way of using UV polymer to create paper micro-fluid channel. (a) 3D view of paper micro-fluid channel across electrode. (b) Back side and front side views of paper micro-fluid channel. (c) Fabrication process for such paper micro-fluid channel.

REFERENCES

[1] A. J. Bard, L. R. Faulkner, J. Leddy and C. G. Zoski, *Electrochemical Methods: Fundamentals and Applications*. Wiley New York, 1980, vol. 2.

[2] R. S. Nicholson and I. Shain, "Theory of stationary electrode polarography. Single scan and cyclic methods applied to reversible, irreversible, and kinetic systems," *Anal. Chem.*, vol. 36, no. 4, pp. 706–723, 1964.

[3] J. Heinze, "Cyclic voltammetry – "electrochemical spectroscopy". New analytical methods (25)," *Angew. Chem. Int. Ed. Engl.*, vol. 23, no. 11, pp. 831–847, 1984.

[4] E. Barsoukov and J. R. Macdonald, *Impedance Spectroscopy: Theory, Experiment, and Applications*. John Wiley & Sons, 2005.

[5] M. E. Stewart, C. R. Anderton, L. B. Thompson, J. Maria, S. K. Gray, J. A. Rogers and R. G. Nuzzo, "Nanostructured plasmonic sensors," *Chem. Rev.*, vol. 108, no. 2, pp. 494–521, 2008.

[6] A. V. Zayats and I. I. Smolyaninov, "Near-field photonics: Surface plasmon polaritons and localized surface plasmons," *J. Opt. A Pure Appl. Opt.*, vol. 5, no. 4, p. S16, 2003.

[7] S. A. Maier, *Plasmonics: Fundamentals and Applications*. Springer Science & Business Media, 2007.

[8] M. R. Gartia, A. Hsiao, A. Pokhriyal, S. Seo, G. Kulsharova, B. T. Cunningham, T. C. Bond and G. L. Liu, "Colorimetric plasmon resonance imaging using nano Lycurgus cup arrays," *Adv. Opt. Mater.*, vol. 1, no. 1, pp. 68–76, 2013.

[9] Y. Shen, J. Zhou, T. Liu, Y. Tao, R. Jiang, M. Liu, G. Xiao, J. Zhu, Z.-K. Zhou, X. Wang et al., "Plasmonic gold mushroom arrays with refractive index sensing figures of merit approaching the theoretical limit," *Nat. Commun.*, vol. 4, 2013.

[10] K. Lodewijks, W. Van Roy, G. Borghs, L. Lagae and P. Van Dorpe, "Boosting the figure-of-merit of LSPR-based refractive index sensing by phase-sensitive measurements," *Nano Lett.*, vol. 12, no. 3, pp. 1655–1659, 2012.

[11] J. M. Bingham, W. P. Hall and R. P. Van Duyne, "Exploring the unique characteristics of LSPR biosensing," in *Nanoplasmonic Sensors*. Springer, 2012, pp. 29–58.

[12] D. Maystre, "Theory of woods anomalies," in *Plasmonics*. Springer, 2012, pp. 39–83.

[13] Q. Wei, R. Nagi, K. Sadeghi, S. Feng, E. Yan, S. J. Ki, R. Caire, D. Tseng and A. Ozcan, "Detection and spatial mapping of mercury contamination in water samples using a smart-phone," *ACS Nano*, vol. 8, no. 2, pp. 1121–1129, 2014.

[14] S. K. Ludwig, H. Zhu, S. Phillips, A. Shiledar, S. Feng, D. Tseng, L. A. van Ginkel, M. W. Nielen and A. Ozcan, "Cellphone-based detection platform for rbST biomarker analysis in milk extracts using a microsphere fluorescence immunoassay," *Anal. Bioanal. Chem.*, vol. 406, no. 27, pp. 6857–6866, 2014.

[15] Q. Wei, W. Luo, S. Chiang, T. Kappel, C. Mejia, D. Tseng, R. Y. L. Chan, E. Yan, H. Qi, F. Shabbir et al., "Imaging and sizing of single DNA molecules on a mobile phone," *ACS Nano*, vol. 8, no. 12, pp. 12 725–12 733, 2014.

[16] H. C. Koydemir, Z. Gorocs, D. Tseng, B. Cortazar, S. Feng, R. Y. L. Chan, J. Burbano, E. McLeod and A. Ozcan, "Rapid imaging, detection and quantification of Giardia lamblia cysts using mobile-phone based fluorescent microscopy and machine learning," *Lab Chip*, vol. 15, no. 5, pp. 1284–1293, 2015.

[17] D. Gallegos, K. D. Long, H. Yu, P. P. Clark, Y. Lin, S. George, P. Nath and B. T. Cunningham, "Label-free biodetection using a smartphone," *Lab Chip*, vol. 13, no. 11, pp. 2124–2132, 2013.

[18] L. Shen, J. A. Hagen and I. Papautsky, "Point-of-care colorimetric detection with a smartphone," *Lab Chip*, vol. 12, no. 21, pp. 4240–4243, 2012.

[19] P. B. Lillehoj, M.-C. Huang, N. Truong and C.-M. Ho, "Rapid electrochemical detection on a mobile phone," *Lab Chip*, vol. 13, no. 15, pp. 2950–2955, 2013.

[20] A. Nemiroski, D. C. Christodouleas, J. W. Hennek, A. A. Kumar, E. J. Maxwell, M. T. Fernández-Abedul, and G. M. Whitesides, "Universal mobile electrochemical detector designed for use in resource-limited applications," *Proc. Natl. Acad. Sci.*, vol. 111, no. 33, pp. 11 984–11 989, 2014.

[21] D. Zhang, J. Jiang, J. Chen, Q. Zhang, Y. Lu, Y. Yao, S. Li, G. L. Liu and Q. Liu, "Smartphone-based portable biosensing system using impedance measurement with printed electrodes for 2, 4, 6-trinitrotoluene (TNT) detection," *Biosens. Bioelectron.*, vol. 70, pp. 81–88, 2015.

[22] U. Hassan and R. Bashir, "Coincidence detection of heterogeneous cell populations from whole blood with coplanar electrodes in a microfluidic impedance cytometer," *Lab Chip*, vol. 14, no. 22, pp. 4370–4381, 2014.

[23] D. Holmes, D. Pettigrew, C. H. Reccius, J. D. Gwyer, C. van Berkel, J. Holloway, D. E. Davies and H. Morgan, "Leukocyte analysis and differentiation using high speed microfluidic single cell impedance cytometry," *Lab Chip*, vol. 9, no. 20, pp. 2881–2889, 2009.

[24] E. J. Maxwell, A. D. Mazzeo and G. M. Whitesides, "Paper-based electroanalytical devices for accessible diagnostic testing," *MRS Bull.*, vol. 38, no. 04, pp. 309–314, 2013.

[25] J. Hu, S. Wang, L. Wang, F. Li, B. Pingguan-Murphy, T. J. Lu and F. Xu, "Advances in paper-based point-of-care diagnostics," *Biosens. Bioelectron.*, vol. 54, pp. 585–597, 2014.

[26] A. W. Martinez, S. T. Phillips, M. J. Butte and G. M. Whitesides, "Patterned paper as a platform for inexpensive, low-volume, portable bioassays," *Angew. Chem. Int. Ed. Engl.*, vol. 46, no. 8, pp. 1318–1320, 2007.

[27] A. W. Martinez, S. T. Phillips, Z. Nie, C.-M. Cheng, E. Carrilho, B. J. Wiley and G. M. Whitesides, "Programmable diagnostic devices made from paper and tape," *Lab Chip*, vol. 10, no. 19, pp. 2499–2504, 2010.

[28] A. W. Martinez, S. T. Phillips and G. M. Whitesides, "Three-dimensional microfluidic devices fabricated in layered paper and tape," *Proc. Natl. Acad. Sci. U. S. A.*, vol. 105, no. 50, pp. 19 606–19 611, Dec 2008.

[29] Z. Nie, C. A. Nijhuis, J. Gong, X. Chen, A. Kumachev, A. W. Martinez, M. Narovlyansky and G. M. Whitesides, "Electrochemical sensing in paper-based microfluidic devices," *Lab Chip*, vol. 10, no. 4, pp. 477–483, 2010.

[30] Z. Nie, F. Deiss, X. Liu, O. Akbulut and G. M. Whitesides, "Integration of paper-based microfluidic devices with commercial electrochemical readers," *Lab Chip*, vol. 10, no. 22, pp. 3163–3169, 2010.

[31] P. Rattanarat, W. Dungchai, D. Cate, J. Volckens, O. Chailapakul and C. S. Henry, "Multilayer paper-based device for colorimetric and electrochemical quantification of metals," *Anal. Chem.*, vol. 86, no. 7, pp. 3555–3562, 2014.

[32] J. L. Delaney, E. H. Doeven, A. J. Harsant and C. F. Hogan, "Use of a mobile phone for potentiostatic control with low cost paper-based microfluidic sensors," *Anal. Chim. Acta*, vol. 790, pp. 56–60, 2013.

[33] M. Su, L. Ge, Q. Kong, X. Zheng, S. Ge, N. Li, J. Yu and M. Yan, "Cyto-sensing in electrochemical lab-on-paper cyto-device for in-situ evaluation of multi-glycan expressions on cancer cells," *Biosens. Bioelectron.*, vol. 63, pp. 232–239, 2015.

[34] Y. Zhang, J. Bai, H. Wu and J. Y. Ying, "Trapping cells in paper for white blood cell count," *Biosens. Bioelectron.*, vol. 69, pp. 121–127, 2015.

[35] H. Shafiee, W. Asghar, F. Inci, M. Yuksekkaya, M. Jahangir, M. H. Zhang, N. G. Durmus, U. A. Gurkan, D. R. Kuritzkes and U. Demirci, "Paper and flexible substrates as materials for biosensing platforms to detect multiple biotargets," *Sci. Rep.*, vol. 5, 2015.

[36] Y. He, Y. Wu, J.-Z. Fu and W.-B. Wu, "Fabrication of paper-based microfluidic analysis devices: A review," *RSC Adv.*, vol. 5, no. 95, pp. 78 109–78 127, 2015.

[37] I. Ament, J. Prasad, A. Henkel, S. Schmachtel and C. Sonnichsen, "Single unlabeled protein detection on individual plasmonic nanoparticles," *Nano Lett.*, vol. 12, no. 2, pp. 1092–1095, 2012.

[38] L. Plucinski, M. R. Gartia, W. R. Arnold, A. Ameen, T.-W. Chang, A. Hsiao, G. L. Liu and A. Das, "Substrate binding to cytochrome P450-2J2 in Nanodiscs detected by nanoplasmonic Lycurgus cup arrays," *Biosens. Bioelectron.*, vol. 75, pp. 337–346, 2016.

[39] R. Rajasekharan, E. Balaur, A. Minovich, S. Collins, T. D. James, A. Djalalian-Assl, K. Ganesan, S. Tomljenovic-Hanic, S. Kandasamy and E. Skafidas, "Filling schemes at submicron scale: Development of submicron sized plasmonic colour filters," *Sci. Rep.*, vol. 4, 2014.

[40] S. Yokogawa, S. P. Burgos and H. A. Atwater, "Plasmonic color filters for CMOS image sensor applications," *Nano Lett.*, vol. 12, no. 8, pp. 4349–4354, 2012.

[41] Q. Gan, F. J. Bartoli and Z. H. Kafafi, "Plasmonic-enhanced organic photovoltaics: Breaking the 10% efficiency barrier," *Adv. Mater.*, vol. 25, no. 17, pp. 2385–2396, 2013.

[42] H. Shen and B. Maes, "Combined plasmonic gratings in organic solar cells," *Opt. Express*, vol. 19, no. 106, pp. A1202–A1210, 2011.

[43] S. L. Chuang, *Physics of Photonic Devices*. John Wiley & Sons, 2012.

[44] S. K. Dondapati, T. K. Sau, C. Hrelescu, T. A. Klar, F. D. Stefani and J. Feldmann, "Label-free biosensing based on single gold nanostars as plasmonic transducers," *ACS Nano*, vol. 4, no. 11, pp. 6318–6322, 2010.

[45] T. Endo, S. Yamamura, N. Nagatani, Y. Morita, Y. Takamura and E. Tamiya, "Localized surface plasmon resonance based optical biosensor using surface modified nanoparticle layer for label-free monitoring of antigenantibody reaction," *Sci. Technol. Adv. Mater.*, vol. 6, no. 5, pp. 491–500, 2005.

[46] K. M. Mayer, S. Lee, H. Liao, B. C. Rostro, A. Fuentes, P. T. Scully, C. L. Nehl and J. H. Hafner, "A label-free immunoassay based upon localized surface plasmon resonance of gold nanorods," *ACS Nano*, vol. 2, no. 4, pp. 687–692, 2008.

[47] F. Vollmer and S. Arnold, "Whispering-gallery-mode biosensing: Label-free detection down to single molecules," *Nat. Methods*, vol. 5, no. 7, pp. 591–596, 2008.

[48] L. S. Jung, C. T. Campbell, T. M. Chinowsky, M. N. Mar and S. S. Yee, "Quantitative interpretation of the response of surface plasmon resonance sensors to adsorbed films," *Langmuir*, vol. 14, no. 19, pp. 5636–5648, 1998.

[49] A. G. Brolo, "Plasmonics for future biosensors," *Nat. Photonics*, vol. 6, no. 11, pp. 709–713, 2012.

[50] I. D. Block, L. L. Chan and B. T. Cunningham, "Photonic crystal optical biosensor incorporating structured low-index porous dielectric," *Sens. Actuators, B*, vol. 120, no. 1, pp. 187–193, 2006.

[51] N. A. Rakow and K. S. Suslick, "A colorimetric sensor array for odour visualization," *Nature*, vol. 406, no. 6797, pp. 710–713, 2000.

[52] K. S. Suslick, N. A. Rakow and A. Sen, "Colorimetric sensor arrays for molecular recognition," *Tetrahedron*, vol. 60, no. 49, pp. 11 133–11 138, 2004.

[53] M. C. Janzen, J. B. Ponder, D. P. Bailey, C. K. Ingison and K. S. Suslick, "Colorimetric sensor arrays for volatile organic compounds," *Anal. Chem.*, vol. 78, no. 11, pp. 3591–3600, 2006.

[54] J. I. Hong and B.-Y. Chang, "Development of the smartphone-based colorimetry for multi-analyte sensing arrays," *Lab Chip*, vol. 14, no. 10, pp. 1725–1732, 2014.

[55] A. K. Yetisen, J. L. Martinez-Hurtado, A. Garcia-Melendrez, F. da Cruz Vasconcellos and C. R. Lowe, "A smartphone algorithm with inter-phone repeatability for the analysis of colorimetric tests," *Sens. Actuators, B*, vol. 196, pp. 156–160, 2014.

[56] T. W. Ebbesen, H. J. Lezec, H. F. Ghaemi, T. Thio and P. A. Wolff, "Extraordinary optical transmission through sub-wavelength hole arrays," *Nature*, vol. 391, no. 6668, pp. 667–669, 1998.

[57] T.-W. Chang, X. Wang, A. Hsiao, Z. Xu, G. Lin, M. R. Gartia, X. Liu and G. L. Liu, "Bifunctional nano Lycurgus cup array plasmonic sensor for colorimetric sensing and surfaceenhanced Raman spectroscopy," *Adv. Opt. Mater.*, vol. 3, no. 10, pp. 1397–1404, 2015.

[58] S. Seo, L. Edwards and G. Logan Liu, "Absorbance amplification using chromophore-nanoplasmon coupling for ultrasensitive protein quantification," *Anal. Chem.*, vol. 87, no. 19, pp. 9710–9714, 2015.

[59] A. G. Brolo, R. Gordon, B. Leathem and K. L. Kavanagh, "Surface plasmon sensor based on the enhanced light transmission through arrays of nanoholes in gold films," *Langmuir*, vol. 20, no. 12, pp. 4813–4815, 2004.

[60] S.-H. Chang, S. Gray and G. Schatz, "Surface plasmon generation and light transmission by isolated nanoholes and arrays of nanoholes in thin metal films," *Opt. Express*, vol. 13, no. 8, pp. 3150–3165, 2005.

[61] X. Zhang, Z. Li, S. Ye, S. Wu, J. Zhang, L. Cui, A. Li, T. Wang, S. Li and B. Yang, "Elevated Ag nanohole arrays for high performance plasmonic sensors based on extraordinary optical transmission," *J. Mater. Chem.*, vol. 22, no. 18, pp. 8903–8910, 2012.

[62] W. Yue, Y. Yang, Z. Wang, J. Han, A. Syed, L. Chen, K. Wong and X. Wang, "Improved surface-enhanced Raman scattering on arrays of gold quasi-3D nanoholes," *J. Phys. D. Appl. Phys.*, vol. 45, no. 42, p. 425401, 2012.

[63] D. A. Armbruster and T. Pry, "Limit of blank, limit of detection and limit of quantitation," *Clin. Biochem. Rev.*, vol. 29, no. Suppl 1, pp. S49–52, 2008.

[64] G. Group, "Randomised placebo-controlled trial of effect of ramipril on decline in glomerular filtration rate and risk of terminal renal failure in proteinuric, non-diabetic nephropathy," *Lancet*, vol. 349, no. 9069, pp. 1857–1863, 1997.

[65] K. Fajerwerg, V. Ynam, B. Chaudret, V. Garçon, D. Thouron and M. Comtat, "An original nitrate sensor based on silver nanoparticles electrodeposited on a gold electrode," *Electrochem. Commun.*, vol. 12, no. 10, pp. 1439–1441, 2010.

[66] M. J. Moorcroft, J. Davis and R. G. Compton, "Detection and determination of nitrate and nitrite: A review," *Talanta*, vol. 54, no. 5, pp. 785–803, 2001.

[67] A. Büldt and U. Karst, "Determination of nitrite in waters by microplate fluorescence spectroscopy and HPLC with fluorescence detection," *Anal. Chem.*, vol. 71, no. 15, pp. 3003–3007, 1999.

[68] D. L. Granger, R. R. Taintor, K. S. Boockvar and J. B. Hibbs, "Measurement of nitrate and nitrite in biological samples using nitrate reductase and Griess reaction," *Methods*, vol. 268, pp. 142–151, 1996.

[69] M. A. Titheradge, "The enzymatic measurement of nitrate and nitrite," *Nitric Oxide Protoc.*, pp. 83–91, 1998.

[70] H. Wang, W. Yang, S.-C. Liang, Z.-M. Zhang, and H.-S. Zhang, "Spectrofluorimetric determination of nitrite with 5, 6-diamino-1, 3-naphthalene disulfonic acid," *Anal. Chim. Acta*, vol. 419, no. 2, pp. 169–173, 2000.

[71] S. Kage, K. Kudo and N. Ikeda, "Determination of nitrate in blood by gas chromatography and gas chromatography–mass spectrometry," *J. Chromatogr. B Biomed. Sci. Appl.*, vol. 742, no. 2, pp. 363–368, 2000.

[72] M. I. Helaleh and T. Korenaga, "Ion chromatographic method for simultaneous determination of nitrate and nitrite in human saliva," *J. Chromatogr. B Biomed. Sci. Appl.*, vol. 744, no. 2, pp. 433–437, 2000.

[73] M. J. Dunphy, D. D. Goble and D. J. Smith, "Nitrate analysis by capillary gas chromatography," *Anal. Biochem.*, vol. 184, no. 2, pp. 381–387, 1990.

[74] H. Kodamatani, S. Yamazaki, K. Saito, T. Tomiyasu and Y. Komatsu, "Selective determination method for measurement of nitrite and nitrate in water samples using high-performance liquid chromatography with post-column photochemical reaction and chemiluminescence detection," *J. Chromatogr., A*, vol. 1216, no. 15, pp. 3163–3167, 2009.

[75] G. M. Janini, K. C. Chan, G. M. Muschik and H. J. Issaq, "Analysis of nitrate and nitrite in water and urine by capillary zone electrophoresis," *J. Chromatogr. B Biomed. Sci. Appl.*, vol. 657, no. 2, pp. 419–423, 1994.

[76] A. A. Okemgbo, H. H. Hill, W. F. Siems and S. G. Metcalf, "Reverse polarity capillary zone electrophoretic analysis of nitrate and nitrite in natural water samples," *Anal. Chem.*, vol. 71, no. 14, pp. 2725–2731, 1999.

[77] G. Hanrahan, D. G. Patil and J. Wang, "Electrochemical sensors for environmental monitoring: Design, development and applications," *J. Environ. Monit.*, vol. 6, no. 8, pp. 657–664, 2004.

[78] D. Kim, I. B. Goldberg and J. W. Judy, "Chronocoulometric determination of nitrate on silver electrode and sodium hydroxide electrolyte," *Analyst*, vol. 132, no. 4, pp. 350–357, 2007.

[79] M. A. Bhat, P. P. Ingole, V. R. Chaudhari and S. K. Haram, "Mechanistic aspects of nitrate ion reduction on silver electrode: Estimation of O–NO2- bond dissociation energy using cyclic voltammetry," *New J. Chem.*, vol. 33, no. 1, pp. 207–210, 2009.

[80] S. Li, J. Kiehne, L. I. Sinoway, C. E. Cameron and T. J. Huang, "Microfluidic opportunities in the field of nutrition," *Lab Chip*, vol. 13, no. 20, pp. 3993–4003, 2013.

[81] D. Kim, I. B. Goldberg and J. W. Judy, "Microfabricated electrochemical nitrate sensor using double-potential-step chronocoulometry," *Sens. Actuators, B*, vol. 135, no. 2, pp. 618–624, 2009.

[82] S. K. Vashist, O. Mudanyali, E. M. Schneider, R. Zengerle and A. Ozcan, "Cellphone-based devices for bioanalytical sciences," *Anal. Bioanal. Chem.*, vol. 406, no. 14, pp. 3263–3277, 2014.

[83] A. Ozcan, "Mobile phones democratize and cultivate next-generation imaging, diagnostics and measurement tools," *Lab Chip*, vol. 14, no. 17, pp. 3187–3194, 2014.

[84] Q. Wei, H. Qi, W. Luo, D. Tseng, S. J. Ki, Z. Wan, Z. Gorocs, L. A. Bentolila, T.-T. Wu, R. Sun et al., "Fluorescent imaging of single nanoparticles and viruses on a smart phone," *ACS Nano*, vol. 7, no. 10, pp. 9147–9155, 2013.

[85] J. Jiang, X. Wang, R. Chao, Y. Ren, C. Hu, Z. Xu and G. L. Liu, "Smartphone based portable bacteria pre-concentrating microfluidic sensor and impedance sensing system," *Sens. Actuators, B*, vol. 193, pp. 653–659, 2014.

[86] S. Cattarin, "Electrochemical reduction of nitrogen oxyanions in 1 M sodium hydroxide solutions at silver, copper and CuInSe2 electrodes," *J. Appl. Electrochem.*, vol. 22, no. 11, pp. 1077–1081, 1992.

[87] M. Fedurco, P. Kedzierzawski and J. Augustynski, "Effect of multivalent cations upon reduction of nitrate ions at the Ag electrode," *J. Electrochem. Soc.*, vol. 146, no. 7, pp. 2569–2572, 1999.

[88] G. Dima, A. De Vooys and M. Koper, "Electrocatalytic reduction of nitrate at low concentration on coinage and transition-metal electrodes in acid solutions," *J. Electroanal. Chem.*, vol. 554, pp. 15–23, 2003.

[89] M. R. Majidi, K. Asadpour-Zeynali and B. Hafezi, "Fabrication of nanostructured copper thin films at disposable pencil graphite electrode and its application to elecrocatalytic reduction of nitrate," *Int. J. Electrochem. Sci*, vol. 6, pp. 162–170, 2011.

[90] M. R. Gartia, B. Braunschweig, T.-W. Chang, P. Moinzadeh, B. S. Minsker, G. Agha, A. Wieckowski, L. L. Keefer and G. L. Liu, "The microelectronic wireless nitrate sensor network for environmental water monitoring," *J. Environ. Monit.*, vol. 14, no. 12, pp. 3068–3075, 2012.

[91] X. Wang, M. R. Gartia, J. Jiang, T.-W. Chang, J. Qian, Y. Liu, X. Liu and G. L. Liu, "Audio jack based miniaturized mobile phone electrochemical sensing platform," *Sens. Actuators, B*, vol. 209, pp. 677–685, 2015.

[92] E. Savinova, P. Kraft, B. Pettinger and K. Doblhofer, "In situ Raman spectroscopy studies of the interface between silver (111) electrodes and alkaline NaF electrolytes," *J. Electroanal. Chem.*, vol. 430, no. 1, pp. 47–56, 1997.

[93] R. Zadro, B. Pokrić and Z. Pucar, "Dependence of diffusion coefficients and immunoprecipitating titers on pH: Human serum transferrin, immunoglobulin a, human chorionic somatomammotropin, and their rabbit antibodies," *Anal. Biochem.*, vol. 117, no. 1, pp. 238–244, 1981.

[94] U. NRCS, "Soil survey division staff (1993) soil survey manual. Soil conservation service," *US Department of Agriculture Handbook*, vol. 18, p. 315.

[95] E. Savinova, S. Wasle and K. Doblhofer, "Structure and activity relations in the hydrogen peroxide reduction at silver electrodes in alkaline NaF/NaOH electrolytes," *Electrochim. Acta*, vol. 44, no. 8, pp. 1341–1348, 1998.

[96] V. Murray and G. Lau, "Drinking water safety: Guidance to health and water professionals and other health protection issues on water safety," in *Water Contamination Emergencies*, 2011, pp. 1–12.

[97] L. Wang, Q. Liu, Z. Hu, Y. Zhang, C. Wu, M. Yang and P. Wang, "A novel electrochemical biosensor based on dynamic polymerase-extending hybridization for E. coli O157: H7 DNA detection," *Talanta*, vol. 78, no. 3, pp. 647–652, 2009.

[98] Q. Liu, H. Cai, Y. Xu, L. Xiao, M. Yang and P. Wang, "Detection of heavy metal toxicity using cardiac cell-based biosensor," *Biosens. Bioelectron.*, vol. 22, no. 12, pp. 3224–3229, 2007.

[99] N. J. Ashbolt, "Microbial contamination of drinking water and disease outcomes in developing regions," *Toxicology*, vol. 198, no. 1, pp. 229–238, 2004.

[100] X. Xue, J. Pan, H. Xie, J. Wang and S. Zhang, "Fluorescence detection of total count of Escherichia coli and Staphylococcus aureus on water-soluble CdSe quantum dots coupled with bacteria," *Talanta*, vol. 77, no. 5, pp. 1808–1813, 2009.

[101] K. M. Horsman, J. M. Bienvenue, K. R. Blasier and J. P. Landers, "Forensic DNA analysis on microfluidic devices: A review," *J. Forensic Sci.*, vol. 52, no. 4, pp. 784–799, 2007.

[102] A. Battaglia, A. J. Schweighardt and M. M. Wallace, "Pathogen detection using a liquid array technology," *J. Forensic Sci.*, vol. 56, no. 3, pp. 760–765, 2011.

[103] J. Cai, C. Yao, J. Xia, J. Wang, M. Chen, J. Huang, K. Chang, C. Liu, H. Pan and W. Fu, "Rapid parallelized and quantitative analysis of five pathogenic bacteria by ITS hybridization using QCM biosensor," *Sens. Actuators, B*, vol. 155, no. 2, pp. 500–504, 2011.

[104] Z. Wang, T. Han, T.-J. Jeon, S. Park and S. M. Kim, "Rapid detection and quantification of bacteria using an integrated micro/nanofluidic device," *Sens. Actuators, B*, vol. 178, pp. 683–688, 2013.

[105] E. P. Randviir and C. E. Banks, "Electrochemical impedance spectroscopy: An overview of bioanalytical applications," *Anal. Methods*, vol. 5, no. 5, pp. 1098–1115, 2013.

[106] B.-Y. Chang and S.-M. Park, "Electrochemical impedance spectroscopy," *Annu. Rev. Anal. Chem.*, vol. 3, pp. 207–229, 2010.

[107] L. Yang and R. Bashir, "Electrical/electrochemical impedance for rapid detection of foodborne pathogenic bacteria," *Biotechnol. Adv.*, vol. 26, no. 2, pp. 135–150, 2008.

[108] D. Mark, F. von Stetten and R. Zengerle, "Microfluidic apps for off-the-shelf instruments," *Lab Chip*, vol. 12, no. 14, pp. 2464–2468, 2012.

[109] J. Paek, J. Kim and R. Govindan, "Energy-efficient rate-adaptive GPS-based positioning for smartphones," in *Proceedings of the 8th International Conference on Mobile Systems, Applications, and Services*. ACM, 2010, pp. 299–314.

[110] H. Falaki, R. Mahajan, S. Kandula, D. Lymberopoulos, R. Govindan and D. Estrin, "Diversity in smartphone usage," in *Proceedings of the 8th International Conference on Mobile Systems, Applications, and Services*. ACM, 2010, pp. 179–194.

[111] N. Ramanathan, M. Lukac, T. Ahmed, A. Kar, P. Praveen, T. Honles, I. Leong, I. Rehman, J. Schauer and V. Ramanathan, "A cellphone based system for large-scale monitoring of black carbon," *Atmos. Environ.*, vol. 45, no. 26, pp. 4481–4487, 2011.

[112] J. Li, "Nanosensors-cellphone integration for extended chemical sensing network," 2011.

[113] X.-Z. R. Yuan, C. Song, H. Wang and J. Zhang, *Electrochemical Impedance Spectroscopy in PEM Fuel Cells: Fundamentals and Applications*. Springer Science & Business Media, 2009.

[114] C. Ruan, L. Yang and Y. Li, "Immunobiosensor chips for detection of Escherichia coli O157: H7 using electrochemical impedance spectroscopy," *Anal. Chem.*, vol. 74, no. 18, pp. 4814–4820, 2002.

[115] E. Ferro and F. Potorti, "Bluetooth and wi-fi wireless protocols: A survey and a comparison," *IEEE Wireless Commun.*, vol. 12, no. 1, pp. 12–26, 2005.

[116] K. Stulík, C. Amatore, K. Holub, V. Marecek and W. Kutner, "Microelectrodes. definitions, characterization, and applications (technical report)," *Pure Appl. Chem.*, vol. 72, no. 8, pp. 1483–92, 2000.

[117] D. A. Lytle, E. W. Rice, C. H. Johnson and K. R. Fox, "Electrophoretic mobilities of Escherichia coli O157: H7 and wild-type Escherichia coli strains," *Appl. Environ. Microbiol.*, vol. 65, no. 7, pp. 3222–3225, 1999.

[118] B. F. Rodak, G. A. Fritsma and E. Keohane, *Hematology: Clinical Principles and Applications*. Elsevier Health Sciences, 2013.

[119] D. M. Jaffe and G. R. Fleisher, "Temperature and total white blood cell count as indicators of bacteremia," *Pediatrics*, vol. 87, no. 5, pp. 670–674, 1991.

[120] R. Virkki, T. Juven, H. Rikalainen, E. Svedström, J. Mertsola and O. Ruuskanen, "Differentiation of bacterial and viral pneumonia in children," *Thorax*, vol. 57, no. 5, pp. 438–441, 2002.

[121] G. Opdenakker, W. E. Fibbe and J. Van Damme, "The molecular basis of leukocytosis," *Immunol. Today*, vol. 19, no. 4, pp. 182–189, 1998.

[122] E. V. Granowitz and R. B. Brown, "Antibiotic adverse reactions and drug interactions," *Crit. Care Clin.*, vol. 24, no. 2, pp. 421–442, 2008.

[123] F. Koinis, G. Nintos, V. Georgoulias and A. Kotsakis, "Therapeutic strategies for chemotherapy-induced neutropenia in patients with solid tumors," *Expert Opin. Pharmacother.*, vol. 16, no. 10, pp. 1505–1519, 2015.

[124] T. J. Smith, K. Bohlke, G. H. Lyman, K. R. Carson, J. Crawford, S. J. Cross, J. M. Goldberg, J. L. Khatcheressian, N. B. Leighl, C. L. Perkins et al., "Recommendations for the use of WBC growth factors: American society of clinical oncology clinical practice guideline update," *J. Clin. Oncol.*, vol. 33, no. 28, pp. 3199–3212, 2015.

[125] B. H. Hyun, G. L. Gulati and J. K. Ashton, "Differential leukocyte count: Manual or automated, what should it be?" *Yonsei Med J*, vol. 32, no. 4, pp. 283–291, 1991.

[126] M. Buttarello and M. Plebani, "Automated blood cell counts: State of the art," *Am. J. Clin. Pathol.*, vol. 130, no. 1, pp. 104–116, 2008.

[127] L. Terstappen, B. G. DeGrooth, K. Visscher, F. A. VanKouterik and J. Greve, "Four-Parameter white blood cell differential counting based on light scattering measurements," *Cytometry*, vol. 9, no. 1, pp. 39–43, 1988.

[128] J. C. Hudson, R. F. Brunhouse, C. Garrison, C. M. Rodriguez, R. Zwerner and T. R. Russell, "Lymphocyte subset determination using a hematology analyzer," *Cytometry*, vol. 22, no. 2, pp. 150–153, 1995.

[129] M. D. Graham, "The Coulter principle: Foundation of an industry," *J. Assoc. Lab. Autom.*, vol. 8, no. 6, pp. 72–81, 2003.

[130] X. Cheng, D. Irimia, M. Dixon, K. Sekine, U. Demirci, L. Zamir, R. G. Tompkins, W. Rodriguez and M. Toner, "A microfluidic device for practical label-free CD4 T cell counting of HIV-infected subjects," *Lab Chip*, vol. 7, no. 2, pp. 170–178, 2007.

[131] M. T. Glynn, D. J. Kinahan and J. Ducrée, "Rapid, low-cost and instrument-free CD4 cell counting for HIV diagnostics in resource-poor settings," *Lab Chip*, vol. 14, no. 15, pp. 2844–2851, 2014.

[132] X. Chen, C. C. Liu and H. Li, "Microfluidic chip for blood cell separation and collection based on crossflow filtration," *Sens. Actuators, B*, vol. 130, no. 1, pp. 216–221, 2008.

[133] D. M. Cate, J. A. Adkins, J. Mettakoonpitak and C. S. Henry, "Recent developments in paper-based microfluidic devices," *Anal. Chem.*, vol. 87, no. 1, pp. 19–41, 2014.

[134] J. Adkins, K. Boehle and C. Henry, "Electrochemical paper-based microfluidic devices," *Electrophoresis*, vol. 36, no. 16, pp. 1811–1824, 2015.

[135] M. Cuartero, G. A. Crespo and E. Bakker, "Paper-based thin-layer coulometric sensor for halide determination," *Anal. Chem.*, vol. 87, no. 3, pp. 1981–1990, 2015.

[136] X. Li, K. Scida and R. M. Crooks, "Detection of Hepatitis B virus DNA with a paper electrochemical sensor," *Anal. Chem.*, vol. 87, no. 17, pp. 9009–9015, 2015.

[137] F. Liu and C. Zhang, "A novel paper-based microfluidic enhanced chemiluminescence biosensor for facile, reliable and highly-sensitive gene detection of listeria monocytogenes," *Sens. Actuators, B*, vol. 209, pp. 399–406, 2015.

[138] C. Ma, W. Li, Q. Kong, H. Yang, Z. Bian, X. Song, J. Yu and M. Yan, "3D origami electrochemical immunodevice for sensitive point-of-care testing based on dual-signal amplification strategy," *Biosens. Bioelectron.*, vol. 63, pp. 7–13, 2015.

[139] D. Zhang and Q. Liu, "Biosensors and bioelectronics on smartphone for portable biochemical detection," *Biosens. Bioelectron.*, vol. 75, pp. 273–284, 2016.

[140] G. L. Damhorst, C. Duarte-Guevara, W. Chen, T. Ghonge, B. T. Cunningham and R. Bashir, "Smartphone-imaged HIV-1 reverse-transcription loop-mediated isothermal amplification (RT-LAMP) on a chip from whole blood," *Engineering*, vol. 1, no. 3, pp. 324–335, 2015.

[141] S. Choi, "Powering point-of-care diagnostic devices," *Biotechnol. Adv.*, vol. 34, no. 3, pp. 321–330, 2016.

[142] H. J. Chun, Y. M. Park, Y. D. Han, Y. H. Jang and H. C. Yoon, "Paper-based glucose biosensing system utilizing a smartphone as a signal reader," *BioChip J.*, vol. 8, no. 3, pp. 218–226, 2014.

[143] J. L. Delaney, C. F. Hogan, J. Tian and W. Shen, "Electrogenerated chemiluminescence detection in paper-based microfluidic sensors," *Anal. Chem.*, vol. 83, no. 4, pp. 1300–1306, 2011.

[144] V. Oncescu, D. O'Dell and D. Erickson, "Smartphone based health accessory for colorimetric detection of biomarkers in sweat and saliva," *Lab Chip*, vol. 13, no. 16, pp. 3232–3238, 2013.

[145] W. Chen, K. D. Long, J. Kurniawan, M. Hung, H. Yu, B. A. Harley and B. T. Cunningham, "Planar photonic crystal biosensor for quantitative label-free cell attachment microscopy," *Adv. Opt. Mater.*, vol. 3, no. 11, pp. 1623–1632, 2015.

[146] A. G. A. Aggidis, J. D. Newman and G. A. Aggidis, "Investigating pipeline and state of the art blood glucose biosensors to formulate next steps," *Biosens. Bioelectron.*, vol. 74, pp. 243–262, 2015.

[147] M. Varshney and Y. Li, "Interdigitated array microelectrodes based impedance biosensors for detection of bacterial cells," *Biosens. Bioelectron.*, vol. 24, no. 10, pp. 2951–2960, 2009.

[148] L. Yang, Y. Li and G. F. Erf, "Interdigitated array microelectrode-based electrochemical impedance immunosensor for detection of Escherichia coli O157: H7," *Anal. Chem.*, vol. 76, no. 4, pp. 1107–1113, 2004.

[149] S. J. Konopka and B. McDuffie, "Diffusion coefficients of ferri-and ferrocyanide ions in aqueous media, using twin-electrode thin-layer electrochemistry," *Anal. Chem.*, vol. 42, no. 14, pp. 1741–1746, 1970.

[150] F. Wei, P. Patel, W. Liao, K. Chaudhry, L. Zhang, M. Arellano-Garcia, S. Hu, D. Elashoff, H. Zhou, S. Shukla et al., "Electrochemical sensor for multiplex biomarkers detection," *Clin. Cancer Res.*, vol. 15, no. 13, pp. 4446–4452, 2009.

[151] X. Cao, J. Ma, X. Shi and Z. Ren, "Effect of TiO2 nanoparticle size on the performance of PVDF membrane," *Appl. Surf. Sci.*, vol. 253, no. 4, pp. 2003–2010, 2006.

[152] S. Yu and C. Gao, "Research on PVDF UF membrane with small pore size," *Technol. Water Treat.*, vol. 25, pp. 83–88, 1999.

[153] L.-Y. Yu, Z.-L. Xu, H.-M. Shen and H. Yang, "Preparation and characterization of PVDF-SiO2 composite hollow fiber UF membrane by sol-gel method," *J. Memb. Sci.*, vol. 337, no. 1, pp. 257–265, 2009.

[154] J. Bisquert, G. Garcia-Belmonte, F. Fabregat-Santiago and A. Compte, "Anomalous transport effects in the impedance of porous film electrodes," *Electrochem. commun.*, vol. 1, no. 9, pp. 429–435, 1999.

[155] J. Bisquert, G. Garcia-Belmonte, P. Bueno, E. Longo and L. O. S. Bulhoes, "Impedance of constant phase element (CPE)-blocked diffusion in film electrodes," *J. Electroanal. Chem.*, vol. 452, no. 2, pp. 229–234, 1998.

[156] J. Bisquert, G. Garcia-Belmonte, F. Fabregat-Santiago and P. R. Bueno, "Theoretical models for ac impedance of finite diffusion layers exhibiting low frequency dispersion," *J. Electroanal. Chem.*, vol. 475, no. 2, pp. 152–163, 1999.

[157] R. G. Compton and C. E. Banks, *Understanding Voltammetry*. World Scientific, 2007.

[158] X. Li, J. Tian, T. Nguyen and W. Shen, "Paper-based microfluidic devices by plasma treatment," *Anal. Chem.*, vol. 80, no. 23, pp. 9131–9134, 2008.

[159] S. I. Fox, "Human Physiology 9th Editon," 1996.

[160] C. Porth, *Essentials of Pathophysiology: Concepts of Altered Health States*. Lippincott Williams & Wilkins, 2011.